Conceptual Design Report: Main Injector Neutrino Program

Physics Goals, Technical Components, and Civil Construction
June 14, 1991

Version 1.1

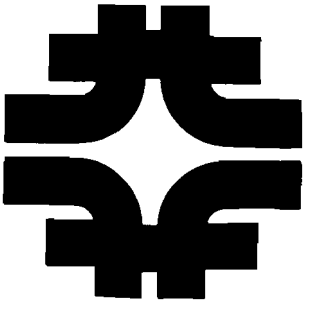

Fermi National Accelerator Laboratory
Batavia, Illinois

Operated by Universities Research Association Inc.
Under Contract with the United States Department of Energy

Authors

R. Bernstein, L. Beverly, F. Browning, S. Childress, W. Freeman, V. Jacobsen, G. Koizumi, J. Krider, L. Kula, A. Malensek, S. Pordes, R. Trendler, E. Villegas, R. Williams
Fermi National Accelerator Laboratory

N. W. Reay,[7] R. Sidwell,[7] N. Stanton[7]
P–803

S. Dye,[2] W. Gajewski,[8] J. Schultz,[8] R. Svoboda[5]
P–805

R. Johnson,[9] S. Mishra,[3] M. Shaevitz,[3] I. Stockdale,[9] F. Taylor[6]
P–815

M. Goodman[1]
P-822

J. Learned,[4] V. Peterson,[4] A. Roberts,[4] V. Stenger,[4] M. Webster[10]
P-824

[1] Argonne National Laboratory
[2] Boston University
[3] Columbia University
[4] Hawaii DUMAND Center/University of Hawaii
[5] Louisiana State University
[6] Massachusetts Institute of Technology
[7] Ohio State University
[8] University of California at Irvine
[9] University of Cincinnati
[10] Vanderbilt University

Contents

List of Figures

List of Tables

Preface

The Main Injector will have a profound impact on neutrino physics. It will enable us to improve existing measurements and make basic discoveries of new physics in both $\nu_\mu N$ deep-inelastic scattering experiments and searches for neutrino oscillations. At Tevatron energies the errors on electroweak parameters will be substantially reduced and precise tests of QCD achieved. At intermediate energies it will create an entirely new program focusing on neutrino oscillations. Experiments which will search for the "missing mass" of the Universe have already been proposed. The program will provide the first well-controlled test of the solar and atmospheric neutrino puzzles which provide a mounting but inconclusive body of evidence for neutrino mass and mixing.

These two classes of experiments test the Standard Model across a wide energy range and confront fundamental predictions of both the Standard Model and the suggested alternatives. The deep-inelastic experiments test the radiative corrections in electroweak physics providing information on supersymmetry, technicolor, and the nature of the Higgs sector. It will test some of basic predictions of QCD for the first time, measuring the fine-structure constant of the strong interactions as well as the gluon distributions. Searches for neutrino oscillations directly confront the issues of neutrino mass and lepton number violation and have become increasingly important as circumstantial evidence on neutrino oscillation builds. The programs are complementary as well; the high-energy experiments will search for oscillations in regions inaccessible to the intermediate energy experiments, and the oscillation experiments can provide useful measurements of charm production and V_{cd} to the Tevatron program. The remarkable range and depth of such a neutrino program is unlikely to be duplicated in the future.

Over the past several years, Fermilab has held several Workshops in which a renaissance of neutrino physics either has been the main thrust [1] or a significant part of the program. [2,3] Both Tevatron energy and intense lower energy neutrino beams are required, but whether measurements are of $\sin^2\theta_W$ or of neutrinos oscillating over baselines of hundreds of kilometers, intensity is the motivating factor. Increased fluxes made possible by the Main Injector upgrade will open exciting new vistas for neutrino research.

In order to evaluate this program as a whole, Fermilab called for the construction of an overall Conceptual Design Report. Neutrino physics was to be sharply defined, requirements

and costs determined in a manner more concise than for previous fixed target experiments, conflicts between efforts minimized, and whenever possible commonalities of interest exploited to lower projected expenditures.

Fermilab Director John Peoples appointed N. W. Reay as the head of this effort in April, 1990, and subsequently he was joined by more than a dozen people both from Fermilab and from other Laboratories and Universities associated with each type of new physics. The group began by preparing for and attending Snowmass 1990, and since August has held weekly meetings at Fermilab in the course of defining issues, solving problems and constructing this report. During this period three letters of intent for new neutrino physics have evolved into full proposals, and two new letters have been submitted.

Feedback from the Fermilab Physics Advisory Committee has been solicited throughout; progress reports have been submitted to the PAC Spring, Summer, and Fall 1990 meetings.

References

[1] New Directions in Neutrino Physics at Fermilab, Fermi National Accelerator Laboratory pub. (1989).

[2] Proceedings of the Summer Study of High Energy Physics in the 1990's, Singapore, World Scientific Pub. (1989).

[3] Physics at Fermilab in the 1990's (Breckenridge), Singapore.

Part I

Physics Goals and Experimental Methods

1 Introduction and Physics Goals

The Main Injector will provide an unprecedented opportunity for challenging the Standard Model. The increased fluxes available from this essential upgrade make possible neutrino experiments of great power both at the Tevatron and at intermediate energies.

With a factor of six increase in flux, experiments at higher energies probe with great sensitivity the electroweak sector, test QCD, and search for rare processes which could point the way to new physics. Such experiments can make simultaneous measurements of the Standard Model ρ parameter and $\sin^2\theta_W$ to 0.25% and 0.6%, respectively.

Measurements of the radiative corrections in electroweak physics will reveal physics at the TeV mass scale. ρ probes the Higgs sector, and deviations from its expected value would be unambiguous signals of new phenomena and possibly our first clear window into physics beyond the Standard Model. Another way to quantify these corrections is through measurements of $\sin^2\theta_W$ in different processes; comparisons among an ensemble of precise electroweak measurements can then distinguish among alternatives and pin down the sources of new phenomena. Four processes likely to be important in the coming decade are the direct boson mass measurements, Z polarization asymmetries, atomic parity violation, and neutrino-nucleon scattering. Each of these processes has a different dependence on the various sources of new physics: such phenomena as multiple Z's, supersymmetry, or technicolor are just three of many possibilities. Neutral current measurements of $\sin^2\theta_W$ and ρ have already provided constraints on m_t; improved measurements will extend their reach and help us interpret the information from the colliders.

QCD tests, especially those involving the structure function xF_3, can check two fundamental predictions of the theory: the dependence of the strong-coupling constant $\alpha_S(Q^2)$ on Q^2, and the value (and Q^2 dependence) of $R_{QCD} = \sigma_L/\sigma_T$. A Main Injector experiment will check the scaling violation of the theory and provide solid measurements of the gluon distributions.

The order-of-magnitude greater statistics will enable us to improve measurements of rare processes and search for new ones. Searches for $\nu_\mu \rightarrow \nu_e$ neutrino oscillations with

sensitivities reaching 10^{-4} for large Δm^2 along with improvements of the dimuon and trimuon rates are just a few of the possibilities.

The Main Injector upgrade also will create an entirely new program based on the extraction of 120 GeV protons. It will produce 3×10^{13} protons every 1.9 seconds, resulting in the most intense neutrino beam ever produced. Neutrino oscillations can be searched for in previously unexplored regions of parameter space. A positive signal for such oscillations would establish the non-conservation of lepton number and could answer two questions of cosmological or astrophysical significance.

Is the Universe closed? It is well-known that visible matter comprises only 10% of the matter necessary to close the Universe. A natural candidate for the "missing mass" is the ν_τ. One experiment would search for the oscillation $\nu_\mu \leftrightarrow \nu_\tau$ with a coupling sensitivity of 10^{-4} for $\Delta m^2 > 1\text{eV}^2$.

What are the solutions to the Solar and Atmospheric Neutrino Problems? Neutrinos from the Sun have too few ν_e and those created in the atmosphere show a dearth of ν_μ. With experiments designed to detect neutrino interactions at long-baselines of 500 km or more, oscillations due to Δm^2 as small as 0.003 eV^2 could be detected, sufficient to study the atmospheric problem under controlled conditions. A particularly elegant feature of this program is that the short-baseline $\nu_\mu \leftrightarrow \nu_\tau$ experiment could serve as a flux monitor for the long-baseline detector, providing systematic checks and an *in situ* flux measurement.

The above experiments will study $\nu_\mu \rightarrow \nu_\tau$, $\nu_\mu \rightarrow \nu_e$, $\nu_e \rightarrow \nu_\tau$, and ν_μ disappearance oscillations over an unprecedented range of Δm^2 and sensitivities. Byproducts of these efforts include a measurement to 3% of the Kobayashi-Maskawa matrix element V_{cd}. A deviation of this measurement from the 1% value determined by unitarity of the KM matrix would indicate new physics.

The Laboratory will have to make a substantial committment in order to fulfill the potential of this program, and this Conceptual Design Report was written in order to set forth both the promise of the program and the required effort. Specifically, this Report has three goals:

1. To explain the physics goals and potential of the program and to show how specific experiments have already been designed, taking advantage of the Main Injector, which will meet these goals.

2. To describe all technical components required and demonstrate their feasibility. We stress that the "conceptual designs" presented here require further work and eventually full engineering reviews.

3. To estimate the civil construction and costs required. Again, these designs are not final and await further evaluation and review.

We also present a funding profile based on our current plans. We conclude by indicating some areas which require more work and likely directions for future R&D.

We begin with a description of the physics.

2 P815: Tevatron Program

P–815 represents a new generation of deep-inelastic scattering experiments at the Tevatron. Building on a decade of experience and using the factor of six increase in fixed-target intensity available at the Main Injector, it will make dramatic improvements in three realms: electroweak physics, QCD tests, and searches for rare processes.

2.1 Electroweak Parameters

Deep-Inelastic Scattering has been an important tool in the search for new physics. During the past decade, neutrino-nucleon scattering has provided the best upper limit for m_t. With the precise and rapidly improving measurements of the W and Z masses, there now exist precise and unambiguous predictions for $\sin^2\theta_W$ given m_t within the Standard Model which can be decisively checked with improved measurements. P–815 Phase I,[1] to be run in 1993, will improve on previous determinations of $\sin^2\theta_W$ and ρ by a factor of three. Detector upgrades and the further increase in flux from the Main Injector will decrease the errors to ± 0.0015 on $\sin^2\theta_W$ and ± 0.0025 on ρ. At that time the prediction of m_t from $\sin^2\theta_W$ will have errors of ± 10 GeV (for fixed m_H).

The prediction of m_t is an example of the power of precise electroweak measurements. The errors on $\sin^2\theta_W$ from deep-inelastic scattering will be equal to those expected from A_{LR} and the W, Z mass measurements (although the measurement of ρ is unique!) but deep-inelastic scattering has a quite different dependence on new physics, providing powerful tests of the Standard Model and clues to whatever lies beyond it.[2]

Neutrino-nucleon scattering yields data which allow several methods of determining $\sin^2\theta_W$ and ρ. All are founded on the electroweak couplings of the Z^0 boson with quarks (δ) which depend on their weak isospin, (T_3^i) and electric charge (Q^i) of the quarks, and on $\sin^2\bar{\theta}_W$ by the relation:

$$\delta^i = T_3^i - Q^i \sin^2\bar{\theta}_W \tag{2.1}$$

The ρ parameter, defined by the relation,

$$\rho = M_W^2/M_Z^2 \cos^2 \bar{\theta}_W \tag{2.2}$$

measures the strength of the neutral current interaction. In the Standard Model with only one Higgs doublet, $\rho = 1$. Beyond the tree level, ρ can be different from one depending on various electroweak corrections such as those dependent on the top quark mass, m_t among other parameters. The parameter $\sin^2 \theta_W$ measured in deep-inelastic scattering is numerically close to the Sirlin ("mass-shell")value:[3]

$$\sin^2 \theta_W = 1 - \frac{M_W^2}{M_Z^2} \tag{2.3}$$

The value of $\sin^2 \theta_W$ measured in any process is a function of several variables: while the underlying gauge couplings provide a basic definition, the measured value for a particular experiment depends of such variables as m_t and the mass of the Higgs boson. This dependence is not trivial: it is the reason that $\sin^2 \theta_W$ must be measured in several different processes, all to high precision. An ensemble of experiments can then be used to extract specific sources of physics beyond the Standard Model. The strongest dependence in most processes is on the mass of the as-yet undiscovered top quark. The best upper limit on its mass has already been set by comparing the masses of the W and Z bosons to $\sin^2 \theta_W$ measured in neutrino-nucleon scattering. If we assume the top will have been discovered and its mass measured at CDF or D0 by the late 1990's, the observables R_ν and A_{LR} will test the overall consistency of the Standard Model and probe for new physics.[4]. Neutral current scattering is a particularly good complement to the collider determinations. Fig. 2.1 shows the region in ρ–$\sin^2 \theta_W$ space which will be allowed by the W and Z mass measurements and νN scattering. An interesting point is the great sensitivity of ρ to m_t; a shift in the mass from 150 to 200 GeV would shift the central point of the contour off the plot!

2.1.1 Methods of Extraction

Llewellyn Smith[5] has shown that for an isoscalar target with only massless u and d quarks, isospin invariance can be used to determine the largest contributions to the neutral current (NC) and charged current (CC) cross sections. Thus, the ratio $R_\nu = NC/CC$ can be written as:

$$R_{\nu[\bar{\nu}]} = \rho^2(1/2 - \sin^2 \theta_W + 5/9 \sin^4 \theta_W(1 + r^{[-1]})), \tag{2.4}$$

where $r = \sigma_{\bar{\nu}}^{CC}/\sigma_\nu^{CC}$ is the ratio of the antineutrino to neutrino charged-current cross section with the same experimental cuts as are used in the $\sin^2 \theta_W$ analysis. The factor r, derived from measurement, absorbs many of the quark-parton corrections which are otherwise difficult to take into account. In this method, (referred to here as the LS method), the

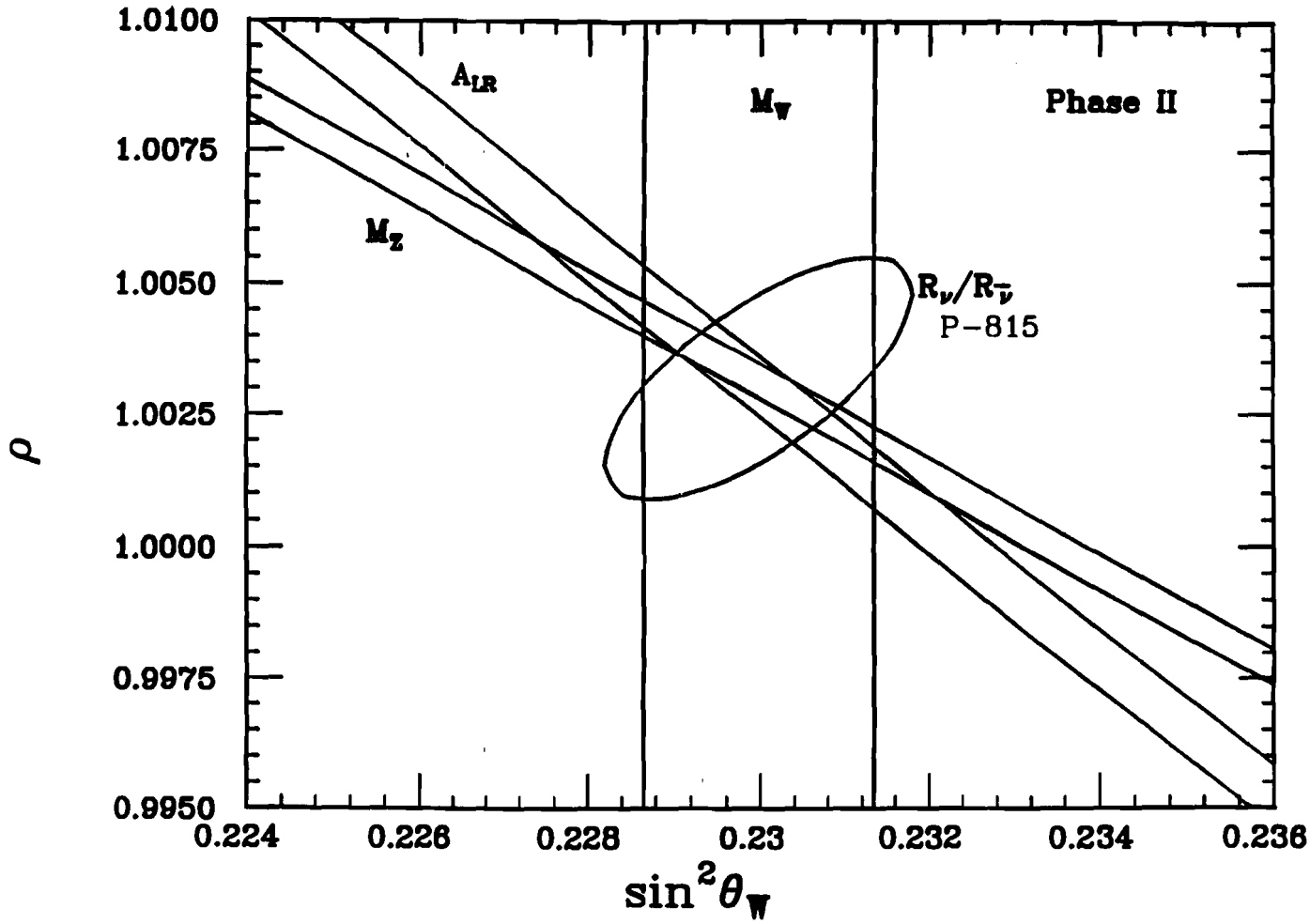

Figure 2.1: A comparison of the allowed regions in ρ–$\sin^2\theta_W$ space from M_W, M_Z and νN scattering, with $\delta M_W = 70$ MeV. The central values apply to the current world-average $\sin^2\theta_W$ and $m_t = 150$ GeV.

corrections associated with the target being nonisoscalar, the strange quark contribution, the charm quark kinematic factors, etc. are all treated as small corrections.

Another method for determining $\sin^2\theta_W$ which is theoretically robust is derived from the Paschos -Wolfenstein[6] (P-W) relations:

$$R^- = \frac{(\sigma_\nu^{NC} - \sigma_{\overline{\nu}}^{NC})}{(\sigma_\nu^{CC} - \sigma_{\overline{\nu}}^{CC})} = \rho^2(\frac{1}{2} - \sin^2\theta_W) \tag{2.5}$$

$$R^+ = \frac{(\sigma_\nu^{NC} + \sigma_{\overline{\nu}}^{NC})}{(\sigma_\nu^{CC} + \sigma_{\overline{\nu}}^{CC})} = \rho^2(\frac{1}{2} - \sin^2\theta_W + \frac{10}{9}\sin^4\theta_W) \tag{2.6}$$

Most corrections tend to cancel in the R^- ratio which makes the extracted $\sin^2\theta_W$ insensitive to many of the theoretical uncertainties although the relative normalization of neutrino to antineutrino data is required in order to obtain $\sin^2\theta_W$. Previous experiments have not used the P-W method due to these normalization uncertainties combined with inadequate antineutrino statistics. For the P815 experiment, the high statistics provided by the Main Injector combined with accurate techniques for determining the relative flux developed in previous experiments indicate that for a one-parameter fit, the P-W method will give the smallest error on $\sin^2\theta_W$.

The use of the two methods is primarily of use in checking systematics; a more detailed analysis of either method shows that for a two parameter fit, the contours of the Llewellyn Smith or Paschos-Wolfenstein methods are identical after the correlations among systematic errors are properly handled.

2.1.2 P-815 Beams for Electroweak Measurements

The Quadrupole Triplet beam used in the past cannot be used for a new generation of precise electroweak measurements. It focuses secondaries of both positive and negative charge; hence the beam is a mixture of neutrinos and antineutrinos in a ratio of about two to one. Separate measurements of $\mathrm{R}_\nu = \sigma_{NC}^\nu/\sigma_{CC}^\nu$ and $R_{\bar{\nu}} = \sigma_{NC}^{\bar{\nu}}/\sigma_{CC}^{\bar{\nu}}$ are therefore not possible and hence we cannot separately extract ρ.

A significant source of background in neutral current measurements is the presence of ν_e. In massive detectors with high-Z targets, such as Lab E, the e from charged current interactions is lost in the hadronic shower and all ν_e interactions appear as neutral currents. The primary souce of ν_e are semileptonic K-decays; the charged-K contribution can be measured from the data, but the Quadrupole Triplet allows neutral K_L to pass through unaffected. This component is especially troublesome since the production of K_L's is not precisely known and could contribute an error to the measured $\sin^2\theta_W$ of up to $\pm.005$.

A Sign-Selected Quadrupole Triplet beam (SSQT) would make possible the separate measurements of R_ν and $R_{\bar{\nu}}$ with little contamination from the opposite species, and would remove the ν_e background from K_L decays. We expect that such a beam will have been constructed and commissioned in P-815 Phase I, to be run in 1993.

For estimates of statistical power (and for estimates of groundwater activation in Sec. 7.3.1) we will asssume 4×10^{18} protons on target per calendar year. This is derived from the expected 6.0×10^{13} protons per minute given in the Main Injector CDR Rev. 2.3 and assumes a "Snowmass year" for a yearly run of 10^7 sec.

2.1.3 Sources of Error in Electroweak Measurements

The ν_e background from neutral K_L will be eliminated through the Sign-Selected Quadrupole Triplet. Remaining ν_e from charged K^+ can be estimated from the charged-current ν_μ observed from $K^+ \rightarrow \mu\nu_\mu$ decays. Considerable progress has been made in accurate modeling of this rate in the course of the E-744/E-770 analysis of the Quadrupole Triplet beam. We have modeled the beam and fit particle production invariant cross-sections directly to the data, finding only small variations from the Atherton data at 400 GeV/c.[7] Fig. 2.2 shows a representative fit; varying the K^+ fraction well outside the allowed errors from this fit only produces a change of < 0.001 in $\sin^2\theta_W$ and we expect that this error will be further reduced with the greater care we will apply to the Sign-Selected beam. We are also exploring other avenues of measuring this background: (a) if we can measure the K_L background in a separate run, then we may use the higher statistics Quadrupole Triplet beam, and (b) if we can measure the ν_e rate directly from the data (by looking for the shorter electromagnetic showers of charged-current electrons from $\nu_e N \rightarrow eN$) we can *remove* the contamination directly.

A significant error in any of these ratios is cross-talk between the charged current denominator and the neutral current numerator.[1] Events are classified as charged or neutrtal current according to their length along the beam direction as measured by the number of consecutive scintillation counters fired; a hadronic shower from neutral currents lasts only 1–2 m in the Lab E detector; a muon from a charged current event continues firing many counters downstream. The length distribution from E-744/770 along with a Monte Carlo are shown in Fig. 2.3.

If the muon in a charged current event ranges out from dE/dx loss before it exits the shower, or is produced at such a wide angle that it leaves the detector before it can be recognized, the apparent length will be small and the charged current event will be classified as a neutral current, biasing the ratio and hence the extracted values of $\sin^2\theta_W$ and ρ. The subtraction is approximately 12% for the CCFR spectrometer and Quadrupole Triplet energy spectrum. Approximately half the contamination comes from "range-outs" and half from "wide-angle" muons. The range-outs are events at large-y ($y = E_H/E_\nu$) and can be

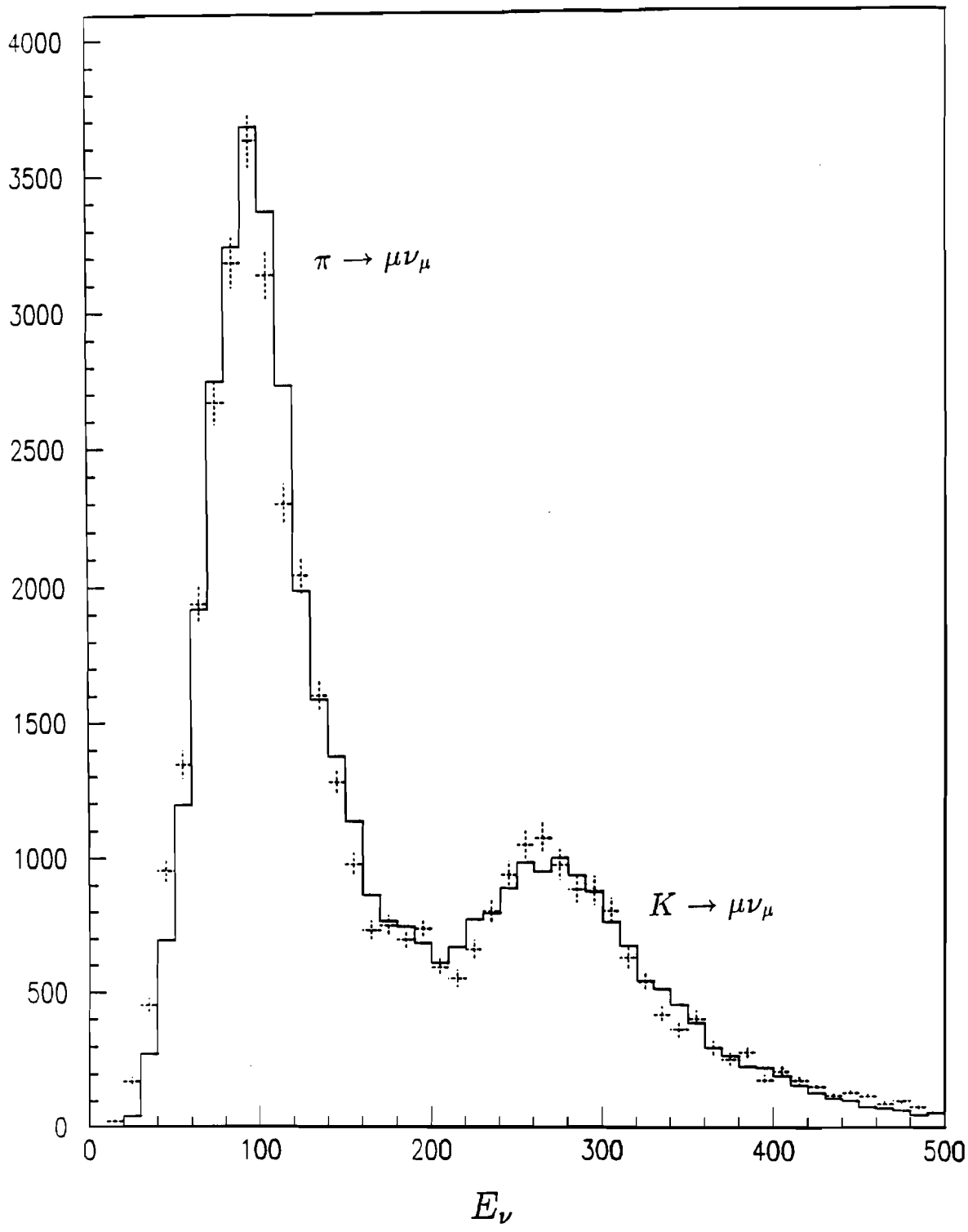

Figure 2.2: Fit to charged-current ν_μ spectrum in E-744/E-770 (only a fraction of the total data sample is displayed). The histogram is the data and the points are the fit. The lower-energy peak is from $\pi \rightarrow \mu\nu_\mu$ decays and the higher-energy peak comes from $K^+ \rightarrow \mu\nu_\mu$.

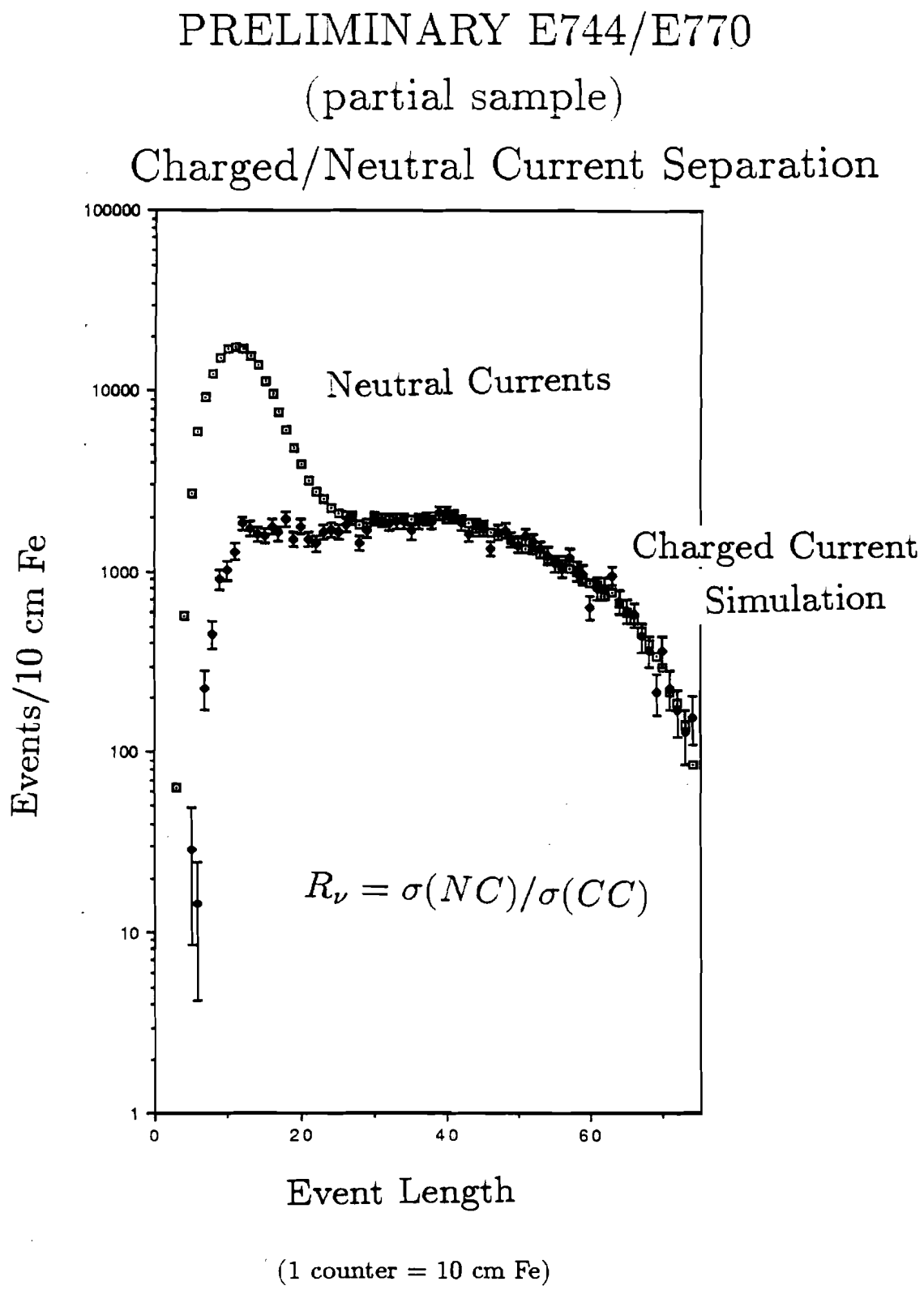

Figure 2.3: Length Distribution of Charged and Neutral Current events. The peak near small length is the neutral current sample. The tail is the charged current distribution. The dip at large length is from a geometric cut on the sample and is not from physics. A Monte Carlo, independently normalized, is overlaid.

estimated by a smooth extrapolation from intermediate y where the muon is visible. The wide-angle muons are a much more serious problem since they arise from muon-production at large $x = Q^2/2ME_H$. We attack this class of events in two ways: the first is through software and the second through hardware. We will upgrade the detector to contain twice as many drift chambers, to one chamber every 4 in. of Fe. GEANT simulations of the calorimeter indicate that with this sampling we will be able to track more than 90% of wide-angle muons. In hardware, we propose to *tag* exiting muons using an upgrade of our scintillation counters, directly eliminating the contamination. Our current estimates are that after the wide-angle muons are removed, the errors from charged-current background will be well under 1/2% on $\sin^2\theta_W$ and 1/4% on ρ.

The most significant theoretical error in the determination of $\sin^2\theta_W$ and ρ has been from estimating charm production from the d and s quarks in the nucleon. Charm-production constitutes 7% of the charged-current cross-section but is forbidden in neutral current processes since there are no flavor-changing neutral currents. This difference presents a bias in the extraction of the electroweak parameters: all the methods involve a ratio of neutral to charged-current processes, and charm-production therefore affects the denominator but not the numerator. An accurate modeling of the process is therefore essential for a precise determination of either ρ^2 and $\sin^2\theta_W$.

Since the charmed quark is heavy, there must be a kinematic penalty for its production. Slow-rescaling[1] models this penalty by the replacement:

$$x \rightarrow x(1 - \frac{m_c^2}{Q^2}), \tag{2.7}$$

a natural prescription. m_c is then a parameter which can be fit to the data from opposite-sign dimuon production, which involves the same process. CCFR has measured $m_c = 1.34 \pm 0.35$ GeV/c^2 from E-744 and will cut the error to ± 0.25 GeV/c^2 when the E-770 sample is included.[8] With the statistical power available at the Main Injector, charm-production will be the largest source of error unless the error is further reduced. A Quadrupole Triplet run at the Main Injector with the same detector for our QCD studies will determine m_c to ≈ 0.1 GeV/c^2 or less, making the error acceptably small.[1]

We will also attempt to lessen the error from charm-production by (a) increasing the sampling of the detector, and (b) measuring the angle of the hadronic shower with the FADC system already developed for E-744/E-770. Since we do not observe the outgoing muon in neutral current events, all we have is the energy of the hadronic shower. By measuring its angle as well, and demanding momentum conservation about the beam direction, we can reconstruct and cut on $Q^2 = 2E_\nu E_{\nu'}\theta_H$. The Lab E detector for E-744/E-770 did not have

[1]This is just one place where the two halves of the Tevatron program are complementary; it is also true that an accurate measurement of $|V_{cd}|$ from P–803, discussed later, will be of great help here. Hence the medium and high energy programs are also mutually beneficial.

the resolution necessary to cut on Q^2; by doubling the sampling we expect to bring the resolution on θ_H down to the 10–15 mr necessary to make use of this technique.

2.2 Nucleon Structure Functions and Precision Measurements of QCD

Precise measurements of structure functions have been the most significant product of past measurements. Neutrino-nucleon scattering is particularly important since it provides the cleanest measurement of xF_3. By determining $\partial \ln xF_3/\partial \ln Q^2$ we measure $\alpha_S(Q^2)$ and can extract Λ_{QCD} with an error of ± 15 MeV. The quantity $R_{QCD} = F_2/2xF_1$ has never been adequately measured; although measurements at low Q^2 at SLAC have been performed, R at Tevatron energies has never been cleanly distinguished from zero, let alone shown to be consistent with QCD.[9] Precision tests of perturbative QCD, and "the best way" of achieving them, is a subject of some controversy arising largely due to the uncalculable contributions from "nonperturbative" effects.[10,11] Nevertheless, within the framework of deep-inelastic experiments, there exist elegant and unambiguous predictions that could be directly tested against measurements. Such a program (P–815 Phase II) would first restore the high-flux, high-energy Quadrupole Triplet. With ten times the integrated flux of the last Quadrupole Triplet runs we would have the samples shown in Table 2.1.

Table 2.1: The Proposed Statistical Sample in P-815 Phase II. Number of $\nu(\bar{\nu})$-induced charged current (CC), neutral current (NC), and charm-induced opposite sign dimuon ($\mu^-\mu^+$) events in the new experiment, are presented below.

Experiment	ν_μ-CC	$\bar{\nu}_\mu$-CC	NC	$\mu^-\mu^+$
E744 + E770	1.4×10^6	0.3×10^5	0.4×10^6	1×10^4
New Experiment	15×10^6	5×10^6	5×10^6	15×10^5

We remind the reader of the definitions of the relevant structure functions:

$$2xF_1(x,Q^2) = q(x,Q^2) + \bar{q}(x,Q^2) \tag{2.8}$$

$$xF_3(x,Q^2) = q(x,Q^2) - \bar{q}(x,Q^2) \tag{2.9}$$

$$F_2(x,Q^2) = q(x,Q^2) + \bar{q}(x,Q^2) + 2k(x,Q^2) \tag{2.10}$$

where a sum over quark species is understood. The variable R is defined through

$$F_2(x,Q^2) \;=\; \frac{2xF_1(x,Q^2)(1+R(x,Q^2))}{1+4M_N^2x^2/Q^2} \tag{2.11}$$

and reflects the spin-0 content of the nucleon. This term arises from the gluon component along with "intrinsic" p_T of the quarks within the nucleon.[2]

Two compelling tests of QCD within deep inelastic experiments are the evolution of structure functions with Q^2 at fixed x and the dependence of R (σ_L/σ_T) on x and Q^2.[12]

The evolution of the parity violating structure function $\partial ln(xF_3)/\partial ln(Q^2)$ is the simplest. It is free of the details of gluon densities or the knowledge of R and therefore provides the cleanest channel for testing the Q^2 evolution predicted by the theory.[13]. Specifically, the leading-order evolution equation at fixed x is:

$$\frac{\partial \ln xF_3(x,Q^2)}{\partial \ln Q^2} = \frac{\alpha_S}{2\pi}\frac{4}{3}\left[\int_x^1 dz\,\frac{1+z^2}{1-z}\left[\frac{x}{z}F_3(\frac{x}{z},Q^2)-xF_3(x,Q^2)\right]-xF_3(x,Q^2)\int_0^x dz\,\frac{1+z^2}{1-z}\right] \tag{2.12}$$

This complicated-looking equation breaks into two simple parts: (1) an overall factor of α_S and (2) an integral proportional to xF_3 itself. Hence the logarithmic derivative can be measured with almost no theoretical complications.[3] The new CCFR QTB-data[12] demonstrate, for the first time, a Q^2-evolution of xF_3 consistent with the Altarelli-Parisi equation. The statistical and systematic precision of the earlier measurements of xF_3 in the narrow band beam data of CCFR[14] and the wide band data of CDHSW[15] were such that the test was inconclusive.[11]

Next, since (to first-order)

$$\alpha_S = \frac{4\pi}{(11-\frac{2}{3}n_f)\ln\frac{Q^2}{\Lambda^2}} \tag{2.13}$$

(where n_f is the number of quark flavors) we can use the xF_3 evolution to determine Λ_{QCD}. The primary systematic uncertainty will be the relative calibration between the hadronic energy measured by the calorimeter and muon momentum from the toroids. This will smear the events to different values of x and Q^2, thereby altering the derivatives.

The next goal for QCD tests is a demonstration of $R_{EXPT} = R_{QCD}$. Fortunately, perturbative QCD predicts the absolute magnitude and shape of $R(x,Q^2)$ which can then be confronted in an deep inelastic scattering experiment.[16] Current data are consistent with R_{QCD}, but they are also consistent with R constant.[17] With an order-of-magnitude more data, a precise test could be made.

[2]This is a complicated topic and we can only collect formulae here. For reviews, see [9] and references therein.

[3]The second-order evolution equation is considerably more complicated but by the nature of the Altarelli-Parisi equations requires no new information.

We also point out the power of neutrino scattering in determining the gluon structure function. We evolve both

$$F_2^{\nu(\bar{\nu})} = 2[xq^{\nu(\bar{\nu})} + x\bar{q}^{\nu(\bar{\nu})} + 2xk^{\nu(\bar{\nu})}] \quad (2.14)$$

$$xF_3^{\nu(\bar{\nu})} = 2[xq^{\nu(\bar{\nu})} - x\bar{q}^{\nu(\bar{\nu})}] \quad (2.15)$$

where the k term represents the spin-0 component from the gluon distribution $G(x, Q^2)$ (and from higher-order QCD effects). By simultaneously evolving both of these structure functions, we put contraints on the gluon distribution (since the integrals of F_2 and xF_3 are fixed).

The statistical strength of the new experiment permits the extraction of quark and antiquark distributions separately for neutrinos and antineutrino. Hence we may also test the assumption that the structure functions are the same for neutrinos and antineutrinos.

Furthermore, the only direct measurement of the strange sea comes from a study of neutrino induced opposite sign dimuon events.[8] The 150,000 opposite sign dimuons in Phase II will give an unprecedented determination of the strange sea density including its Q^2 evolution. The traditional quark-parton model integral tests, such as the Gross-Llewellyn Smith sum rule and the mean square charge test will be significantly improved as well.

2.3 Rare Processes

With a factor of ten greater statistics than ever before and a significantly upgraded detector, limits on and searches for rare processes will be greatly improved. In particular, searches for neutral heavy leptons and wrong-sign muons will be improved by an order-of-magnitude and we may set significantly improved limits for $\nu_\mu \to \nu_\tau$ oscillations at large Δm^2. We describe some others below:

Inverse Muon Decay The purely leptonic reaction, $\nu_\mu + e^- \to \mu^- + \nu_e$, offers an elegant test of the model. We could learn the structure of the Lorentz current of the weak interaction, the scalar coupling of leptons, as well as the energy dependence of its cross section. It offers an absolute normalization of ν-events.[18]

Measurement of V_{cd} Opposite sign dimuons have been the direct means of measuring the Cabibbo-Kobayashi-Maskawa matrix element. The present measurements could be vastly improved.[8]

Neutrino Tridents Measurement of the destructive interference between the neutral current and charged current channels of neutrino scattering off the coulomb field of the nucleus (the so called ν-induced trident events) directly tests the gauge structure of the

standard model. Recently the CCFR collaboration has reported the first demonstration of the predicted destructive interference between the W and Z channels in neutrino tridents.[19]. The new experiment, which would observe more than 600 tridents, would permit a precise test ($\geq 6\sigma$) of this important Standard Model prediction.

Neutral Heavy Leptons Neutrino experiments are sensitive to iso-singlet type neutral heavy leptons (as opposed to sequential fourth generation neutrinos). These leptons are not excluded by the LEP data, and would continue to be of interest even with 10^7 Z^o events from LEP. The current best limits in the appropriate mass regions come from the CCFR searches.[21] For low mass neutral heavy leptons (< 5 GeV), the sensitivity in the new experiment will be far superior to the e^+e^- experiments. By instrumenting the apparatus suitably, we could extend the search domain with masses down to 10 MeV and with coupling suppressions down to 10^{-9}.

Search for Right Handed Currents The y-distributions of neutrino and antineutrino CC events constrain the right handed currents in the most model independent way. The current limit on the mixing of the right handed currents from the CCFR(QTB) experiments is the most stringent one. The corresponding limit from muon-decay is-sensitive to the theoretical assumptions such as the mass of the right handed neutrino. In the new experiment the derived limit on the mass of the right handed boson should be the most stringent.[20]

Trimuons Neutrino-induced trimuons predominantly arise from hadronic sources (vector meson resonances). The new sample should have over 1300 of these events; offering an opportunity to do a quantitative test of various hypotheses.

The Tevatron program thus offers a varied program with both significant potential for new discoveries as well as precise measurements of fundamental quantities. We conclude with a description of changes which will be needed in the Lab E detector.

2.4 P-815 Detector Upgrades

P-815 will need to significantly upgrade the Lab E detector both for the electroweak measurements and for its precision tests of QCD. Improvements will be made to both the calorimeter and to the magnetic measurement system. The changes in the calorimeter do not require new techniques although they will require significant construction. The upgrades to the calorimeter will be studied and finalized in P-815 Phase I. We hope to test options for the magnetic measurement upgrade at that time; one option, an air-core toroid, is a major construction project and much more work is required before we can realistically assess the requirements. It is important, therefore, to realize that the Phase II proposal has not been prepared and that this design is preliminary. A schematic of the present Lab E detector, used for the CCFR runs of E-744 and E-770, is shown in Fig. 2.4.

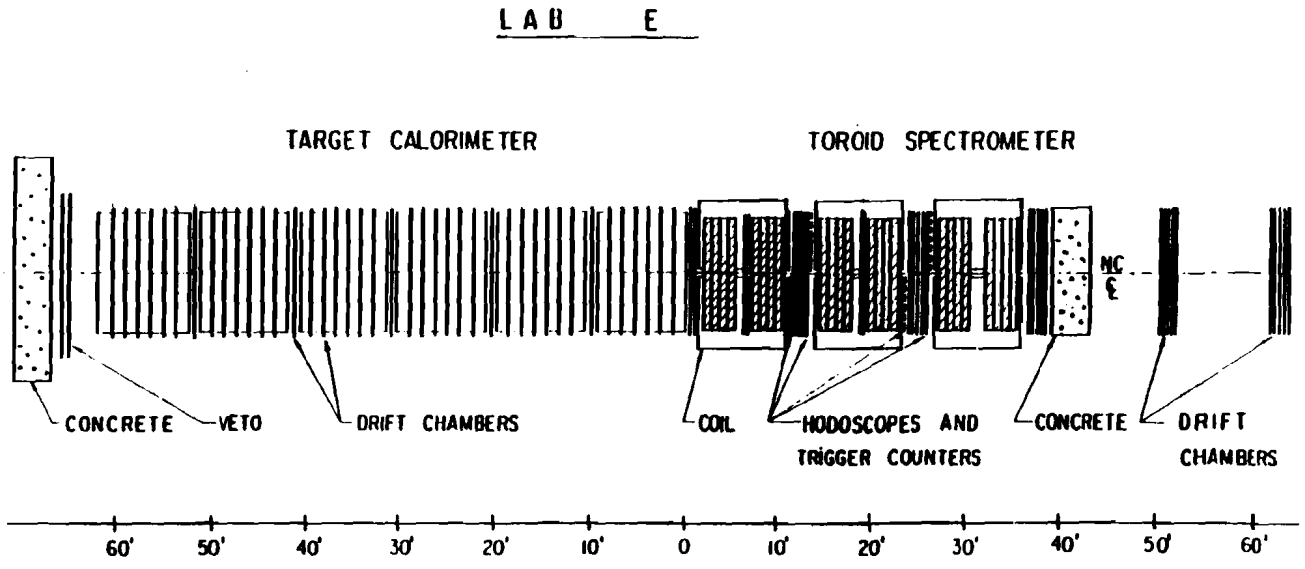

Figure 2.4: The Lab E detector for the Quadrupole Triplet runs of E-744/E-770.

2.4.1 Calorimeter

The calorimeter must be improved for three reasons: (1) to provide a better measurement of the hadronic shower angle θ_H and (2) to provide better tracking for low-energy and/or wide-angle muons, and (3) to improve the separation of electromagnetic and hadronic showers. Each of these improvements will primarily affect the electroweak measurements. Two changes will be made to the calorimeter, and these changes will be studied in P-815's 1993 run. A schematic of the arrangement of Fe, scintillators, and drift chambers is given in Fig. 2.5.

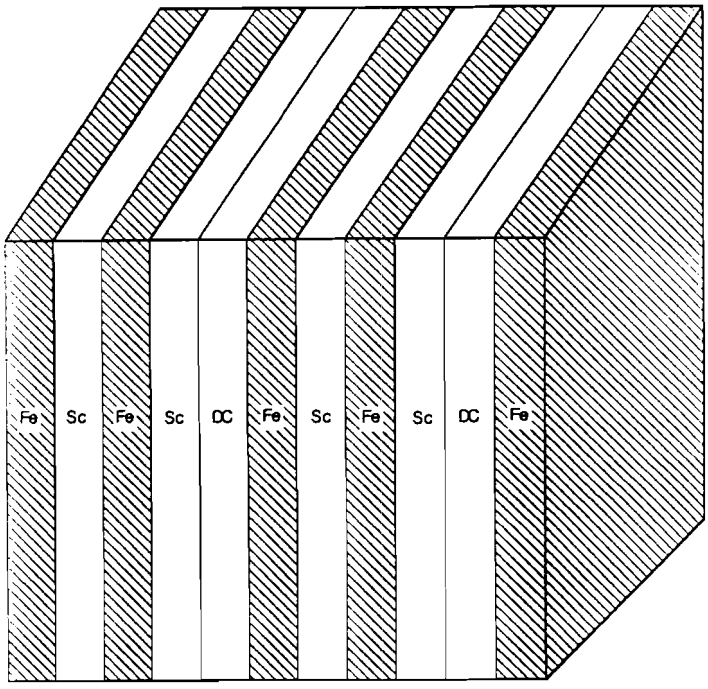

Figure 2.5: Enlarged View of a Section of the P–815 Calorimeter; not to scale. Each iron plate is 2 in thick. The entire calorimeter is 10 ft by 10 ft and the unit shown is repeated 42 times.

Scintillation Counters

The first change will be to provide transverse segmentation in the calorimeter. The current Lab E counters are 10 ft. by 10 ft. liquid scintillation counters. These will be made into solid scintillator strips with sampling every 2 in. of Fe instead of the current 4 in. A schematic of one possible plane is given below; the 1993 run will determine the final dimensions and arrangement. We see nine 1 ft. strips and two 6 in. strips on the outside. The outside, smaller strips will serve to tag exiting muons. Muons which exit before traveling downstream of the hadronic shower are potential condidates for crosstalk from the *CC* denominator to the *NC* numerator of R_ν, as discussed in Sec. 2.1.3.

The increased longitudinal sampling would also be of great help in distinguishing electromagnetic from hadronic showers. If we could detect charged-current ν_e interactions, a significant source of background would be eliminated. Electromagnetic showers have a maximum at typically 4 in of Fe (5.7 X_o) which is the same as the current sampling. Hence it is difficult to accurately determine the longitudinal profile. While the Lab E detector will never be able to follow the development precisely, a factor of two improvement in the sampling length would make the distinction clearer. GEANT studies are currently underway on this issue.

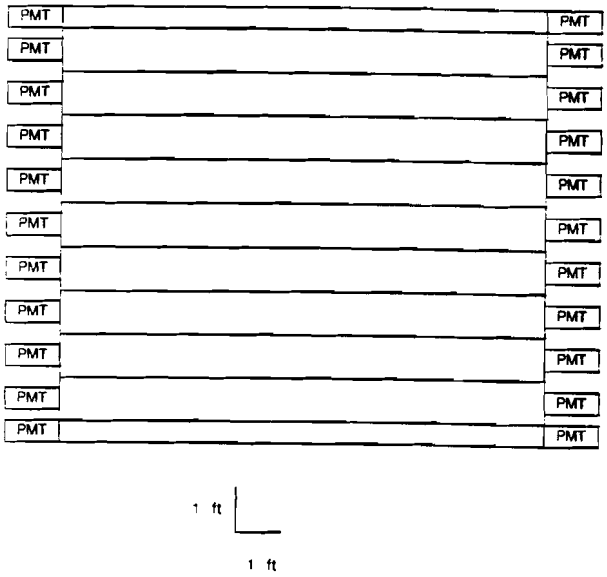

Figure 2.6: A schematic of a possible scintillator plane for P-815. There are 14 such planes and an additional 14 rotated by 90° for each of seven carts. The two counters at top and bottom are 6 in wide; the rest are 1 ft. All are 10 mm thick.

Such an array would require 4224 phototubes and 19200 sq. ft. of scintillator.

Drift Chambers

The primary error in the electroweak determinations will be the error on the charm-mass, m_c, used in the slow-rescaling parameterization. A Q^2 cut would eliminate the dependence but we would need to measure Q^2 in both the *NC* numerator and the *CC* denominator to avoid biases as explained earlier. The drift chambers in the target are seen by FADC's which we will use for accurate measurements of θ_H; a weighted momentum vector of hits in the shower is formed which then gives the shower angle. A plot from test run data in E-744/E-770 is shown in Fig. 2.7.

We will require a measurement accuracy of 10–15 mr. which will require doubling the

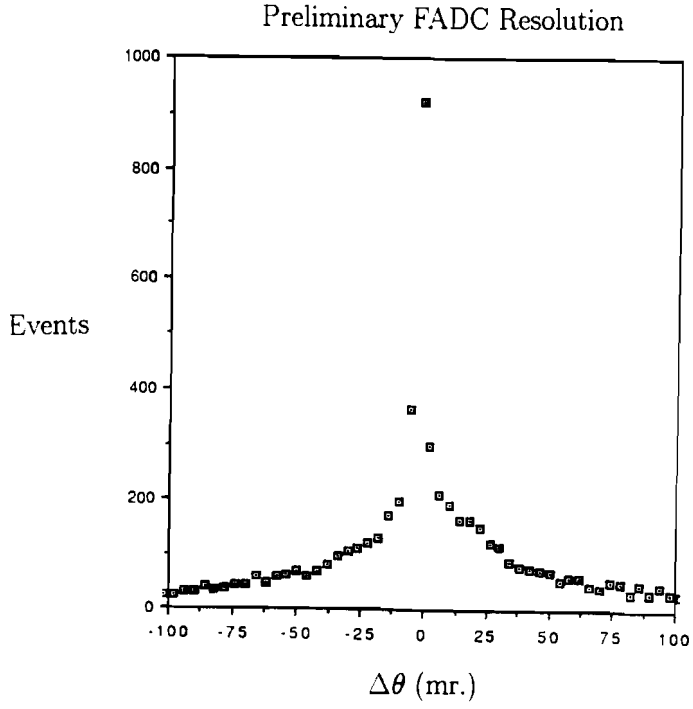

Figure 2.7: Preliminary Hadron Shower Angle resolution from E-744/E-770 using FADC's. P-815 will have twice the number of chambers which will improve the resolution.

number of chambers. Since the chambers were designed and constructed at Fermilab, and many of the personnel involved are still present at the Lab (two are collaborators on P-815) building an additional set should be a relatively straightforward task.

2.4.2 Spectrometer

The QCD tests, particularly the measurement of Λ_{QCD}, require that the relative calibration between E_H and p_μ must be improved to $\delta(p_\mu - E_H) = \pm 0.05\%$. Event-by-event errors here are less important than the overall calibration of the difference, and so multiple scattering in the toroid iron is not a direct problem.

No straightforward method of improving E_H exists, but the muon momentum measurement can be improved in one of three ways:

An improved alignment system would remove one of the difficulties in the calibration of muon momentum from the E-744/E-770 analysis. Although the surveying was done to an accuracy of 0.010 in, rotations of chambers (in x, y, and z) were present and caused discrepancies of up to 0.1 in. when a internal calibration to the data was performed. A system of mounts which eliminated these rotations and more accurate surveying technique should reduce these discrepancies to the 0.01 in. level, consistent with the errors on internal placement of wires within the chambers. A design for an improved system is just beginning and we hope to have it completed in the next year so that we may test it in P-815 Phase I.

It would also be possible to construct a new toroid system. The current Lab E toroid is constructed of laminated sheets instead of solid iron; this may induce irregularities in the field. The field measurement could be made more precise and a new design could include a systematic arrangement of probes to map out the field. The toroids could also be made larger to reduce effects from fringe fields and variations within the fiducial volume. Combined with an improved alignment system, such a new toroid could minimize many of the problems associated with the old system.

An air-core toroid[22] would remove multiple scattering and lead to a far more precise event-by-event determination of the momentum. A few of the advantages of the air-core are

- The field is completely determined by the coil geometry and current. Hysteresis in the iron or variations in the material are eliminated as sources of systematic effects.
- Tracking will be free of multiple scattering and make the pattern recognition and momentum reconstruction easier and more precise.

Ref. [22] concluded that a ± 10 MeV measurement of Λ_{QCD} could be obtained with such a device while retaining an iron toroid would imply an error of 20–50 MeV. Hence the air-core

is clearly superior; the decreased error must be balanced against the cost and difficulty of construction. This poses a clear question for the experimenters and studies of the alternatives are underway.

2.4.3 Triggering, Data Acquisition, and Logic

The triggering, data acquisition, and logic for E-744/770 will be more than adequate for the P-815 program if we make small modifications to the system. We will require that the number of fast extractions be doubled to approximately 6–8 in order to keep the live-time over 90% (we are dominated by the time for readout of the FERA system for our ADC's) and have acceptably small accidental backgrounds for some of the rare decay searches. This presents no special problems for the accelerator but methods of making the fast-spill extraction less disruptive to slow-spill users are being studied. The 120 GeV program will be unaffected by fast resonant extraction in the Tevatron program.

References

[1] P–815 proposal and references therein. Also see S. R. Mishra, A 2nd Generation Neutrino Experiment at the Tevatron, Physics at Fermilab in the 1990's, Breckenridge, Col.

[2] R. Bernstein in Physics at Fermilab in the 1990's, to be published. Also see the P-815 proposal.

[3] R.G. Stuart, Z. Phys. C34, 445(1987).

[4] M. Shochet *etal.*, CDF/D0C/CDF/PUBLIC/1152, (1990).

[5] C.H. Llewellyn Smith, Nucl. Phys. B228 (1983) 205.

[6] E.A. Paschos, L. Wolfenstein, Phys. Rev. D7 (1973) 91.

[7] H. W. Atherton, CERN 80-07. Also see A. Malensek, FN–341.

[8] C. Foudas *et al.*, Phys. Rev. Lett., (1990); For recent experimental results from CCFR, see M. Shaevitz in Proc. of Neutrino '90.

[9] S.R. Mishra and F.J. Sciulli, Phys. Lett. B244, 341(1990).

[10] G. Altarelli, "Tests of QCD ", Ann. Rev. Nucl. Part., 39, 366 (1989).

[11] S.R.Mishra and F.Sciulli, "Deep Inelastic Lepton-Nucleon Scattering", Ann. Rev. Nucl. Part., 39, 259 (1989).

[12] S.R.Mishra, "Probing Nucleon Structure with ν-N Experiments", Nevis Preprint # 1426; to appear in the proceedings of "Workshop on Hadron Structure Functions and Parton Distributions", Fermilab, Batavia, Ill, Apr(1990).

[13] G. Altarelli and G. Parisi, Phys. Lett. B26, 298(1977).

[14] E. Oltman, PhD thesis, Columbia University, Nevis-270, Apr(89); to be published.

[15] B. Vallage, PhD thesis, Saclay CEA-IV-2513, Jan(87); to be published.

[16] G. Altarelli and G. Martinelli, Phys. Lett. B76, 89(1978); M. Gluck and E. Reya, Nucl. Phys. B145, 24(1978).

[17] S. R. Mishra and F. Sciulli, Phys. Lett. B244, 341(1990).

[18] CCFR: S.R.Mishra *et al.*, Phys. Rev. Lett. 63, 132(1989).

[19] S. R. Mishra *et al.*, "Neutrino Tridents and $W-Z$ Interference", Nevis Preprint #1430, Dec. 1990; submitted to Phys. Rev. Lett.

[20] CCFR: S.R.Mishra et al., "A Study of the Space-Time Structure of the Weak Current in ν-N Scattering"; Nevis preprint #1428; submitted to Phys. Lett. B.

[21] S. R. Mishra *et al.*, Phys. Rev. Lett., 59, 1397(1987). Also P. De Barbaro, A Search for Neutral Heavy Leptons in $\nu_\mu N$ Interactions, in New and Exotic Phenomena '90, Rencontres de Moriond, Jan. 1990, Editions Frontières.

[22] An air-core toroidal spectrometer is being considered by the Saclay-Munich group to conduct a second generation deep inelastic muon experiment. See, C. Guyot *et al.*, "A New Fixed Target Experiment for a Precise Test of QCD", to be published in Proceedings of "Fermilab in the 1990's", ed. R. Brock and H. Montgomery.

3 Long-Baseline Oscillation Experiments

3.1 Physics Motivation for Long Baseline Experiments

The Main Injector at Fermilab and its high-intensity neutrino beam will make possible the first long-baseline oscillation experiments using accelerator neutrinos[1,2,3]. Such experiments would provide sensitivity to neutrino masses in a range previously unexplored under well-controlled laboratory conditions. The extraordinarily high intensity, excellent collimation, and high energy provide tens of thousands of measured events in a typical exposure of a long-baseline detector. Moreover the proposed beam provides purity of flavor at the one percent level with negligible error in the estimate of flavor contamination and energies high enough so that nuclear effects are negligible. The energy is also high enough that the ν_τ can be detected by its charged current interaction. Improvements in flux, energy spectrum, composition, and control of experimental parameters which will be offered by the Main Injector neutrino beam are nearly as impressive as those enjoyed by high energy physicists in the transition from the cosmic radiation to accelerators for beams.

The motivation for searching for neutrino oscillations predates the recent hints from non-accelerator experiments. Neutrino oscillation experiments directly test conservation of lepton number. Lepton number conservation *has been* an observed symmetry of nature, but *is not* a fundamental requirement of the Standard Model; indeed, grand unified theories require its violation. The mixings between quark generations expressed in the CKM matrix may have analogous non-diagonal elements in a neutrino mixing matrix. Neutrino oscillations may exist at small Δm^2 with couplings too small to have been detected by previous experiments. The combination of the low energy beam and large distances provides a considerable leap in parameter space, about two orders of magnitude lower Δm^2 for $\nu_\mu \rightarrow \nu_\tau$! This is complementary to the short baseline experiment P803 which will also improve the coverage in parameter space by more than an order of magnitude in mixing angle.

As we discuss below, there is mounting evidence that a specific region at small Δm^2

should be carefully explored (although the vast increase in parameter space is sufficient impetus in itself). The suggestion that neutrinos oscillate with parameters accessible to long-baseline experiments is based on two separate experiments:

- A result on the flavor composition of atmospheric neutrinos can be explained by $\nu_\mu \rightarrow \nu_\tau$ (or $\nu_\mu \rightarrow \nu_e$) oscillations in this region of parameter space ($\sin^2 2\theta > 0.1$, $\Delta m^2 \sim 10^{-2}\text{eV}^2$)
- The explanation of the solar neutrino problem as matter enhanced $\nu_e \rightarrow \nu_\mu$ oscillation (MSW effect) coupled with a reasonable see-saw mechanism[4] for the mass hierarchy of lepton families again leads to $|m^2_{\nu_\mu} - m^2_{\nu_\tau}| \sim 10^{-1}$–$10^{-2}$ eV^2.

We further discuss these two kinds of experiments in the next two sections.

3.2 Atmospheric Neutrino Deficit

Atmospheric neutrinos are produced primarily from the decay of π, μ and K secondaries in showers created by the primary cosmic ray flux. Several underground detectors can detect the interactions of these atmospheric neutrinos and thereby measure the neutrino flavor composition (ν_μ/ν_e), energy spectra, and angular distribution of atmospheric neutrinos. These observations of flavor composition and angular distribution provide a test for neutrino oscillations.

To date, the experiments observe some depletion of the muon neutrino flux at the level of 2–3 standard deviations but the evidence is not conclusive. In order to avoid the 20% uncertainty in the absolute fluxes of atmospheric neutrinos, these experiments report the ratio of observed and predicted ratios of muon and electron neutrinos:

$$r = \frac{(\nu_\mu/\nu_e)_{measured}}{(\nu_\mu/\nu_e)_{predicted}} \tag{3.1}$$

The predicted ratio is known[5] with an accuracy better than 5%. Uncertainties in the nuclear effects on the cross sections, flavor dependent trigger efficiencies, and pattern recognition probabilities for separating electrons from muons contribute to systematic effects which presently limit the accuracy with which this ratio can be determined.

The Kamioka experiment[6] has reported this ratio with the best accuracy, $r = 0.71 \pm 0.08$. More recently, IMB-3[7] presented a preliminary result $r = 0.67 \pm 0.18$ (following an earlier report of a deficit of muon decay signals in IMB-1). The fine-grained tracking detector Frejus[8] reported a value $r = 1.01 \pm 0.10$, although an analysis[9] of fully contained events gives $r = 0.80 \pm 0.08$. A similar detector, Nusex[10], obtained a value of r consistent

with unity with much lower statistics. The results from the high-statistics, low-systematics analyses as a whole show a 20–30% deficit, but the interpretation is by no means clear.

If one interprets [11] the Kamioka result as a signal for $\nu_\mu \rightarrow \nu_\tau$ oscillation, the measured event composition, the measured energy spectra, and the angular distributions indicate the most probable value of Δm^2 is 10^{-2}eV^2 and the mixing angle $\sin^2 2\theta$ is 0.69. This point is plotted in Fig. 3.1. The region between the dot–dashed lines is the 90% CL Δm^2–$\sin^2 2\theta$ region *allowed* by one analysis from Kamioka. The regions excluded by accelerator experiments, Frejus and IMB1 are also shown. The region allowed by all experiments at 90% CL is outlined.

3.3 Solar Neutrino Puzzle

The flux of solar neutrinos has been monitored for over two decades by the Davis chlorine experiment[12] and more recently by the Kamiokande[13] detector. The Kamioka experiment, which observes neutrino-electron scattering was also the first experiment to measure the directionality of their signal, thus identifying neutrinos from the Sun. Data from both experiments taken during the same time period yield only about half of the predicted neutrino flux in the energy range above ~ 7 MeV. Preliminary results of the gallium experiment, SAGE, which is sensitive to lower energy neutrinos produced in the main solar cycle, may indicate a large deficit of the neutrino flux. These results on solar neutrinos leave us with a choice: either there is a mechanism making neutrinos undetectable or the Sun's energy generation process is grossly misunderstood. The hypothesis [14,15,16,17,19] of neutrino oscillation due to a small mass difference ($\Delta m^2 \sim 10^{-4} - 10^{-7}\text{eV}^2$) between ν_e and ν_μ together with the MSW mechanism, is a very natural candidate to explain the observed solar neutrino flux depletion. If this hypothesis is correct, a theoretically motivated see-saw mechanism[4] for neutrino masses would put the difference of Δm^2 for ν_μ and ν_τ in the range of $\approx 10^{-2}\text{eV}^2$.

The results are tantalizing but less than completely persuasive. Both the atmospheric and solar neutrino problems rely on common calculations using theoretical simulations. The errors on r in the atmospheric studies are believed to be under 5%, but unknown systematic errors could bias the interpretations. A new generation of experiments must be able to establish a positive signal without these complications at a convincing level of statistical significance. A long baseline experiment with a beam from the FNAL Main Injector can improve on the raw statistics by several orders of magnitude, but more importantly, with a beam of much purer and better known composition and with an energy spectrum which peaks at energies which are much more favorable for detection.

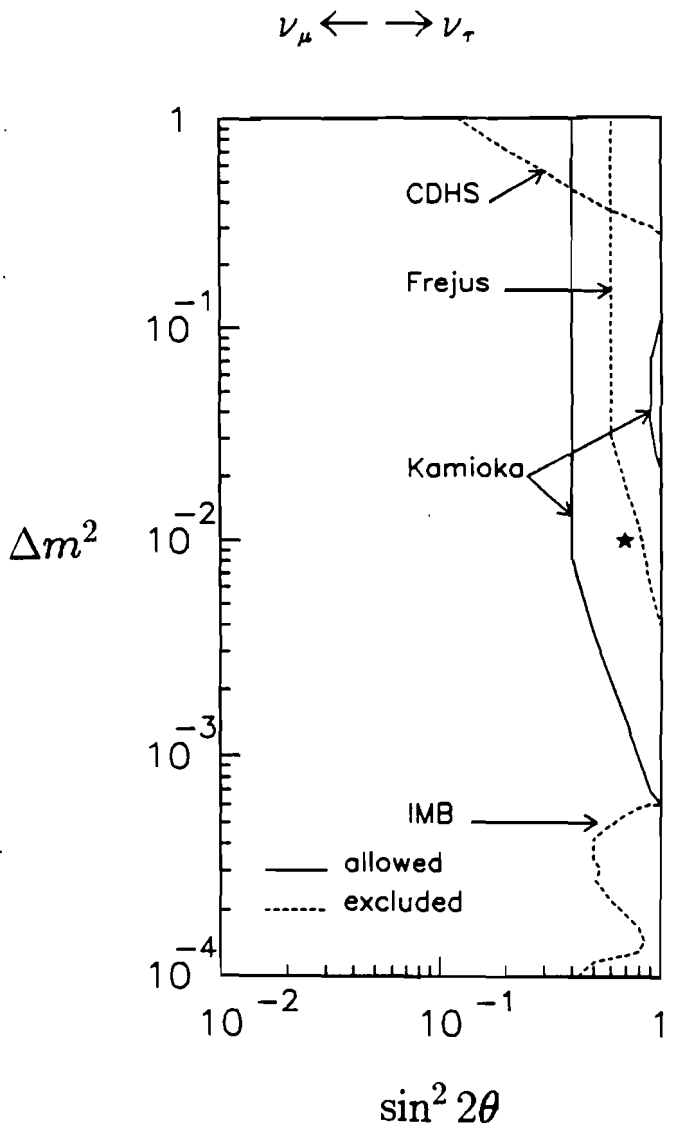

Figure 3.1: Regions of parameter space *allowed* by one Kamioka analysis for $\nu_\mu \rightarrow \nu_\tau$ and excluded by accelerator experiments, Frejus and IMB1.

3.4 Capabilities of Long Baseline Neutrino Detectors

Laboratory experiments have set upper limits on neutrino masses in the range of a few eV for ν_e and in the MeV range for the other flavor neutrinos, while the masses suggested by solar and atmospheric neutrino measurements are considerably smaller. There is then no prospect of mass measurements using kinematics in this range; the most promising technique for obtaining information about these small masses appears to be interference experiments such as have been used to determine the K_L^0 and K_S^0 mass differences. The solar deficit is an example of such an experiment, although the energy of solar neutrinos is below threshold for detecting oscillations by observing ν_μ or ν_τ charged current interactions.

If neutrino oscillations exist, the probability (P) goes as

$$P_{\nu_a \to \nu_b} = \sin^2 2\theta \, \sin^2(1.27 \, \Delta m^2 \, \frac{L}{E_\nu}) \tag{3.2}$$

with Δm^2 in eV^2, L in km and E_ν in GeV. $\Delta m^2 = |m^2_{\nu_a} - m^2_{\nu_b}|$ and θ is the mixing angle between ν_a and ν_b neutrinos. In order that the energy be high enough for clean identification of the flavor through observing charged current events, it is clear that the very small mass differences which appear to be interesting imply long baseline experiments. A baseline of 500 km or more extends the Δm^2 sensitivity downward by two orders of magnitude from all previous accelerator experiments. Without the large neutrino flux from the Main Injector, experiments at this distance would have only a handful of events: a "similar" experiment using the Tevatron would have eight hundred times fewer events and would thus not be sensitive to the interesting range of Δm^2. Only the Main Injector combines the high flux with the right energy range for these experiments.

The sensitivity to mixing angle that can be achieved depends on statistics and control of systematic errors[1,20]. One of the most important elements of systematic error in these experiments will be the understanding of the neutrino beam itself to sufficient accuracy. An important tool in understanding the long baseline beam would be measurements done in the same beam by the short baseline experiment (P803) or by a dedicated short baseline detector.

In order to conduct a long baseline neutrino oscillation experiment it is necessary to have a beam of neutrinos of large enough flux and a large detector at the appropriate distance. The large distances require a dedicated beam pointing at the detector. Until now there has not been an accelerator which would provide a sufficiently large flux of neutrinos to make a long baseline experiment feasible. The Main Injector, producing 3×10^{13} protons every 1.9 seconds at 120 GeV, will be the first accelerator fulfilling this requirement. Fortunately, several large neutrino detectors suitable for such an experiment (target mass in the kiloton range at distances of 500–6000 km) exist or are under construction.

Fermilab has received two proposals to performlong baseline oscillation experiments. The

first was from IMB, a 6.8 kton water detector at a distance of 570 km. The second was from Soudan-2 (P822), a 1.1 kton iron calorimeter under construction at a distance of 806 km from the Main Injector. DUMAND (P824), a 2 Mton Čerenkov detector to be placed in the deep ocean near the island of Hawaii, 6000 km away has submitted a letter-of-intent. Other large detectors or a new detector might also be considered.

All of these detectors can record neutrinos interacting either inside the detector (contained signal) or in the material surrounding the detector (entering signal). The size of the contained signal is proportional to detector mass and the entering signal to the detector surface area facing the neutrino beam front. Both signals are inversely proportional to the square of the distance separating neutrino source and detector.

The different detectors which might be used in a long baseline neutrino experiment have various capabilities, but all will look for a decrease in the ν_μ flux due to possible oscillations and all will detect signals from interactions in the material in front of the detector as well as from contained events. The ν_μ's interacting in the earth will create muons that have a range which increases with higher muon energy. As muons range out, new ones are created by charged current interactions, so at any point along the beam there should be a constant muon flux per unit solid angle, which is approximately independent of density. The long range of muons from high energy neutrinos provides access to an effective target mass which may be much larger than the mass of the detector.

The IMB collaboration has carefully studied the potential systematic effects on the ratio of entering muons to contained events,

$$R_{\mu/\nu}(E) = \frac{\Phi(1-P_{\nu_\mu})\sigma^{cc}_{\nu_\mu} M_{eff}}{\left(\Phi\sigma^{nc} + \Phi(1-P_{\nu_\mu})\sigma^{cc}_{\nu_\mu} + \Phi P_{\nu_\mu}\sigma^{cc}_{not\ \nu_\mu}\right) M_{det}} \tag{3.3}$$

where $\Phi(E)$ is the flux of ν_μ, $P_{\nu_\mu}(E)$ is the probability of a ν_μ oscillation, M_{det} is the fiducial mass of the detector, and $M_{eff}(E)$ is the effective target mass in the upstream rock for neutrinos of a given energy E to create a muon which reaches the detector. Potential problems due to beam pointing, uncertainties in the energy distribution of the beam, the geometry of the detector and its surrounding and properties of the surrounding matter have all been considered. No effects have been identified which would introduce uncertainties larger than 1% in the measurement of $R_{\mu/\nu}$. An overall accuracy of this parameter of the order of 2% is expected. The absolute beam flux, which would have an uncertainty of at least 10%, cancels out in the above equations.

Equation 3.3 provides sensitivity to the cases $\nu_\mu \rightarrow \nu_\tau$ and $\nu_\mu \rightarrow \nu_e$. Measurement of neutrino oscillation to a sterile species, such as right handed neutrinos (ν_R) would rely on the absolute beam flux. These various oscillation hypotheses would affect event rates in different ways as summarized in Table 3.1.

	$\nu_\mu \rightarrow \nu_\tau$	$\nu_\mu \rightarrow \nu_e$	$\nu_\mu \rightarrow \nu_R$
# entering $\mu's$	1 - $\sim \mathcal{P}$	1 - $\mathcal{P}$	1 -$\mathcal{P}$
# contained events	1 - 0.5 $\mathcal{P}$	1	1 - $\mathcal{P}$
ratio $R_{\mu/\nu}$	1 - $\sim$0.5 $\mathcal{P}$	1 - $\mathcal{P}$	1

Table 3.1: Changes in Observed Beam Fractions from Oscillations. $\mathcal{P}$ is the probability of oscillation suitably averaged over the energy spectrum.

3.5 Possible Long Baseline Detectors

3.5.1 IMB

Features of the Detector

The IMB detector is located in the Morton Salt mine near Cleveland, Ohio about 600 m below the surface and 570 km from Fermilab. A beam aimed towards the detector points almost due east and downward with an angle of about 45 mr with respect to the horizon.

The detector consists of a rectangular volume (17 m $\times$ 17.5 m $\times$ 23 m) of highly purified water, viewed by 2048 photomultipliers augmented with waveshifter plates. It has operated with high reliability since 1982, and has set significant limits on proton decay, measured properties of atmospheric neutrinos, and detected the burst of neutrinos from SuperNova SN1987A. The detector resolves the patterns of Čerenkov light from muons entering the detector and from individual products of neutrino interactions in the detector volume.

The detector trigger threshold of 10 MeV is far below the requirements of the proposed oscillation experiment. The 2.7 Hz rate of cosmic ray muons passing through the detector produces only 1% dead time. A system of clocks recording the absolute time of every detector trigger and every spill of the neutrino beam eliminates the necessity for directly gating the detector.

The detector has the capability of resolving showering (e, π^0) from nonshowering $(\mu, \pi^\pm)$ tracks but it cannot resolve electrons from π^0's with energies above 500 MeV.

Assuming that the Main Injector will provide 3×10^{13} protons of 120 GeV energy with the repetition time of 2 sec, one can expect that IMB would record 2.6 neutrino interactions in the detector volume and 5.2 muon tracks entering the detector per hour associated with the beam. A signal of this size would result in 1.3% statistical accuracy after half a year of data collection for the sample of contained events. The background to this signal due to

interactions of atmospheric neutrinos is of the order of 10^{-6}.

$R_{\mu/\nu}$ test for $\nu_\mu \rightarrow \nu_\tau$

The experiment will measure the rate of neutrino interactions in the detector volume associated with the beam and the rate of tracks entering the detector. Since the rock surrounding the IMB detector has density about 3 times larger than water, the contamination of other than muon tracks in this sample is expected to be only about 4%. The ratio of these two signals is independent of the beam flux.

Both the statistics and systematic effects will determine the accuracy of the measured ratio. The statistical error will be dominated by the number of contained events. Due to large mass of their detector, IMB can collect in a half year enough contained events so that their statistical accuracy will be 1.3%, much smaller than the systematic error.

A significant component of the systematic uncertainty of Long Baseline experiments is due to the variations of the beam characteristics with an angle with respect to the beam axis, and the accuracy with which the beam is pointed towards the detector. The IMB group helped coordinate the effort to design a beam with minimum energy variation as a function of angle.[1] As a result, the mean energy of the beam described in this document varies only 1% over 0.5 mr. Since this variation is directly proportional to the error of the expected ratio, the beam pointing precision of $\pm$ 0.2 mr assures the experimental precision better than 1%. The potential 90% CL upper limit that IMB can set in the 6 month run is given in curve B in Fig 3.2.

ν_e appearance

In the IMB detector, one can resolve patterns of Čerenkov light from electron and muon tracks, but high energy π^0's are similar to electron showers. However, for the neutrino beam considered in this document, the probability of producing a π^0 with energy above 20 GeV is only about 5% of that of leptons. Thus an observation of more electron tracks with energies above 20 GeV than the expected π^0 background and the contamination of the beam by ν_e (about 1% in this energy region) would indicate $\nu_\mu \rightarrow \nu_e$ oscillation. The region of sensitivity to Δm^2–$\sin^2 2\theta$ of this experiment is similar to that of the $R_{\mu/\nu}$ test. This region seems to be well above the region considered in the explanation of solar neutrino puzzle but it has never been tested in well controlled accelerator conditions. Again, the potential 90% CL upper limit that IMB can set in a 6 month run in the absence of oscillations in this mode is shown

[1] In addition to crucial contributions to the design of the double horn beam, IMB collaborators have participated in aspects of the horn design, a new type of target for FNAL, and numerical analysis of the neutrino beam output.

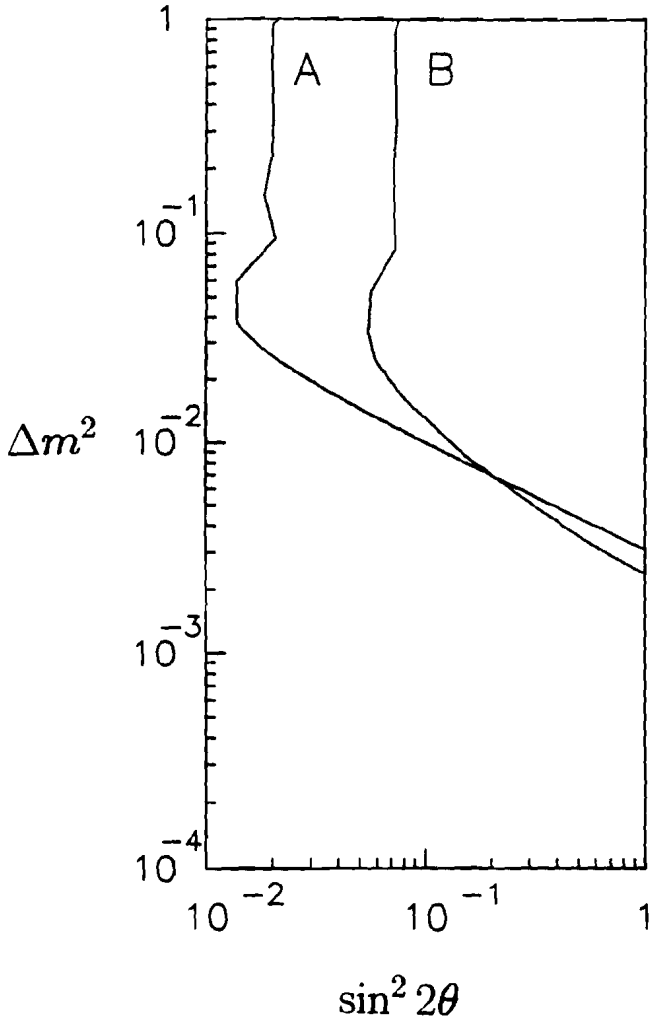

Figure 3.2: Region of 90% CL sensitivity to Δm^2–$\sin^2 2\theta$ of the IMB Long Baseline experiment to oscillations $\nu_\mu \rightarrow \nu_e$ (A) and $\nu_\mu \rightarrow \nu_\tau$ (B).

in curve A in Fig 3.2. An important systematic check available to IMB in this mode would be agreement between the excess electron events above 20GeV and a ratio of contained to entering events consistent with the $\nu_\mu \rightarrow \nu_e$ hypothesis.

3.5.2 SOUDAN 2

Description of the detector

The Soudan 2 detector (P822) is located in an iron mine in Northern Minnesota, 800 km from Fermilab. It will be an 1100 ton fine grained calorimeter (620 tons are currently in operation), consisting of 256 modules which each contain 7560 1.4-cm radius 1-m long drift tubes. Its spatial resolution and related properties are similar to those of "standard" neutrino detectors (Fermilab E594, the CHARM detector at CERN, ...). It could measure the muon rate from the Main Injector ν_μ beam both in the detector (5m $\times$ 8m $\times$ 16m) and in its proportional counter shield (11m $\times$ 14m $\times$ 24m) and normalize to the contained vertex events.

$R_{\mu/\nu}$ test for $\nu_\mu \rightarrow \nu_\tau$

Due to its larger distance and smaller size, the Soudan event rates for entering muons and contained events would be lower than IMB's by a factor of 2.2 and 11.9 respectively. The limits that Soudan 2 could obtain based on a similar $\nu_\mu \rightarrow \nu_\tau$ analysis are shown in curve C of Fig. 3.3.

Neutral current fraction test for $\nu_\mu \rightarrow \nu_\tau$

In addition, Soudan 2 could also do a ν_τ appearance experiment by looking for a deviation from the expected *NC/CC* ratio,

$$\frac{N_{nc}}{N_{cc}} = \frac{R_{nc/cc} + \eta(1-B)P}{1 - P + \eta BP} \tag{3.4}$$

where B is the branching fraction for $\tau^- \rightarrow \mu^- X$, and η is the ratio of the ν_τ charged current cross section to the ν_μ charged current cross section. Integrated over the energy distribution from the main injector, $\eta \sim .25$. $R_{nc/cc} = .31 \pm .01$ is the expected ratio in the absence of oscillations and depends only on knowledge of the Weinberg angle. The limit that can be obtained in the absence of oscillations is shown in curve B of Fig. 3.3. If neutrino oscillations actually are found to exist, there is an advantage to measure them in more than one way simultaneously and to test for consistency between the two results. Other

capabilities of Soudan 2 include a measurement of the rate of stopping muons, which gives added sensitivity at low Δm^2, and, with a high enough flux, the possible identification of single ν_τ quasi-elastic events.

3.5.3 DUMAND

Description of the detector

The DUMAND detector will measure the Čerenkov light in ocean water from charged particles produced by neutrino interactions. The array is being constructed in a subsidence basin at a depth of 4.8 km, 30 km west of Keahole Point, Hawaii. The array consists of nine strings, one at the center and at each of the vertices of an octagon 40m on a side. Each string supports 24 phototubes, 15 inches in diameter and spaced 10 m apart vertically. The spherical tubes are oriented with the photo cathode pointing downward and have a sensitivity which falls linearly with the cosine of the angle between the most sensitive direction and the direction of the incident light. A cable from shore supplies electrical power to the array and has an optical fiber for data transmission from each string. For upward muons, the signal is almost entirely due to neutrino interactions beneath the array, and the effective area of the array is 2×10^4 m^2. The location deep in the ocean provides a huge reduction in the flux of downward muons. In the upward going hemisphere, the isotropic background from neutrinos which are due to cosmic ray interactions in the atmosphere is 1/3 event per bin of angular resolution size per year.

A prototype detector[21] has been used to measure[22] the downward flux of muons in the deep ocean (4 km) and the construction is proceeding with one third of the detector elements scheduled for installation by the end of 1992 and the remainder by the end of 1993.

$R_{\mu/\nu}$ test for $\nu_\mu \rightarrow \nu_\tau$

Neutrinos from a Fermilab beam would intersect the DUMAND array at an angle 30° below the horizontal, well within the region of best acceptance and low background. The large size of the array approximately compensates for the decrease of flux with large distance, and the solid angle subtended is roughly the same for all the long baseline detectors. Monte Carlo calculations show detection and reconstruction efficiencies which are equivalent to a target mass of approximately 10^6 metric tons (half the contained volume) for muons from interactions of 20 GeV neutrinos. For interactions in the contained volume, these Monte Carlo calculations give a 41% trigger efficiency for interactions of ν_e and 51% for ν_μ with the energy distribution expected for a neutrino beam from the Main Injector. A typical trigger rate in the Main Injector beam is about 5 events per hour or 17,000 neutrino triggers in a typical 8 month run with 100 useful hours per week. Triggering and reconstruction are

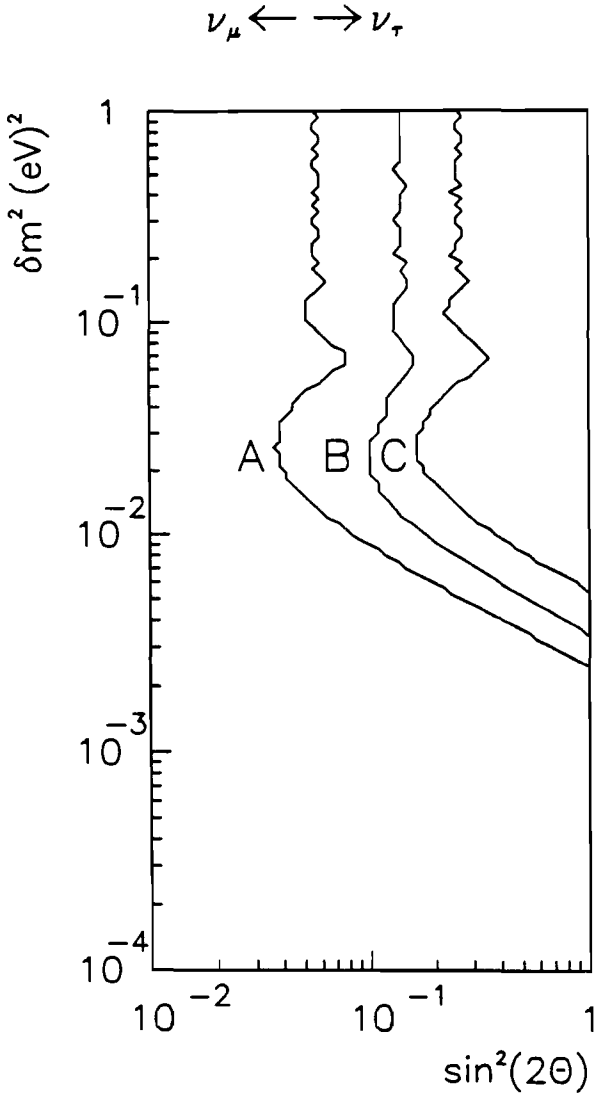

Figure 3.3: Limits on $\nu_\mu \rightarrow \nu_\tau$ Oscillations Attainable by Soudan. Curve A is based on a comparison of event rates in Soudan 2 and a detector at Fermilab, Curve B is based on the neutral current to charged current ratio, and Curve C is based on the $R_{\mu/\nu}$ test

clearly adequate and the detection efficiencies are sufficiently similar that the sum can be used for flux normalization. Techniques for demonstrating a small signal of ν_e in a much larger ν_μ sample are under development through a Monte Carlo.

The array is readily expandable. A modest addition of four additional strings inside this array would enhance the efficiency for low energy events. The cost of such an enhancement is very roughly \$2.5M. If evidence for the existence of neutrino oscillations is found, it would be straightforward to increase the event rate by adding strings of phototubes outside the planned array.

Matter Enhanced $\nu_\mu \rightarrow \nu_e$ Oscillations

The DUMAND array is ten times as far from FNAL as the other proposed long-baseline detectors. This long path of the neutrinos provides room for longer wavelength oscillations of all flavors, and, because it is through the Earth, it also provides sufficient integrated electron density to induce flavor changes to or from ν_e, thus substantially increasing the sensitivity of this detector for small mixing angles with ν_e through the MSW effect. This possibility has been studied [17,19,20] for ν_μ to ν_e oscillations. Similar oscillation enhancements are expected for full three flavor mixings. For example a ν_μ–ν_e mass difference as small as that suggested by the MSW explanation of the solar neutrino deficit ($\approx 10^{-7}$ eV^2) would be very difficult to detect in a laboratory the size of the Earth, but leads one to expect a much larger ν_μ–ν_τ mass difference with a corresponding decrease in oscillation length. Matter mixing of ν_τ and ν_e may then produce a signal which is much easier to detect.

3.5.4 Other possibilities

Physics, costs, or other considerations may dictate that other detectors be used. The proposed Sudbury Solar Neutrino Observatory (SNO) at 930 km is closest to the the present direction of the neutrino beam. It will be a tank of heavy water similar to IMB. MACRO, at Grand Sasso in Italy, is the largest muon detector in the world at present ($864m^2$). It will consist of 12 large supermodules which include proportional chambers, scintillators and streamer tubes. The proposed GRANDE experiment near Little Rock Arkansas ($\sim$ 1000 km) has proposed a long baseline experiment from an extracted beam at the SSC. Grande would consist of phototubes to detect Cerenkov light in several layers of a large bag of clear water.

The possibility should also not be excluded of wanting to do a new experiment at a particular intermediate distance. For example, if there was reason to believe $m_{\nu_\tau} \sim 0.5$ eV/c^2, ($\Delta m^2 \sim .25$eV^2), then the maximum oscillation for the 12 GeV average energy neutrino beam would be at 60 km. A modest sized detector with muon energy measurement

would then be desirable.

Different detectors have differing capabilities which make them attractive or not as a long baseline neutrino detector. For all of the tests which have been discussed in this document for long baseline detectors, the sensitivity to $\sin^2 2\theta$ varies as the square root of the event rate. For a fixed size detector, the event rate goes as the inverse square of the distance to Fermilab (L). Thus the sensitivity to mixing angle goes as $1/L$, down to the mixing angle where systematic effects become important. The sensitivity to Δm^2 goes as $\sqrt{L}$, when the effect of statistics is combined with the second factor in Eq. 3.2.

A second-generation detector, specifically designed for the neutrino spectrum expected from the Main Injector neutrino beam, could also be built. Such a detector could overcome many of the systematic limitations of detectors discussed in this document. It could be designed to (1) provide good ν_μ identification and (2) allow for unambiguous appearance measurements of either ν_e or ν_τ, while still providing an adequate statistical sample.[20]

References

[1] Fermilab Proposal P805, "A proposal for a Long Baseline Oscillation Experiment Using a High Intensity Neutrino Beam from the Fermilab Main Injector to the IMB Water Čerenkov Detector", October 1990.

[2] Fermilab Proposal P822, "A Long Baseline Neutrino Oscillation Experiment Using Soudan 2", March 1991.

[3] Fermilab Letter of Intent P824, "A Neutrino Beam from the Proposed Main Injector to the DUMAND Detector", October 1990.

[4] M. Gell-Mann, P. Raymond, and R. Slansky, 1979 in *Supergravity*, edited by P. Van Nieuwenhuizen and D. Z. Freedman (North-Holland, Amsterdam), p. 315; T. Yanagida, 1979, Proceedings of the Workshop on Unified Theory and Baryon Number of the Universe, Tsukuba, Ibaraki, Japan, unpublished.

[5] T. K. Gaisser, T. Stanev, S. A. Bludman, and H. Lee, Phys. Rev. Lett. **51** (1983) 223; J. L. Osborne, S. S. Said, and A. W. Wolfendale, Proc. Phys. Soc. **86** (1965) 93; A. C. Tam and E. C. M. Young, in: Proc. Eleventh Intern. Conf. on Cosmic rays (Budapest, 1969), Acta Phys. Hungaricae **29**, Supp. 4 (1970) 307; E. C. M. Young, Cosmic Rays at ground level (Adam Hilger. London, (1973), p. 105; K. Mitsue, Y. Minorikawa, and H. Komori, Nuovo Cimento **9 C** (1986) 995; E. V. Bugaev, G. V. Domogatsky, and V.A. Naurnov, Proc. Japan-USA Seminar, Cosmic ray muon and neutrino physics/astrophysics using deep underground/underwater detectors, eds. Y. Ohashi and V. Z. Peterson (Institute for Cosmic Ray Research, University of Tokyo, June 1986) p. 232.

[6] K. S. Hirata, *et al.*, Experimental Study of the Atmospheric Neutrino Flux, Physics Letters **B 205** (1988) 416-420. T. Kajita, talk at Singapore '90.

[7] D. Casper *et al.*, "Measurement of Atmospheric Neutrino Composition with IMB", BU preprint 90-23, (1990), submitted to Phys. Rev. Lett.

[8] Ch. Berger, *et al.*, Phys. Lett. **B245** 305 (1990).

[9] Ch. Berger, *et al.*, Phys. Lett. **B227** 489 (1989).

[10] M. Aglietta, *et al.*, Eurphys. Lett. **8** 611 (1989).

[11] M. Takita, University of Tokyo Ph.D. Thesis (1989).

[12] J. K. Rowley, B. T. Cleveland, and R. Davis, Jr., in Solar Neutrinos and Neutrino Astronomy, eds: M. L. Cherry, W. A. Fowler, and K. Lande, AIP Conf. Proc. No. 126, p. 1, (1985); R. Davis Jr., in Proc. of the Seventh Workshop on Grand Unification, ICOBAN '86, ed: J. Arafune (World Scientific), p. 237 (1987); R. Davis, Jr., in Proc. of the 19th Int'l Conf. on Neutrino Physics and Astrophysics, "Neutrino '88," eds: J. Schneps, *et al.* (World Scientific) p. 518 (1989).

[13] K. S. Hirata, *et al.*, Phys. Rev. Lett. **65** 1297 (1990).

[14] J. N. Bahcall and H. A. Bethe, Phys. Rev. Lett. **65**, 2233 (1990)

[15] S. P, Mikheyev and A. Yu. Smirnov, Sov. Phys. Usp., **30** (1987) 759.

[16] L. Wolfenstein, Phys. Rev. **D 17** (1978) 2369.

[17] T. K. Kuo and J. Pantaleone, Rev. Mod. Phys. **61** (1989) 937-979.

[18] J. Pantaleone, Physics Letters **D 246** (1990) 245-248.

[19] S. J. Parke, Resonant Neutrino Oscillations, Fermilab-Conf-86/131-T (1986).

[20] R. H. Bernstein and S. J. Parke, Terrestrial Long-Baseline Neutrino Oscillation Experiments, Fermilab-Pub-91/59-T, submitted to Phys. Rev. D. S. J. Parke, Terrestrial Long-Baseline Neutrino Oscillation Experiments, FNAL internal note, July 24, 1990; R. Bernstein, Long-Baseline Neutrino Oscillation Experiments at the Fermilab Main Injector, FNAL internal note, June 11, 1990.

[21] S. Matsuno *et al.*, Single Photon Light Detector for Deep Ocean Applications *Nuc. Inst. Meth.* (DUMAND Collaboration), **A 276**, 359 (1989).

[22] J. Babson *et al.*, (DUMAND Collaboration), Phys. Rev., **D 42** (1990) 3613-3620.

4 P-803: $\nu_\mu \leftrightarrow \nu_\tau$ Oscillations

4.1 Physics

The primary goal of Fermilab proposal P-803 is to search for a positive $\nu_\mu \leftrightarrow \nu_\tau$ mixing signal for mixing angles smaller than found in the quark sector. A second oscillation channel, $\nu_e \leftrightarrow \nu_\tau$, will be simultaneously measured at somewhat reduced sensitivity.

The secondary goal, which will be achieved with modest additional effort, is to use the low-energy behavior of neutrino-produced charm and anticharm cross sections to measure both slow rescaling and the Kobayashi-Maskawa matrix element V_{cd} with a precision comparable to unitarity estimates. Finally, precision QCD measurements will be made at low Q^2.

4.1.1 Oscillations

It has been suggested [1] that the tau neutrino, if massive, is the only known particle which could provide sufficient mass to close the universe. A see-saw mechanism [1] which relates masses of neutrinos to quark and/or lepton masses in the same generation indicates that the tau neutrino should be by far the heaviest of known neutrinos. A tau-neutrino mass in the range 10–60 eV/c^2 (sufficient to close the universe) could be generated and still maintain $\nu_e \leftrightarrow \nu_\mu$ oscillations in the 10^{-4} to 10^{-7} eV/c^2 range required by the MSW [2], [3] solution to the solar neutrino problem. Results from SLC and LEP [4] indicate that there are only three generations of light neutrinos, making the tau neutrino an even more attractive dark-matter candidate.

The present world limits for $\nu_\mu \leftrightarrow \nu_\tau$ oscillations are given in Fig. 4.1. These limits are determined by Fermilab experiment E-531 [5] and the CERN CDHSW experiment [6]. Oscillations with a coupling greater than 0.5×10^{-2} have been ruled out for Δm^2 greater than 20 eV/c^2. However, the assumption that lepton mixing angles are comparable to K-

M matrix quark mixing angles leads to the conclusion that $\sin^2 2\alpha$ must be larger than 4×10^{-4}, just ten times smaller than existing limits. P-803 can access 40 times smaller couplings than E531 in the mixing parameter, $\sin^2 2\alpha \leq 1 \times 10^{-4}$, with an estimated background of a fraction of an event, and could clearly establish a signal if one were present at five times this limit. This experiment can also improve the existing limits on $\nu_e \leftrightarrow \nu_\tau$ oscillations by a similar factor, to $\sin^2 2\alpha \leq 5 \times 10^{-3}$, comparable to the old ν_μ limit.

The apparatus is also well-suited to serve as a flux monitor for proposed long-baseline oscillation experiments if one or more of these experiments are approved. P-803 would then share a neutrino beamline with the long-baseline effort(s).

4.1.2 Standard Model

Measurement of $|V_{cd}|$

Because P-803 would have excellent muon identification and topological identification of charm, the same apparatus could simultaneously make definitive measurements both of the "slow rescaling" of charm production and of the Kobayashi-Maskawa matrix element V_{cd} [7]. "Slow rescaling," which refers to the low-energy suppression of the neutrino charm-production cross section due to the massiveness of the charm quark, is parameterized in terms of the charm quark mass m_c, and is one of the main limiting systematic errors in the extraction of $\sin^2 \theta_W$ from deep-inelastic scattering of neutrinos[7]. P-803 would measure m_c to better than ± 0.05 GeV/c^2, as compared to the present determination of 1.5 ± 0.4 GeV/c^2. This would be sufficient to test QCD charm-production models and to eliminate this source of error from the determination of $\sin^2 \theta_W$. Graphs indicating the constraints imposed by 500 topologically-identified charm and 200 similarly identified anti-charm decays are shown in Fig. 4.2.

The present state of measurement of V_{cd} depends on interpretation of systematic errors. If statistical and several systematic errors are summed in quadrature, V_{cd} is now known to 8% from analysis of charm production in deep inelastic scattering [8]. However, if the conservative approach is taken of combining errors linearly, V_{cd} is known only to 13%. Large systematic errors result from the fact that charm production now is inferred through analysis of dimuon data, and thus extraction of this K-M matrix element is model dependent.

On the theoretical side, V_{cd} can be inferred to 1.1% at the one standard deviation level from the unitarity of the K-M matrix [9]. P-803 plans to make a $\pm$ 2.5% direct measurement, approaching a precision where a difference between direct and inferred values could indicate new physics.

Precision QCD measurements at low Q^2

Neutrino scattering traditionally has played a leading role in the extraction both of quark and gluon structure functions, and shows promise of providing precision tests of QCD. Recently, however, controversies have arisen because the size of contributions from "nonperturbative" effects is not calculable and could be large [10,11]. Since most nonperturbative effects are worse at low energies and smaller Q^2, one way to estimate their size experimentally is to measure the full gamut of structure functions using intense low-energy neutrino beams from the Main Injector.

In the initial emulsion run P-803 will acquire the same number of ν_μ and $\bar{\nu}_\mu$ charged current interactions as obtained by Fermilab experiments E744 and E770 (1.4×10^6 and 0.3×10^6, respectively). Using a low-Z aluminum target instead of emulsion, twice this number of events could be obtained in another similar running period.

The spectrometer is particularly well set up to measure both hadronic energy and energy flow, and will measure the momentum of most muons to better than 6%. The ability to separate neutral current from charged current interactions is better than for any previous neutrino detector. Further, methods applied for relative normalization of neutrino to antineutrino data in the more conventional neutrino experiments [12] also could be applied here. Analysis would be all-electronic, not depending in any way on results from scanning of emulsion. Though the main thrust of this experiment has been to measure oscillations and V_{cd}, the ability to study conventional structure functions and QCD processes at low energies and Q^2 will receive increasing attention in the future.

4.2 Experimental Method

4.2.1 Strategy

The proposed experiment is intended to increase the sensitivity for detecting $\nu_\mu \leftrightarrow \nu_\tau$ oscillations by a factor of 40 over E-531. P-803, shown in Fig. 4.3 is a hybrid emulsion experiment in which τ decay candidates are observed in an active emulsion target. An electronic spectrometer selects and locates the events to be scanned in the emulsion, and provides momentum, energy and particle identification information for reconstruction of each event.

The large increase in sensitivity over E-531 comes mainly from an eightfold increase in emulsion target mass and an eighteen-fold increase (in one running period) of protons on target provided by the rapid-cycling 120 GeV beam from the new Main Injector. The yield of neutrinos per proton has also been significantly increased by a complete neutrino beam redesign. Target and beam parameters for E-531 and P-803 are compared in Table 4.1. The

Item	E-531	P-803
Volume of emulsion	23 liters	200 liters
Mass of emulsion	0.10 ton	0.84 ton
Area of emulsion	0.9 m×0.7 m	1.8 m×1.8 m
Thickness of emulsion	5.0 cm	7.5 cm
Primary proton energy	400 GeV	120 GeV
Protons per pulse	1.3×10^{13}	4×10^{13}
Cycle time	8 sec	2.0 sec
Number of pulses†	1×10^{6}	6×10^{6}
Total protons on target	1.3×10^{19}	2.4×10^{20}
Average CC interaction energy	30 GeV	16 GeV
CC interactions in target (all E_ν)	6×10^{3}	1.5×10^{6}
NC interactions in target (all E_ν)	0.2×10^{3}	4.4×10^{5}

† Assumes one 8-month run at 100 useful hours/week.

Table 4.1: Comparison of Target and Beam Parameters for E-531 and P-803.

P-803 yields in this proposal are based on one 8-month running period, though several runs could be envisaged.

Not all of the increase in number of interactions is reflected in an increase in sensitivity over E531, for several reasons. First, the ν_τ interaction cross section is suppressed at low energy by kinematic and helicity effects (see Fig. 4.4), and tau leptons are harder to detect at the lower energies of P803 (see Fig. 4.5). Also, because of the large number of interactions, it will not be possible to scan for every neutrino interaction as in E-531. Selecting events corresponding to the present scan load capability of 30,000 events per year will incur losses from spectrometer cuts. Finally, no τ decay candidates were observed in E-531, while the estimated expected background [13] was 1 event. Using the same acceptance criteria for candidates in P-803 would result in an estimated background of > 100 events. A major reduction in background results from limiting the search to single-prong decay modes of τ^- (see Table 4.2 below), in events in which there is no muon or electron from the primary vertex.

Table 4.2: Single-Prong Decay Modes of τ^-

Label	Decay Mode	Branching Ratio
1	$\mu^- \nu_\tau \overline{\nu_\mu}$	17.8%
2	$e^- \nu_\tau \overline{\nu_e}$	17.5%
3	$\pi^- \nu_\tau$, $K^- \nu_\tau$	11.5%
4	$\rho^- \nu_\tau$	22.6%
5	$\pi^- \nu_\tau$ multi-γ	16.2%
	Total one-prongs	85.6%

4.3 Summary of Procedure

The experimental procedure is as follows: triggered events recorded on tape are reconstructed in the spectrometer, and a subset is selected for emulsion scanning. For the beam flux of Table 4.1, it is estimated that selection criteria will yield 60,000 neutral-current candidates, 15,000 charged-current candidates in which the muon escapes identification, and 6,000 candidates with an identified muon, for a total of 81,000 scan events. Additional scanning of a smaller number of neutrino and antineutrino charged-current events will be required both to investigate backgrounds and to study "Standard Model" physics. The scan load for this part of the effort is less well determined, but is bounded in the range 10,000 to 25,000 events.

The primary neutrino interaction vertex is found by linking one track (the "leading track") from the spectrometer tracking chambers to the downstream face of the emulsion, and following it back to the primary. The features of a tau decay candidate in the emulsion are indicated schematically in Fig. 4.6. Because of the relatively large mass of the τ, it is produced at relatively small laboratory angles: 98% of real τ's will be at angles less than 15°. One-prong decay candidates are located by following down all primary tracks within a cone of 15° from the beam direction for a distance of 2.5 mm, searching for a kink of more than 10 mrad. (Note that $c\tau$ for τ's is 0.091 mm, and γ's are of the order of 5, so that 2.5 mm is more than adequate.)

For events in which a kink is found, the kink secondary must be followed all the way to the exit of the emulsion (followdown) and linked to the spectrometer so that its charge and momentum can be determined. Positively-charged kinks are rejected at this stage, as are those which are too soft (momentum $p < 1.0$ GeV/c) or have insufficient transverse momentum ($P_T < 0.30$ GeV/c) relative to the candidate τ direction. For events meeting these criteria, it must be established that none of the tracks from the primary vertex are

identified as muons (ν_μ CC event) or electrons (ν_e CC event). Many such tracks can be matched between the emulsion and the spectrometer without followdown, but ambiguous matches must followed out. Finally, the τ decay modes consistent with the event must be identified, and the event must pass the particle identification and kinematic cuts for at least one of these modes.

Backgrounds in order of increasing severity are short decays of charged kaons and hyperons, interactions of ν_τ coming from the beam dump, one-prong decays of anticharm produced by the $\bar{\nu}_\mu$ contamination of the beam, and one-prong interactions with no indication of nuclear breakup ("white star kinks"). These sources of background are estimated to contribute 0.01, 0.07, 0.10, and 0.30 events, respectively, for the data sample specified in Table 4.1.

4.3.1 Seeing a Positive Signal

Most oscillation experiments in the past have been more efficient at setting limits than seeing positive indications of oscillation. Because emulsion techniques can accurately measure short decays, P-803 can convincingly demonstrate the existence of tau leptons coming from charged-current interactions of tau neutrinos.

First, charm and tau decays have a similar topology; observing charm proves that it is possible to find tau lepton decays. One and three prong topologies can be measured for charged-current production of charm and anti-charm, and efficiencies can be inferred by comparing measured to known branching ratios.

Secondly, tau lepton kinks have quite a different distribution in P_T and decay length than "white star" interactions, which are the primary source of background. Fig. 4.7 shows distributions in P_T on the vertical axis versus decay length on the horizontal axis for Monte Carlos of real tau decays in the upper scatterplot and "white star" kinks in the lower plot. Note that P_T is measured with respect to the parent direction, not the beam direction. Without the precision of emulsion both plots would be smeared vertically, drastically increasing interaction background.

Finally, if the signal is 5 times larger than the 90% C. L. limits, cuts can be loosened and approximately 10 two-body tau decays can be observed, where one body is measured and the other is the missing neutrino. Two-body decays have a Jacobian mass peak which will permit the extraction of average masses and lifetimes with a systematic uncertainty of less than 10%.

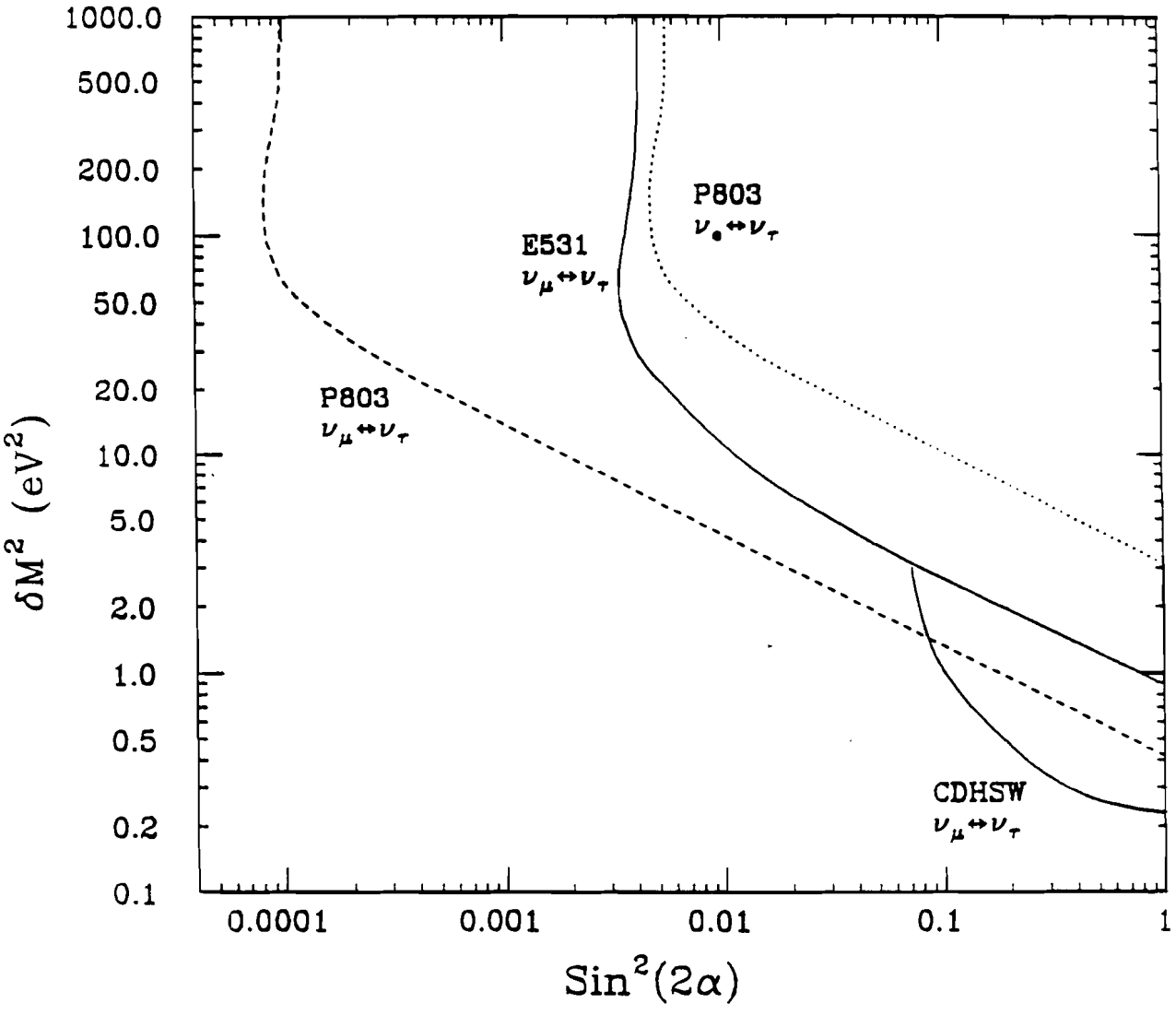

Figure 4.1: Δm^2 *vs.* $\sin^2 2\alpha$ plane showing the previous limits for $\nu_\mu \rightarrow \nu_\tau$ oscillations (solid curves), and the improved limits on $\nu_e \rightarrow \nu_\tau$ (dotted curves) which can be obtained from P–803. The regions to the right of the appropriate curve are excluded at the 90% CL.

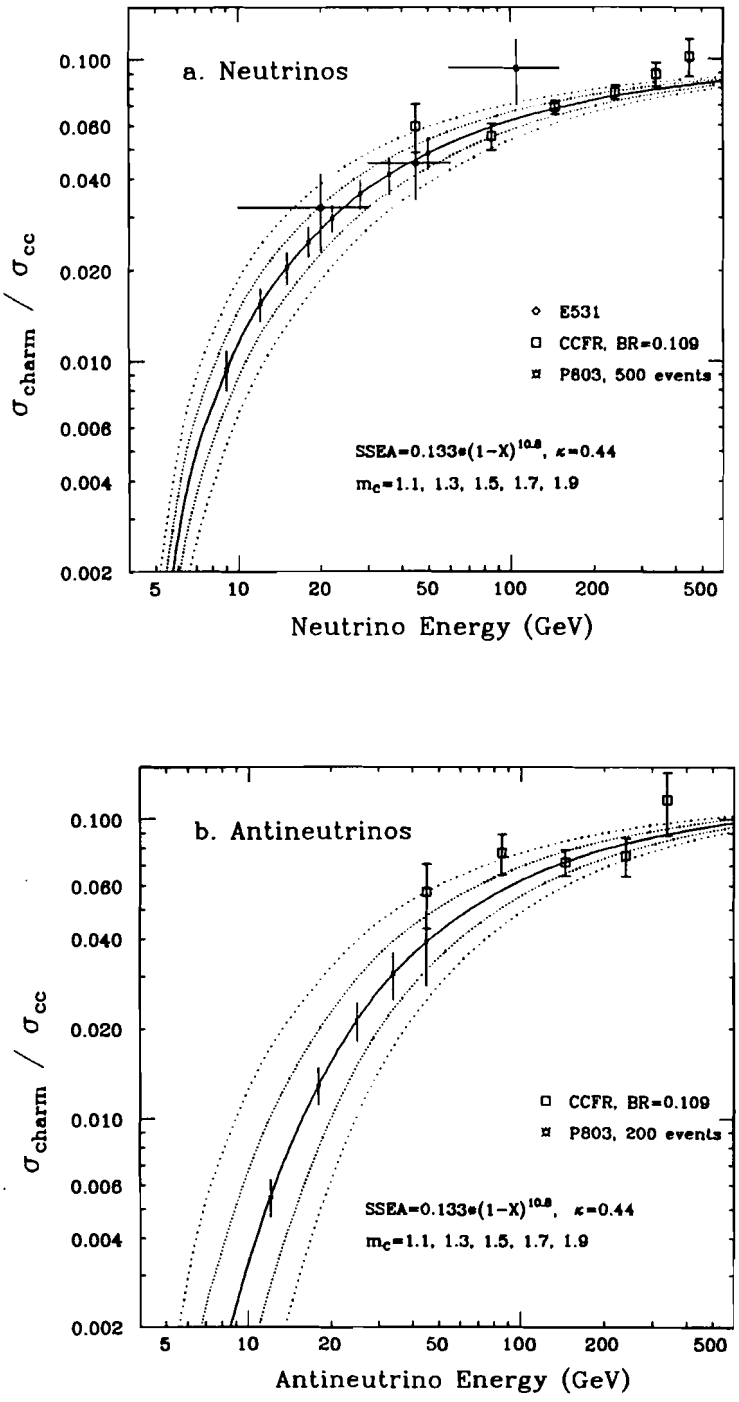

Figure 4.2: The ratio of charm production to charged-current interactions for (a) neutrino and (b) antineutrino interactions. The impact of 500 neutrino charm events and 200 anti-charm events from P–803 is shown.

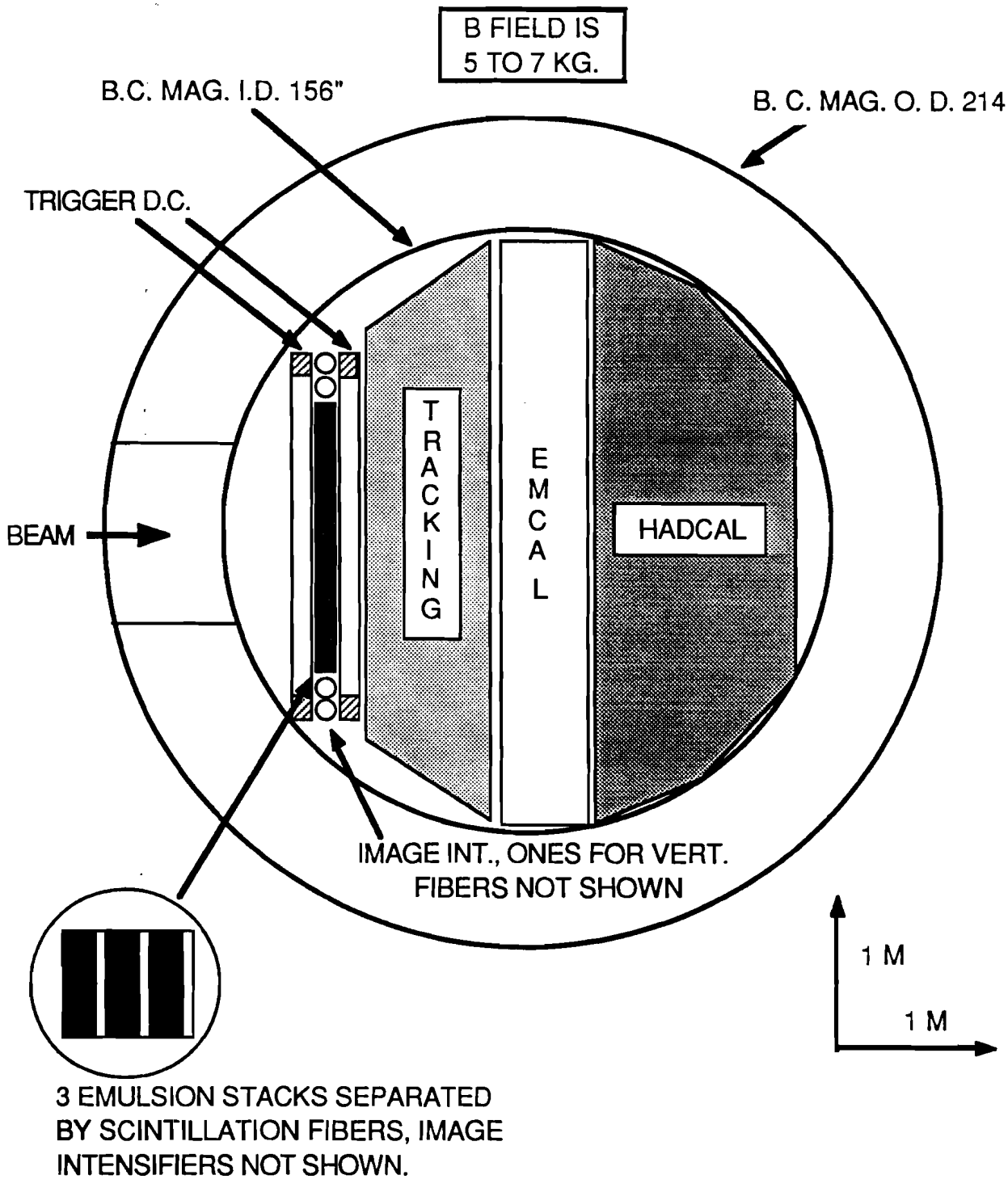

Figure 4.3: Plan View of P-803.

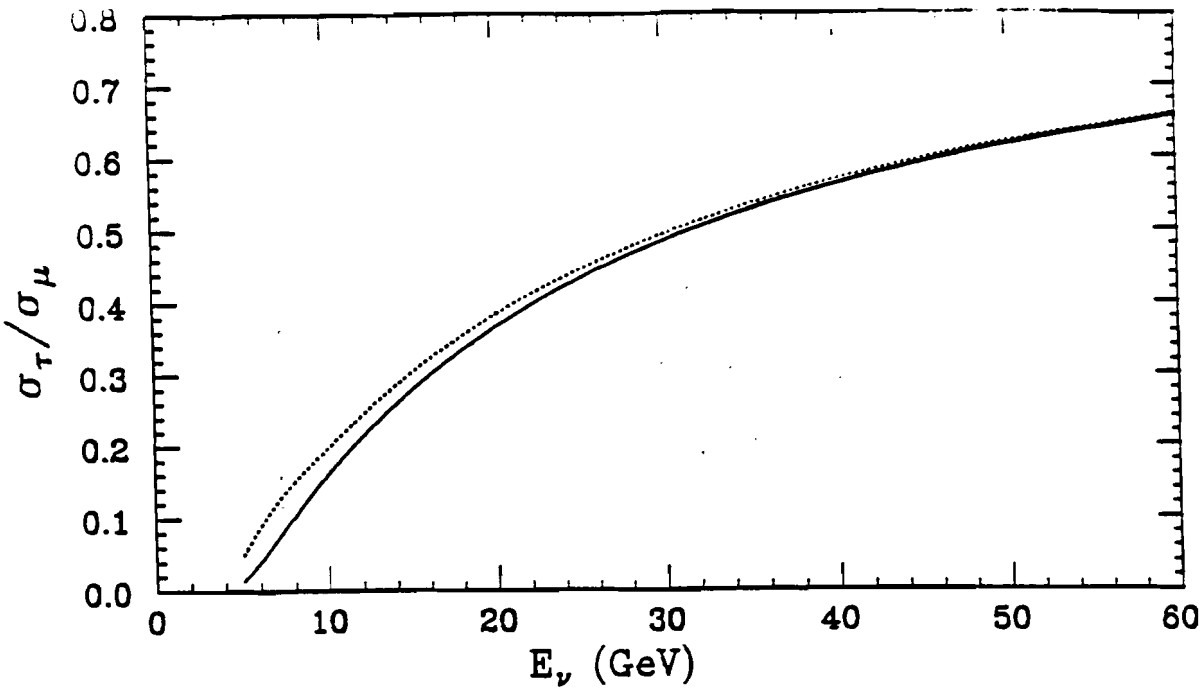

Figure 4.4: The ratio of ν_μ/ν_τ cross-sections displayed as a function of incident neutrino energy. The solid curve shows the deep inelastic and parton model contributions, while the dotted curve includes quasi-elastic and Δ^{++} contributions to both ν_μ and ν_τ cross-sections.

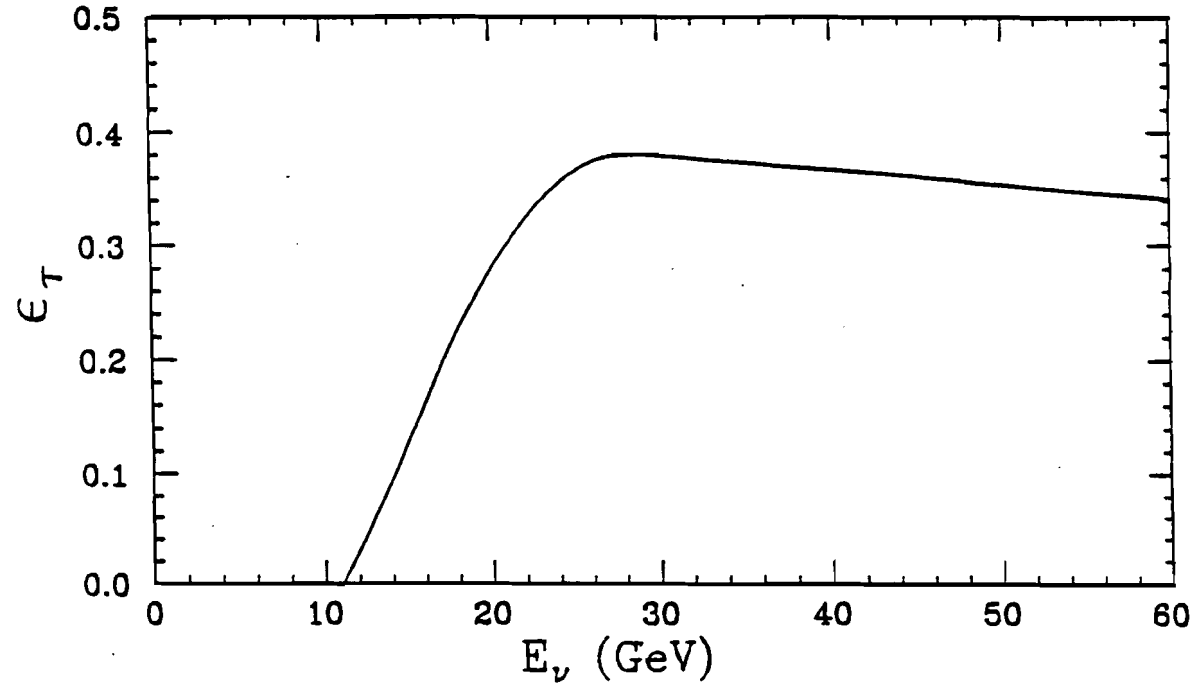

Figure 4.5: Neutrino energy dependence of τ detection efficiency ϵ after event selection cuts have been applied. Energy-independent efficiency contributions have been suppressed.

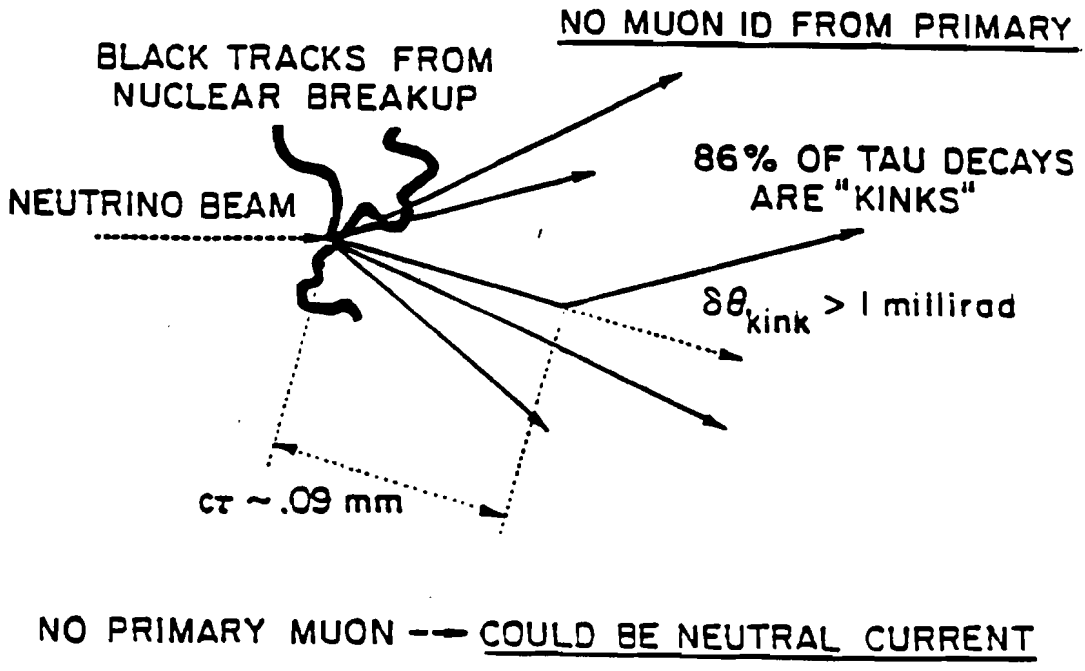

Figure 4.6: Schematic of τ decay Candidate in Emulsion. Note the heavily ionizing tracks from nuclear breakup, the absence of an identified muon from the interaction vertex, and a short decay-length "kink" with a large P_T.

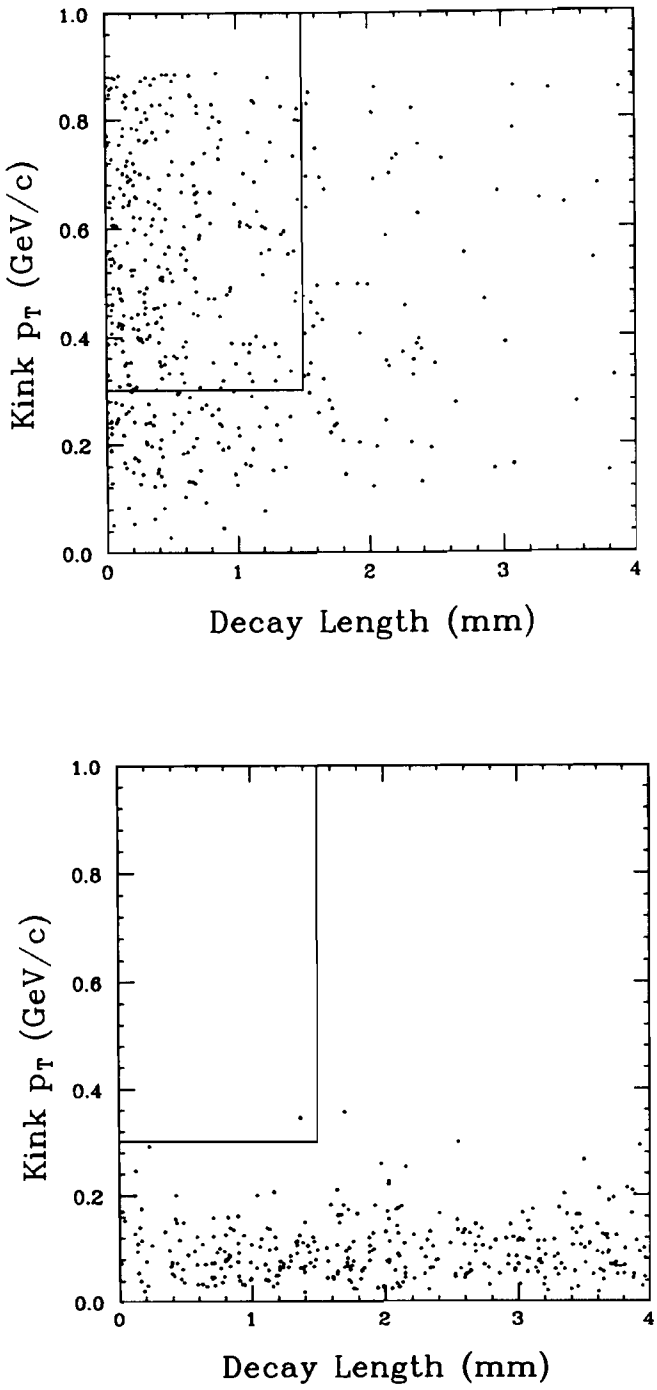

Figure 4.7: P_T Distribution for two-body τ decay. The plots are simulations of the kink in P_T in GeV/c relative to the parent direction (vertical axis) vs. decay length in mm (horizontal axis). The upper scatterplot is for τ events passing the scan cuts, while the lower one (arbitrarily normalized) is for whitestar kinks passing the same cuts. The two distributions are very dissimilar. Events accepted by the kink cuts are inside the boxes.

References

[1] See, e.g., H. Harari, Phys. Lett. B216, 413 (1989).

[2] L. Wolfenstein, Phys. Rev. D17, 2369 (1978).

[3] S. P. Mikheyev and A. Yu. Smirnov, Sov. J. Nucl. Phys. 42, 913 (1985).

[4] G. S. Abrams, *et al.*, Phys. Rev. Lett. **63**, 2173 (1989); LEP results in press.

[5] N. Ushida, *et al.*, Phys. Rev. Lett. **57**, 2897 (1986).

[6] F. Dydak, *et al.*, Phys. Lett. **134B**, 281 (1984).

[7] The possibility of making these measurements was suggested to the proponents of P-803 by R. Brock.

[8] C. Foudas, *et al.*, Phys. Rev. Lett. **64**, 1207 (1990); M. Shaevitz, Lectures at the 1989 SLAC Summer Institute.

[9] J. Cudell, F Halzen and S. Pakvasa, Phys. Rev. **40D**, 1562 (1989).

[10] G. Altarelli, "Tests of QCD", Ann. Rev. Nucl. Part. **39**, 366 (1989).

[11] S.R. Mishra and F. Sciulli, "Deep Inelastic Lepton-Nucleon Scattering", Ann. Rev. Nucl. Part., **39**, 259 (1989).

[12] S. R. Mishra, *et al.*, "Improved Measurement of Inverse Muon Decay at the Fermilab Tevatron", Nevis Preprint 1424 (1990).

[13] A. Gauthier, Ph.D. thesis, The Ohio State University, (1987).

[14] N. Ushida, *et al.*, Nuc. Instr. and Meth. **224**, 50 (1984).

[15] K. Kodama, *et al.*, Nuc. Instr. and Meth. **A289**, 146 (1990).

Part II

Beams

5 Tevatron Beams

5.1 Quadrupole Triplet and Sign-Selected Quadrupole Triplet

The physics goals of P-815 require two runs with two different beams. The first, a Sign-Selected Quadrupole Triplet, is described below. The second is the same Quadrupole Triplet employed for E-744/E-770. Both of these beams will run in the present NCenter line. The modifications to NCenter itself are small; we have already run the Quadrupole Triplet beam and the changes for the Sign-Selected Beam are not major. If P-815 Phase I is approved for a run before the MI turn-on, the Sign-Selected Beam will have already been constructed and operated. Changing between the two configurations will not be difficult but will require waiting until the end of the run since the area will be radioactive and the same magnets will be used for each.

5.1.1 Sign-Selected Quadrupole Triplet Beam: Characteristics and Design

The Sign-Selected Quadrupole Triplet (SSQT) Beam designed for P-815 must achieve three goals:

- Separation of ν from $\bar{\nu}$. This is necessary for the *separate* measurements of $\sin^2\theta_W$ and ρ where $\sin^2\theta_W$ is measured from the neutrino data and ρ from the antineutrino sample.
- Elimination of ν_e from K_L since they provide a difficult-to-measure background for neutral currents events.
- The loss in rate over a pure Quadrupole Triplet must be less than that of a dichromatic beam; we have designed a system with a factor of three loss, compared to a dichromatic

beam which has typically one-tenth the flux of the Quadrupole Triplet.

Fig. 5.1 shows the layout of the proposed beam. The primary proton beam stops in the second beam dump for neutrino running. To switch to antineutrino mode one reverses all the magnet currents (while leaving the primary proton targeting unaltered) and the protons then stop in the first dump. A small adjustment to the field of the final dipole will be made to center the lower energy negatives on the detector. Table 5.1 gives a list of locations, currents, and apertures for the elements in standard Transport units; z-locations are given along NCenter.

Table 5.1: Beam-Sheet for Sign-Selected Quadrupole Triplet.

Element	Type	z-location(ft)	length(ft)	B(kg/in)
1	Target	3175.00	1.0	0.0
2	Modified B1	3183.25	10.0	-18.
3	$\bar{\nu}$ Dump	3196.0	12.0	0.0
4	4Q120	3209.50	10.0	-3.634
5	ν Dump	3226.00	12.0	0.
6	4Q120	3239.50	10.0	3.282
7	4Q120	3252.20	10.0	3.282
8	4Q120	3282.20	10.0	-3.634
9	4–5–72 Dipole	3293.20	6.0	-9.561

The currents and locations of magnets are as given in a coordinate system with 300 GeV/c secondaries focused along the x-axis although the line will actually be at an angle to the current NCenter line. This particular geometry will permit us to maintain the NWest beam, used as the D0 test line. A schematic is shown below. The indicated magnets will always be off for fast-spill; during slow spill, they will be ramped on when the protons are targeted for ν data-taking, and left off for $\bar{\nu}$. All magnets shown exist, except for two magnets: the first is immediately downstream of the target and the second is the final dipole.

We have checked the calculated rates against the QT fluxes from E-744/E-770 in three different ways: (1) from the trigger rate, (2) from the normalization on the E-744/E-770 charged-current sample, and (3) from the normalization of the neutral current sample (with 1 meter radius and 20 GeV E_H cuts). All three methods indicate that the program predicts the correct number of events to within 20% for the QT beam; we are therefore confident that these statistical estimates are accurate to that precision and have scaled down the estimates from the code so that they agree with the lowest rate derived from the data.

The large bends make the K_L and wrong-sign backgrounds negligible, but the bends also cause some loss of flux, especially at the highest energies. The following series of Figures

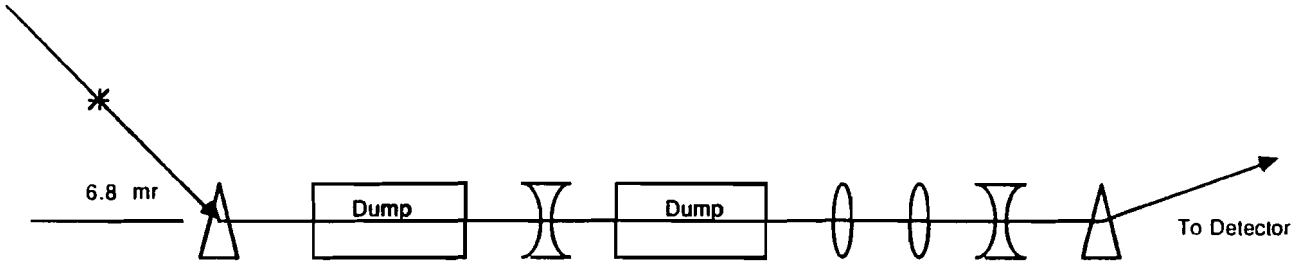

Figure 5.1: Internal Layout of Sign-Selected Quadrupole Triplet.

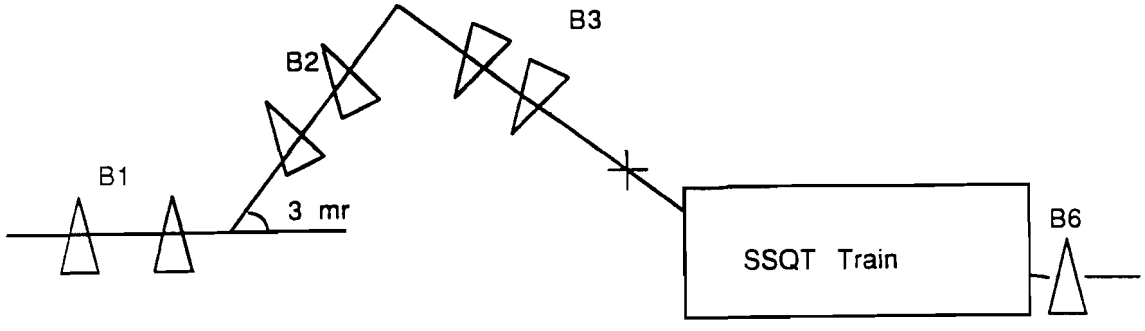

Figure 5.2: Sign-Selected Quadrupole Triplet and NWest Beam

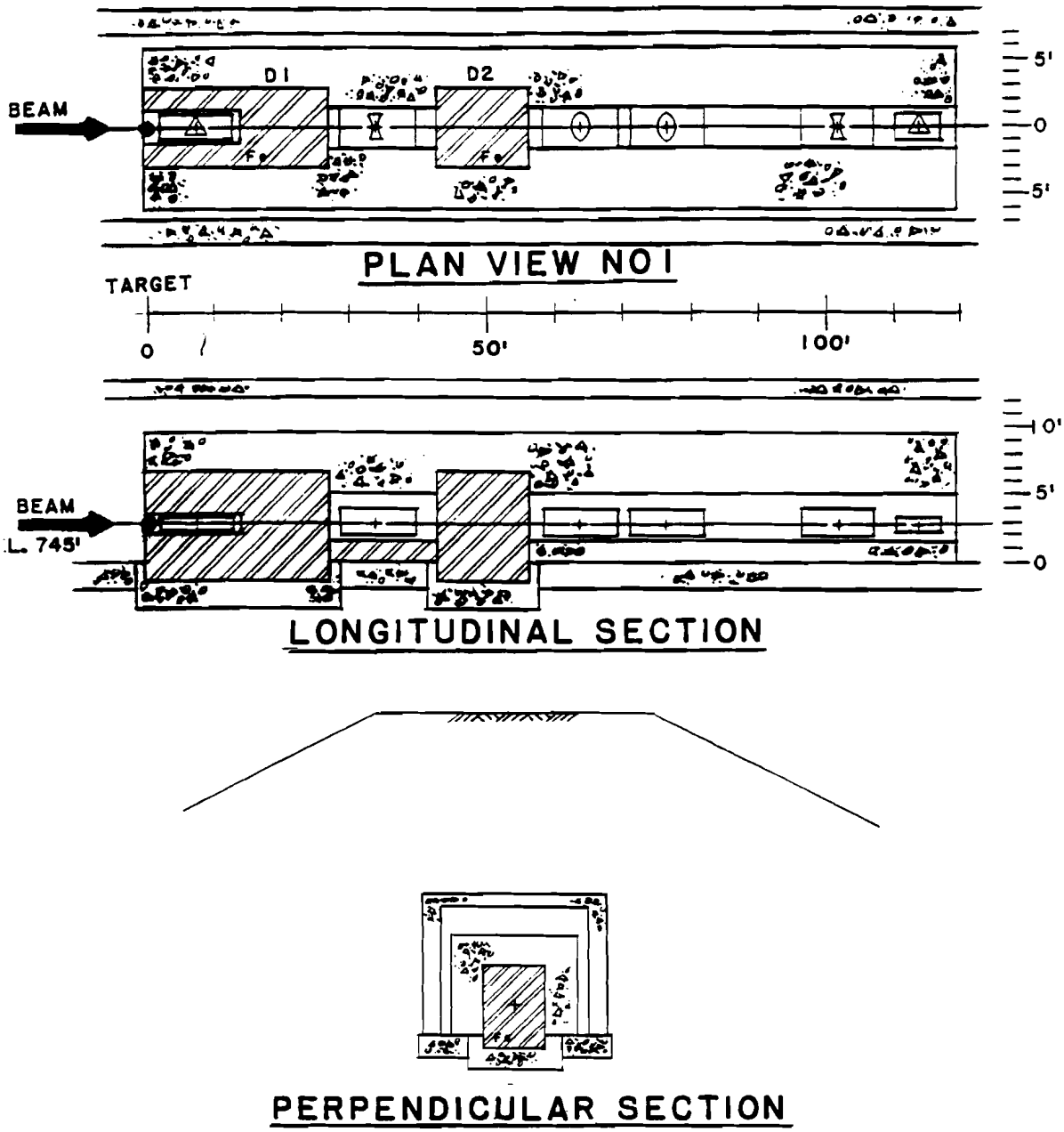

Figure 5.3: Layout of SSQT in N01 Hall.

illustrate the nature of the SSQT. All plots are normalized to exposures of 10^{18} protons on target within a 50 in radius. Fig. 5.4 shows the ν_μ fluxes from the QT and SSQT; the antineutrino spectra are softer, with $< E_\nu > \approx 100$ GeV, and are a factor of three lower in rate, but are otherwise similar.

The wrong-sign background is shown below and is under 0.1%, making the beam more than clean enough to allow separate measurements of ρ and $\sin^2\theta_W$. Furthermore, the remaining samples have mean energies of ≈ 30 GeV, and hence can be cut from the data, as shown in Fig. 5.5.

Fig. 5.6 shows the distribution of the remaining ν_e events from $K^\pm$ and K_L decay for neutrino data (once again, the antineutrino plot is similar). We see the overall level of K_L is down by a factor of five and once again, the spectrum is soft ($< E_\nu >= 28$ GeV) and can be cut if necessary.

5.1.2 Quadrupole Triplet Beam

The Quadrupole Triplet has the advantages of high flux and it is the highest energy neutrino beam ever operated. P-815 requires the high-energy for its structure function measurements. The highest-energy events are also useful for searches for rare processes, where certain backgrounds become small.

Restoring a Quadrupole Triplet line is accomplished in three steps: (1) first the train is brought back to its old location, (2) the upstream dipoles are replaced, and (3) within the train, the two dipoles are turned off and the protons are targeted at 0 mr. The protons then dump after the end of the decay pipe in the current location. Fig. 5.7 shows the rates for ν, $\bar{\nu}$, and total ν_e from K_L rates for the Quadrupole Triplet of E-744/E-770; a Beam-Sheet is given in Table 5.2.

Table 5.2: Beam-Sheet for Quadrupole Triplet

Element	Type	z-location	length	field
1	Target	3040.25	1.0	0.0
2	Collimator	3049.25	12.0	0.0
3	4Q120	3062.25	10.0	4.914
4	4Q120	3074.25	10.0	4.914
5	4Q120	3101.25	10.0	-4.000
6	4Q120	3113.25	10.0	-4.000
7	4Q120	3149.25	10.0	3.114
8	4Q120	3161.25	10.0	3.114
9	4Q120	3188.25	10.0	-2.772

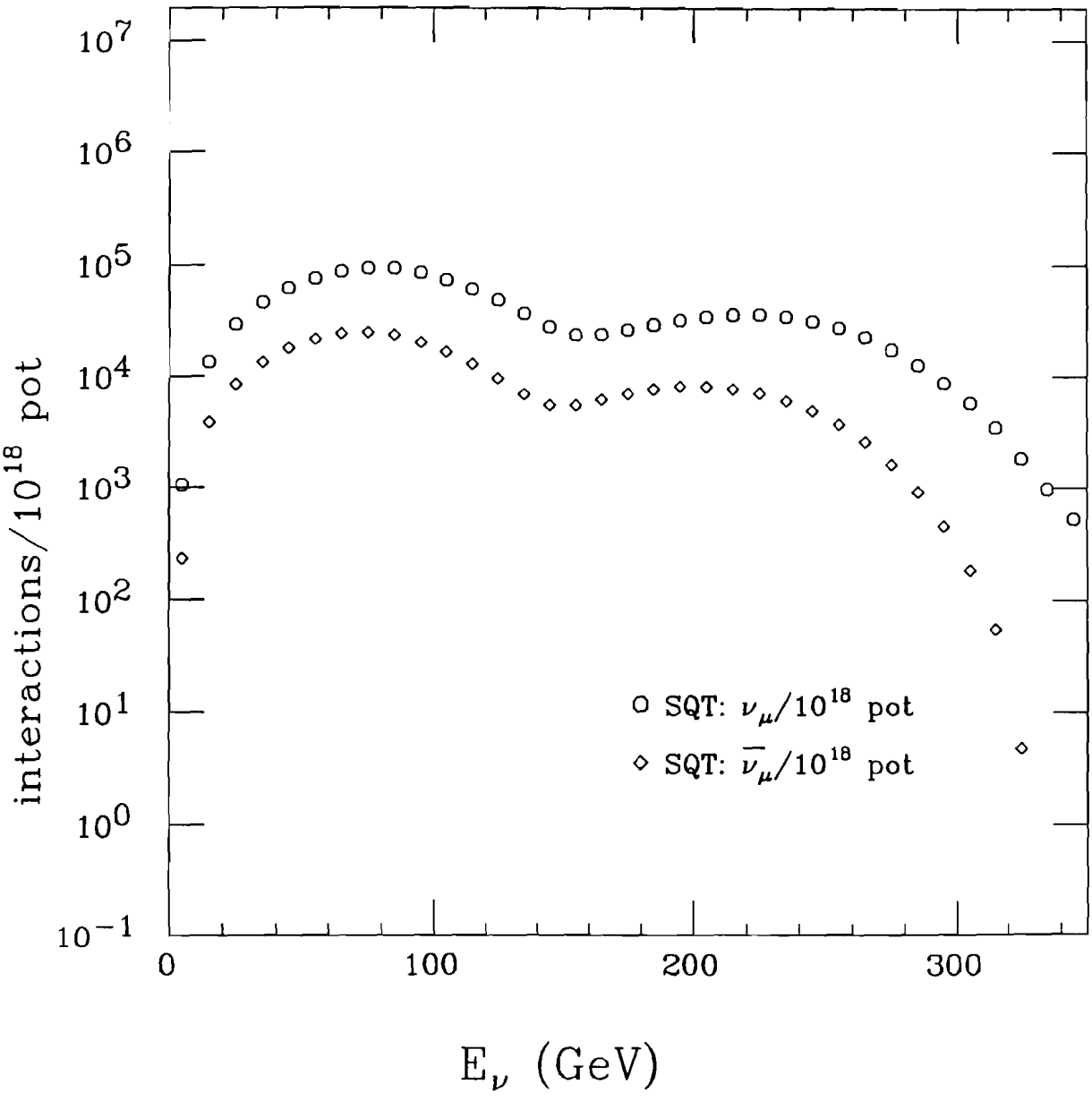

Figure 5.4: Sign-Selected Quadrupole Triplet Fluxes. Neutrino and Antineutrino Data are taken in different runs, and are normalized here to 10^{18} protons on target.

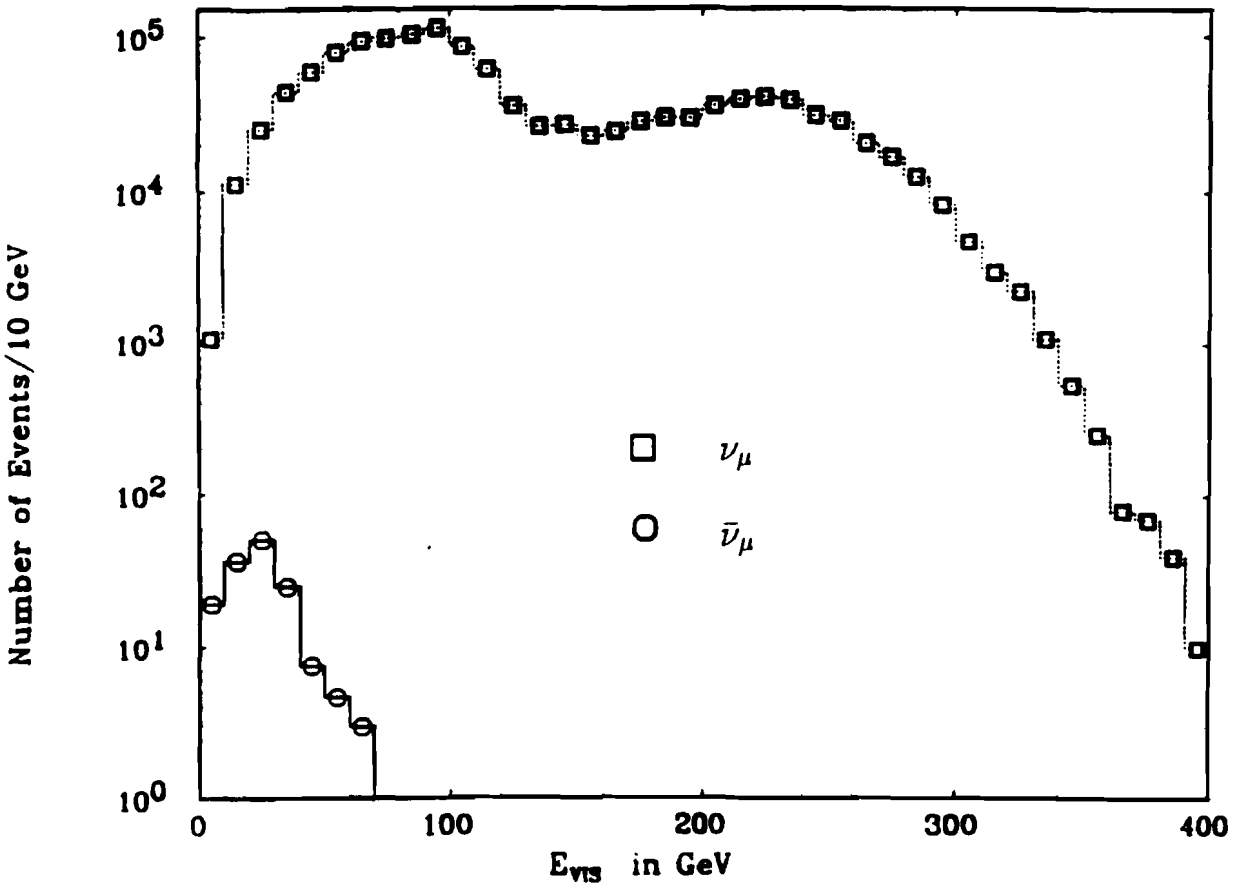

Figure 5.5: Wrong-sign Background in Sign-Selected Quadrupole Triplet

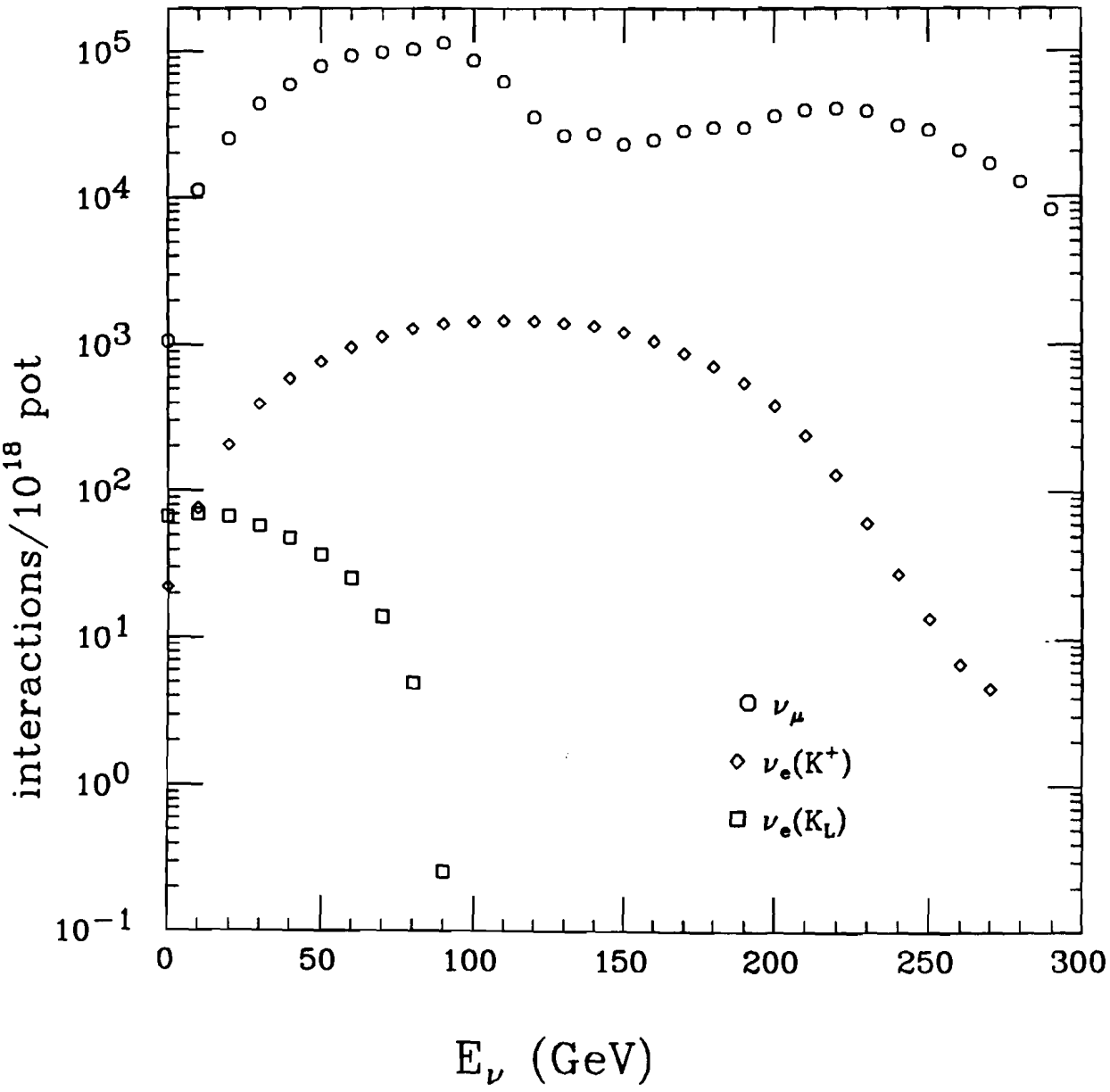

Figure 5.6: ν_e Backgrounds in the Sign-Selected Quadrupole Triplet.

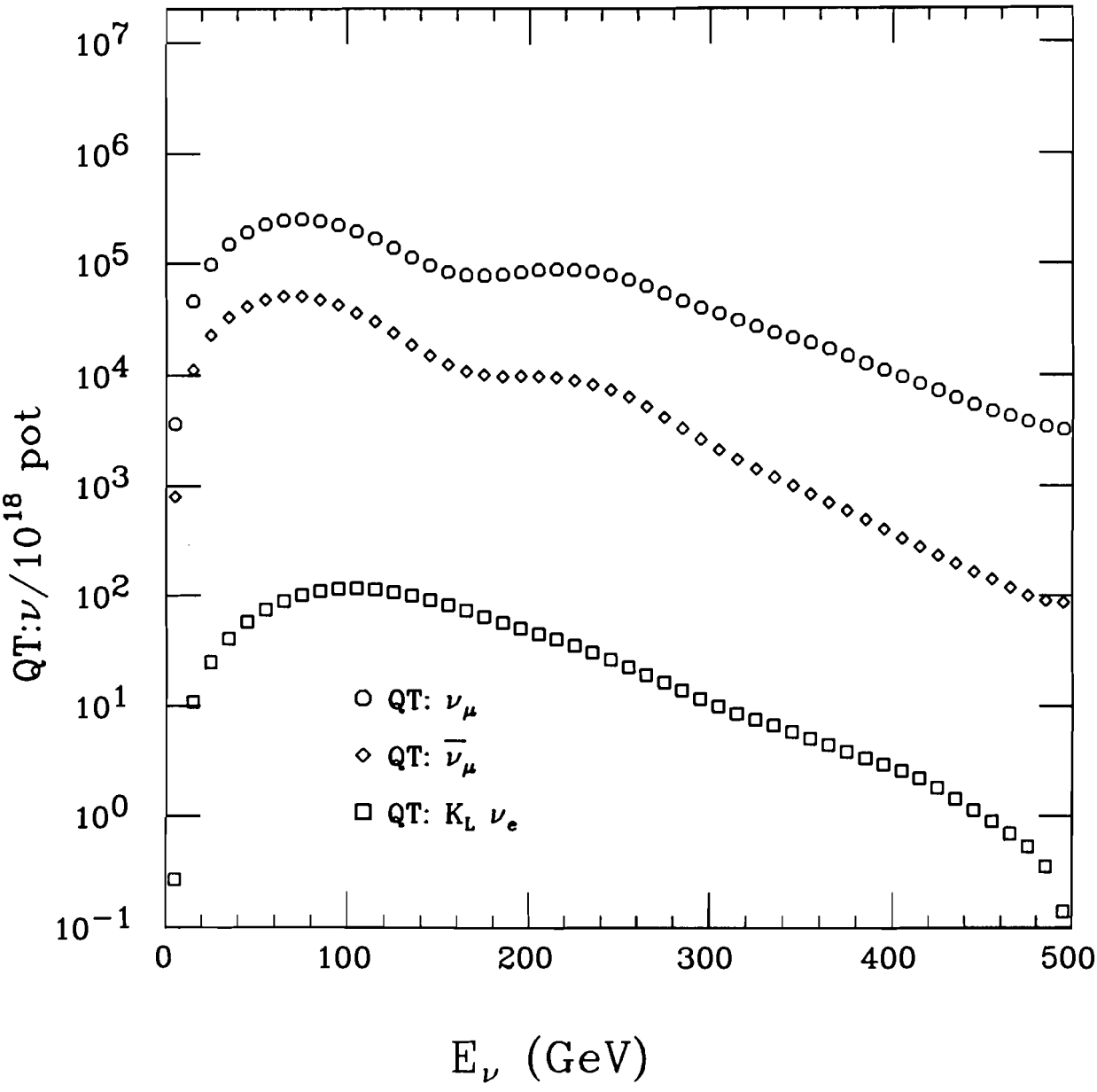

Figure 5.7: Quadrupole Triplet Fluxes.

6 120 GeV Beams: Transport, Target, and Horn

6.1 Overview

The beam line for production of neutrinos by 120 GeV protons from the Main Injector has been designed taking into consideration the following objectives:

- Full utilization of the Main Injector potentials in producing 120 GeV proton beam with a flux of up to 3×10^{13} protons with a cycle time of 1.9 sec and a spill time of 1 msec [7]. To provide a "safety margin", we have *designed* the system to withstand heating and stresses from a 1.5 sec cycle time and 4×10^{13} protons.
- Maximizing the neutrino flux by optimizing the output of secondary pions and kaons from the target and maximizing their focusing into the decay region.
- Minimizing the cost of the beam line by shortening the most expensive element of the beam line, the decay tunnel, to the extend which still secures the reach of the physics objectives. These savings are possible due to the more cost efficient improvements in the design of the target - focusing systems.
- Satisfying Radiation Safety and Groundwater Activation Requirements.

The proposed neutrino beam line is a simple wide-band beam required to perform short or long baseline neutrino oscillation experiments. It consists of the following elements, described in some detail in the forthcoming sections of this document:

1. The extraction of the proton beam from the Main Injector is coupled to the Main Injector beam abort system in the straight section MI-50.[12] Such a solution provides

substantial savings of the cost of the extraction system and of civil construction of the front part of the beam line.

2. The proton beam transport system to the target area is designed to fulfill two basic requirements: to efficiently transport the beam in the direction of the detector (for concreteness we have chosen the IMB detector) with a tolerance of 0.2 mrad, and to provide focusing of the beam to a size matching the strong requirements of the proposed production target.

3. The production target is designed to assure that it will survive the full intensity of the proton beam from the Main Injector at the regular spill time of 1 msec, as well as during the emergency abort at 10 μsec. The design also provides the means of cooling the target even at the fastest cycle time of 1.9 sec without destruction of the azimuthal symmetry of particles produced in the target. Finally, the construction of the target assures the maximum output of particles which, when properly focused, can decay to neutrinos in the direction of the dedicated detectors.

4. A wide-band double horn focusing system has been designed. The first horn has a shape of the inner conductor like a "conical vee" while a second one a shape of a cone. The inside diameters of the inner conductors are made relatively large so the primary proton beam is unlikely to strike and possibly melt them. The shapes, current and spacing between the horns have been optimized to focus particles with transverse momenta up to $p_\perp = 0.9$ GeV/c into the decay tunnel. The wall thicknesses of inner conductors are chosen so they can withstand the axial component of the magnetic pressure and still provide minimum absorbtion of particles which have to pass through them. The operating current for the horns is expected to be 170 kA, but their mechanical properties are designed for currents up to 200 kA.

5. The decay region where secondary pions and kaons can decay into neutrinos consists of 30 m of space filled with air between the target and the end of the horn system, 45 m of space filled with helium gas between the last horn and the beginning of the decay pipe, and 245 m of evacuated decay pipe. The total length of the decay region is 320 meters. Almost no flux can be gained by a short-baseline experiment as this distance increases, because of the smaller solid angle subtended by the detector. The diameter of the decay pipe is determined primarily by cost; the cost per unit length of a 2 meter diameter pipe is more than an order-of-magnitude higher than that of a 1.5 meter pipe.

6. A beam dump is located at the end of the decay pipe. Its role is to absorb all hadrons which reached this point of the beam line and protect soil against undesirable radioactive contamination. Since the primary and secondary beams at such distances are well-dispersed, a standard solution with water cooled cores surrounded by iron can be applied for the beam dump design.

Preliminary results of calculations of the beam neutrino output: the neutrino beam composition, fluxes and energy spectra of various neutrino flavors, are discussed in Sec. 6.5 and 6.7.

The measures provided to shield ground water against radiation produced along the beam line are described in Sec. 7.2.

6.2 Location and Impact on Design

Before presenting the details of the 120 GeV line, we explain the framework for our design. One of the most significant problems in oscillation experiments is the control of systematic errors associated with the beam. Many experiments therefore use two detectors at different distances from the source; the first measures the flux and the second looks for a change, signalling an oscillation. We can use P–803 and one of the long-baseline experiments in this way provided they are along the same line. It is also clear that since the long- and short-baseline experiments share many features, it will result in a considerable savings to associate the two along a common beamline. We have chosen to concentrate on P-803 and P-805 along a common line in a new area. Arranging P-803 and P-822 as a unit would require targeting to a different area; the proton transport section of this Report would be different, but other designs would be essentially unchanged.

We list in Table 6.1 the relevant features of the different experiments that are being considered. The layout of potential beamlines on the Fermilab site is shown in Fig. 6.1.

Table 6.1: Possible Oscillation Experiments

	Proposal	Location	Down Bend
P-803	Short Baseline	Fermilab site	level
P-805	IMB	Cleveland, OH (41.76N, 81.29W)	44.8 mrad
P-822	Soudan II	near Hibbing, Minnesota	63.9 mrad
P-824	DUMAND	30 km west of Keahole Pt., HI	506. mrad

We have mentioned that P-803 could function as the "front-detector" for a long-baseline experiment. This is true for P-805(IMB) or P-822(Soudan) but *not* for P-824(DUMAND). The 506 mr. bend would put the P-803 detector 260 m underground making the tandem operation of these two lines impractical.

If P-803 were to function as the sole neutrino oscillation experiment, there are two options:

1. P-803 would be placed in a new area, with the beam extracted directly from the Main

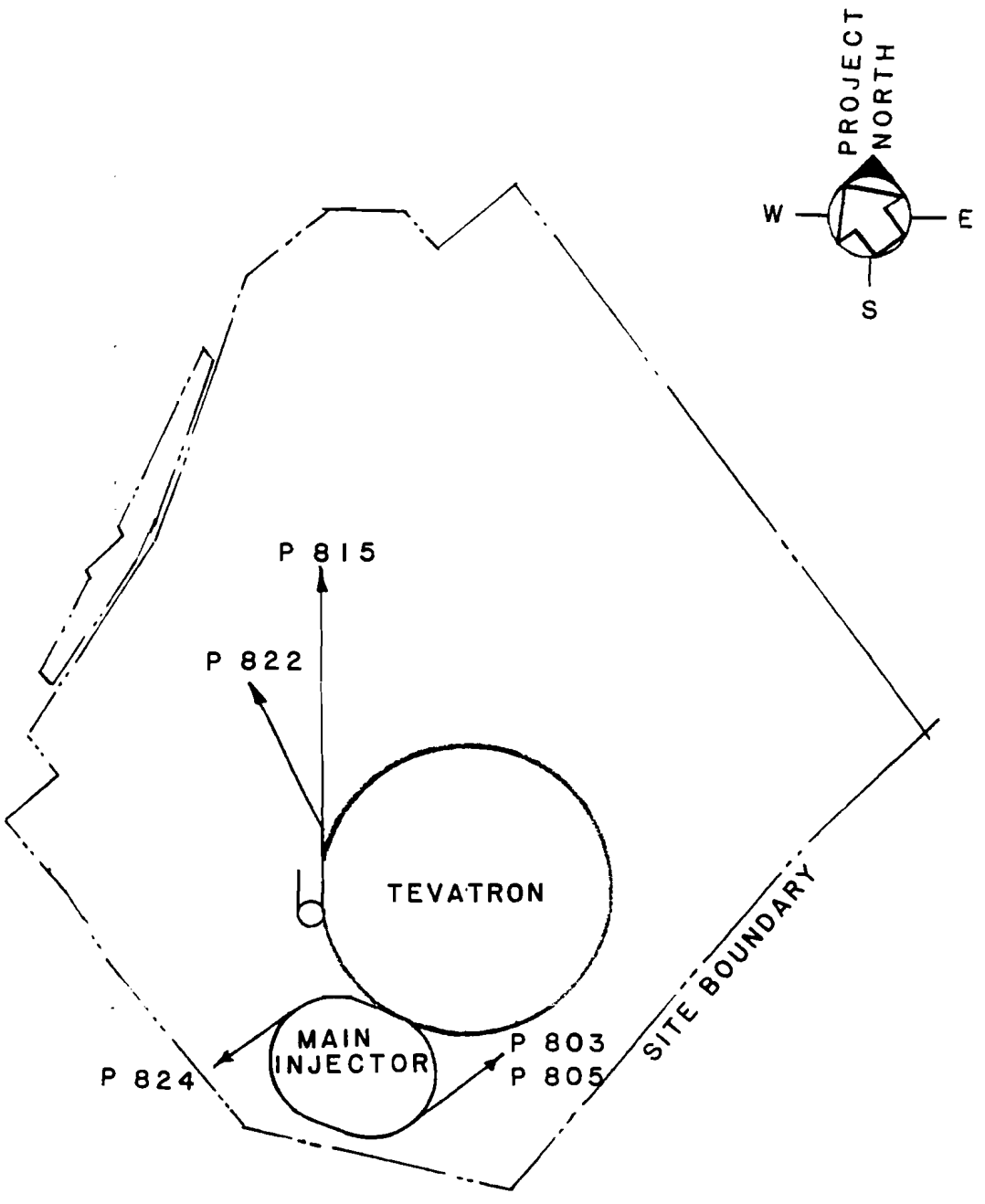

Figure 6.1: Relative Directions of Different Long-Baseline Oscillation Experiments on the Fermilab Site.

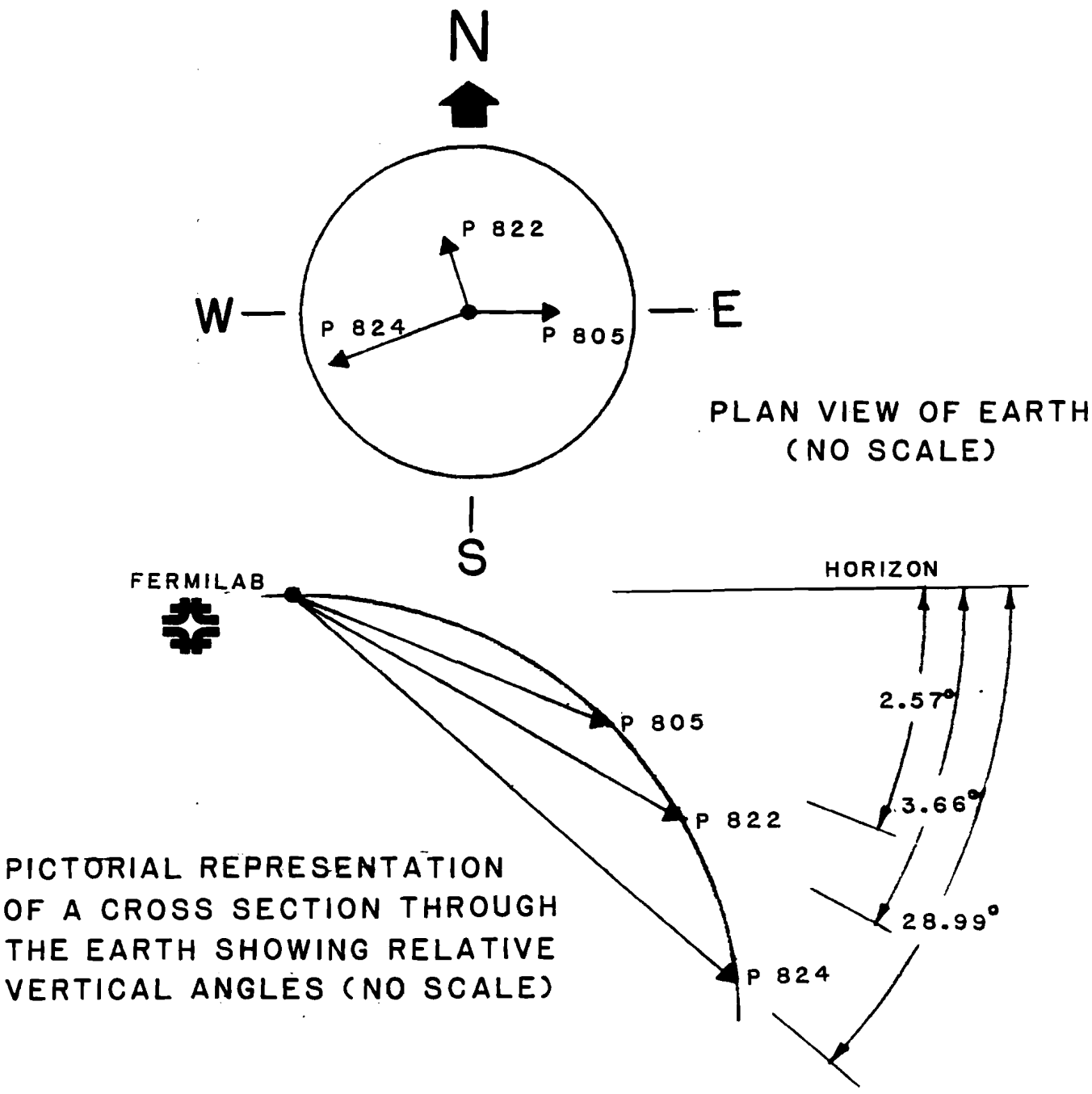

Figure 6.2: Relative Direction of Different Long-Baseline Oscillation Experiments Through the Earth.

Injector. This is the option which we have decided to explore in detail. A significant advantage of this option, the possibility to combine at MI-50 the abort function of the Main Injector with the extraction for the neutrino area is discussed below.

2. P-803 would be placed in the existing neutrino area. We have not worked on this as an option since there seem to be few actual savings over a new area, as will be discussed in Chapter 10.

6.3 Extraction and Proton Transport

6.3.1 The Extraction System and Coupling to Main Injector Abort

The Main Injector Abort system can be conveniently joined to the 120 GeV extraction scheme by coupling the two functions at MI–50. MI–50 is a straight-section of the Main Injector pointed eastward and there is ample room to install a new beamline in that area. The beamline would point as shown in Fig. 6.1. A schematic is given in Fig. 6.3, which shows that we have also allowed for the construction of test beams and future experiments. A more detailed drawing, with a preliminary arrangement of elements, beam monitors, *etc.* is shown in Fig. 6.4 (with values in Table 6.2). This joining of functions and locations can save a significant amount of the cost of this program and result in a net savings to the Laboratory with only minimal, non-disruptive changes to the Main Injector. A task force consisting of members of the Accelerator and Research Divisions now has on-going meetings to design the system and has made significant progress.

There are two potential problems in this plan. First, in the Revision 2.3 of the MI CDR the MI–50 is pointed 225 mr away from IMB. To direct the beam towards IMB would require to locate 10 Main Ring dipoles after the dump, along with an appropriate enclosure.

The second problem arises if the abort comes during a 1 msec ping. We have begun to design a "fail-safe" system which could prevent the aborted beam to strike the neutrino target. However, using the arguments of Section 6.4 it seems that the target could withstand the aborted beam (which comes in one-turn of 10 μsec) and thus there would be no real danger. The Main Injector could also wait to abort for the entire 1 msec if this became necessary.

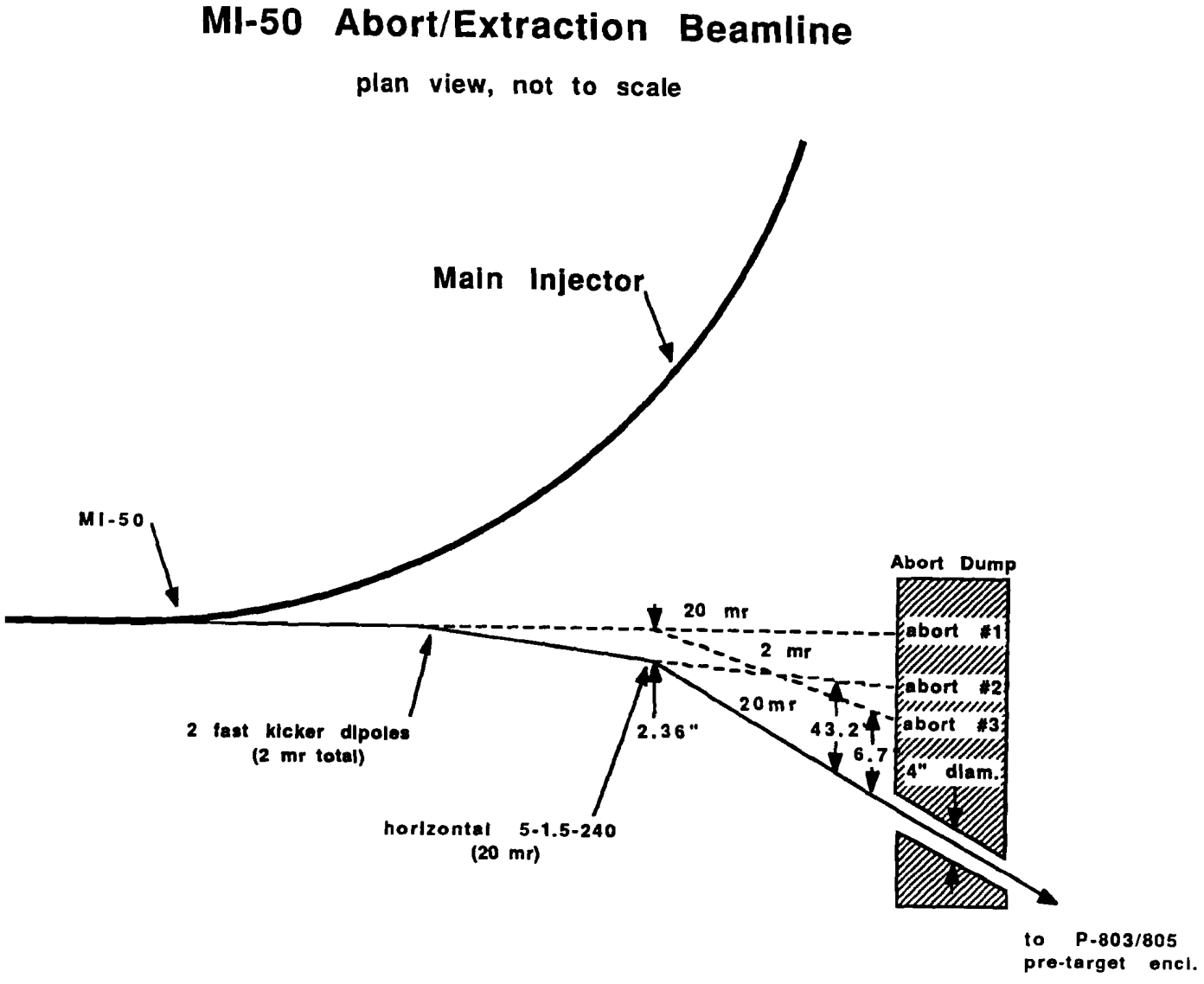

Figure 6.3: Proposed Coupling of Main Injector Abort and Extraction to 120 GeV Program.

6.3.2 Preliminary Design of Abort/Extraction System

For this phase of the pretarget beamline design, the emittance assumptions were modifications of the assumptions and values made in Fermilab TM-1599. The modifications were needed since TM-1599 assumes a 150 GeV beam rather than 120 GeV. The vertical beam size and divergence modifications were made keeping in mind the $1/p$ scaling of the vertical emittance. However, as the design of the Main Injector becomes final, changes may be made which will require changes to our extraction. This design should therefore be regarded as preliminary; we stress the ideas behind and major elements of the system and not the precise details.

It was assumed that the beam leaving MI-50 will be travelling horizontally and will be aimed such that the beam leaving the abort dump will be aimed correctly in the horizontal plane to point the beam toward the IMB detector.[1] The elevation of MI-50 was assumed to be at approximately 715' above sea level.

Our beam elements need to clear those of the MI; to guarantee enough space, we assumed that the first element associated with the new abort/fixed target beamline will be approximately 600' from MI-50. It is further assumed that any correction required to the beamline to make the proton beam ultimately point toward the IMB not explicitly described below will be introduced in the section immediately upstream of this first element.

After the initial beam position/intensity monitors the first optical elements in the proposed beamline are two 3Q120 quadrupoles which make up a doublet. The function of these quadrupoles is to provide an intermediate focus to control the beam size.

The next devices in the beamline are a pair of fast 2.2 m long fast kicker dipoles. Each of the fast kicker magnets will bend the beam horizontally by approximately 1 mr to the west. Their function is to provide an abort. If these magnets are off the protons will be directed to the abort dump further downstream. A backup abort device will be provided by a dipole further downstream, described below.

The next element is a horizontally steering 5-1.5-240 dipole which is 25.25 in. wide. The 5-1.5-240 bends the beam 20 mr to the west. If it is off the beam is sent to the abort dump in one of two different locations separated from one another by about 7 in. horizontally. Two different locations exist because in one case the previously mentioned fast kicker dipoles are assumed to be on at their nomal field and in the other case they are assumed to be off. The two cases for the fast kicker dipoles means that the two trajectories going through this 5-1.5-240 dipole will be separated by about 2.4 in. With our phase space assumptions the horizontal half size of the beam going through this dipole is about 0.43 cm. Therefore, the 5

[1] If the beam must be steered to the east or west, the design presented here would be modified to place any additional steering dipoles downstream of the dump and before the P–803 pretarget area rather than in the Main Injector tunnel.

in. aperture of this dipole should be adequate to accommodate both trajectories within the aperture. The proton beam will be directed through the 4 in. diameter hole in the abort dump if this magnet and the fast kicker dipoles are on at the proper current. This design will send the primary beam to a third abort location about 4.7 in. from the edge of the 4 in. diameter abort dump hole if this 5-1.5-240 is on at its correct field but the fast kicker dipoles are off. Clearly the condition where the westward bending 5-1.5-240 is on while the fast kicker dipoles are off is an abnormal condition so for additional safety we require the fast kicker magnets to be kept off if the 5-1.5-240 is off. By insisting upon the 5-1.5-240 being off if the fast kicker dipoles are off any possible problems arising from having the 5-1.5-240 tuned to the incorrect value is avoided.

A vertical 4-4-30 trim magnet has been provided as the next beamline component. Its function is to provide whatever correction is needed to position the beam properly downstream. It is assumed that horizontal correction can be done by adjusting the current to the 5-1.5-240 that is just upstream.

The abort dump is located approximately 165' downstream of the trim magnet. The position of the dump is somewhat arbitrary. Locating the dump further downstream has the advantages of giving a larger separation between the aborted and transmitted beams, plus giving a larger beam spot size. It will also help in that the intermediate focus is located in the region of the dump and by locating the dump further downstream the beam spot size will be larger than in the present location. On the other hand a small cross sectional size of the beam at the abort dump will make the clearance problems for the beam going through the abort dump hole smaller. The design calls for 150 ft. downstream of the dump before the start of the pretarget enclosure, primarily to allow muons to range-out. In this way, we will have access to the pre-target enclosure while the Main Injector is operating.

The pretarget enclosure has as its initial beamline components beam position/intensity monitors. These are followed by a pair of vertical fast kicker magnets which bend the proton beam by a total of 2 mr downward. The kicker magnets in this enclosure are intended to help protect the horn. If the primary beam drifts off the target the fast kicker magnets should be turned off. Immediately downstream of the second kicker magnet is a horizontally focusing quadrupole and then a downward bending 5-1.5-240 dipole. If the downstream end of the dipole can have a part of the aperture filled by an insert the protons can be dumped there in an emergency dump. With the kicker magnets off, the beam will shift by about 1 in. from the standard trajectory by the time they reach the downstream portion of the first downward bending dipole even without the additional vertical steering of the quadrupole. The vertical beam half size at the downstream end of the first 5-1.5-240 is about 1.6 cm. Thus, the insert should not have any significant impact on the normal trajectory of the primary beam with the kicker magnets on at their proper fields.

There are 3 quadrupoles in the pretarget enclosure. They are configured as a triplet with the first and third quadrupole in series focusing the beam horizontally while the middle

quadrupole defocuses horizontally. The triplet quadrupoles focus the beam onto the production target. Interspersed between these quadrupoles are two 5-1.5-240 dipoles which bend the beam downward. The dipoles aim the beam downward so that the beam leaving these dipoles now point approximately 45 mr downward toward the neutrino production target and IMB. The final quadrupole in this enclosure is followed by a horizontally steering 4-4-30 trim magnet.

The distance between the downstream end of the horizontal trim magnet and the upstream end of the first target is approximately 53 ft. Within this region and just upstream of the target are beam position/intensity monitors. The bulk of the 53 ft. between the trim magnet and the first target is drift space. The drift space (1) permits the beam incident on the target to be more parallel than would be the case if the drift space was shorter, (2) allows for the easier installation or the removal of the target/horn train system from/to the area parallel to the pretarget devices, and (3) permits the installation/removal of the horn train without the relocation of any of the beamline devices.

The design requirements call for the beam spot size on target to be less than 1.33 mm in radius. As can be seen from Fig. 6.6 the spot size requirement has been satisfied. The positions of the vertical and horizontal minima have been chosen deliberately to be located at different locations while meeting the 1.33 mm criteria. The differing locations help to reduce the energy density deposited by the incident protons at any one location of the target, thus reducing the threat of destruction of the target by the primary beam.

Failure of any critical device in this beam poses no danger to personnel; rather, it would result in the beam being mis-steered and hitting another element. Furthermore, the Main Injector designers have agreed that the Main Injector can wait up to 1 msec for the kicker to be turned off before the abort occurs.

The target itself would survive direct hits over a period of minutes from the aborted Main Injector beam; hence a one-turn accident poses no significant danger to the target. In contrast, the horn would probably not survive a one-pulse hit by the beam. An annulus will protect the horn; an annulus is a thick instrumented collimator with a hole, shadowing the target but much smaller than the horn. A monitor on the annulus detects scraping and then can serve as a critical device to further protect the horn from the mis-steered beam.

Assuming the Main Injector Lattice of Revision 2.3 we have completed a preliminary proton transport design with the above coupling. We show below the beam envelope along the transport path and in the region of the target in Figs. 6.5 and 6.6. We see that the beam remains small with respect to the 3 mm. target across its length.

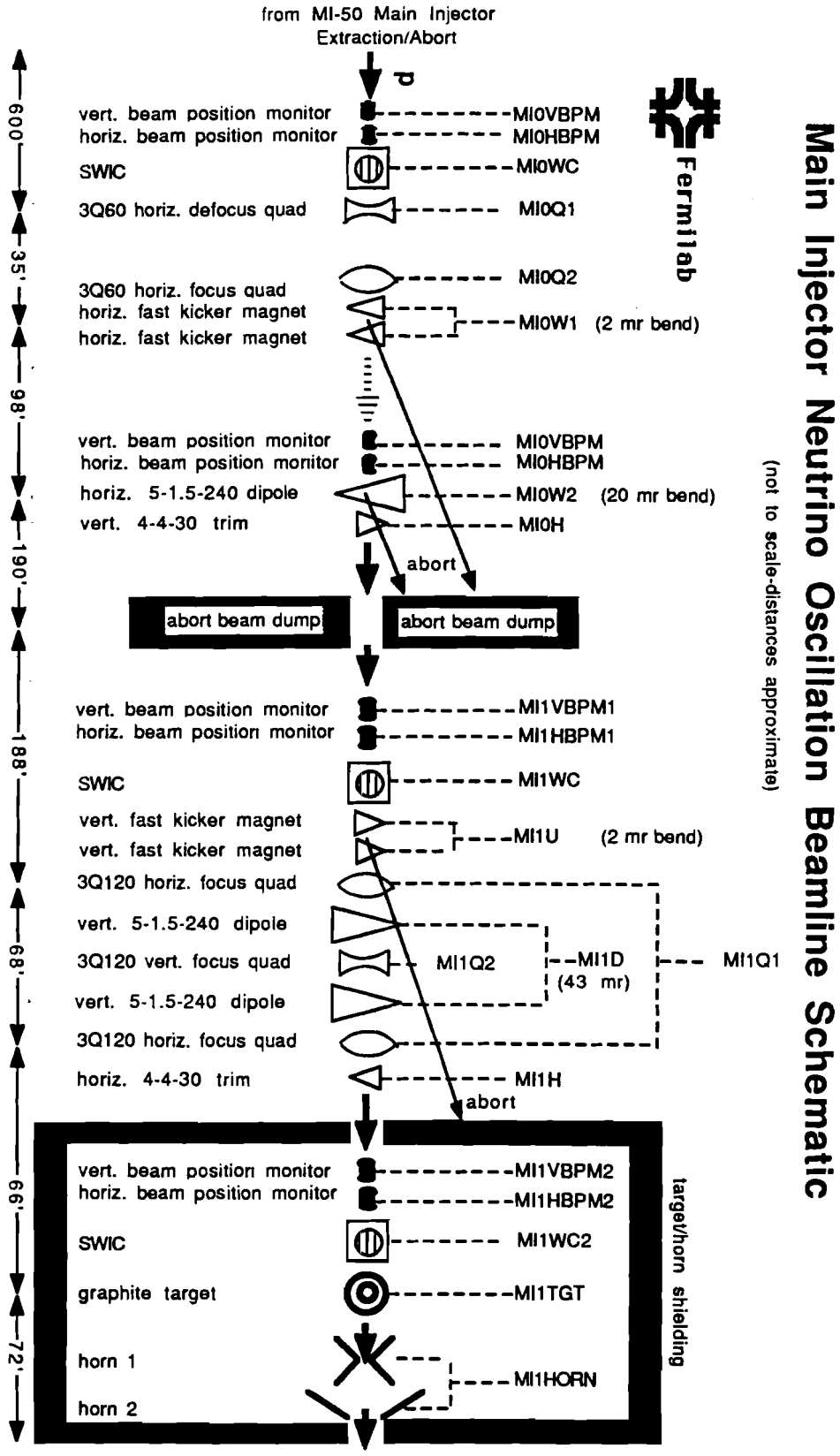

Figure 6.4: Schematic Drawing of MI/120 GeV Line

Z CENT.	X CENT.	Y CENT.	ELEMENT CODE	FIELD (KG/IN)
602.50	0.00	715.09	3Q60 Quad, HORIZONTALLY FOCUSING	-3.635
622.50	0.00	715.09	3Q60 QUAD, HORIZONTALLY FOCUSING	3.760
630.61	0.00	715.09	2.2 M LONG FAST KICKER MAG., BENDS 1 MR	1.818
639.83	-0.01	715.09	2.2 M LONG FAST KICKER MAG., BENDS 1 MR	1.818
655.44	-0.04	715.09	FUTURE 5-1.5-240 DIPOLE FOR TEST BEAM	0.000
733.43	-0.30	715.09	HORIZONTAL 5-1.5-240 DIPOLE	13.133
746.68	-0.49	715.09	VERTICAL 4-4-30 TRIM	0.000
933.39	-4.60	715.09	UPSTREAM END OF ABORT BEAM DUMP	
1083.35	-7.90	715.09	U.S. END OF PRE-TARGET ENCLOSURE	
1091.96	-8.08	715.08	2.2 M VERT. FAST KICKER MAG., 1 MR BEND	-1.818
1101.17	-8.29	715.07	2.2 M VERT. FAST KICKER MAG., 1 MR BEND	-1.818
1111.78	-8.52	715.06	3Q120 QUAD, HORIZONTALLY FOCUSING	2.214
1128.78	-8.90	714.91	VERTICAL 5-1.5-240 DIPOLE	-14.119
1145.77	-9.27	714.62	3Q120 QUAD, HORZONTALLY DEFOCUSING	-3.451
1162.76	-9.64	714.11	VERTICAL 5-1.5-240 DIPOLE	-14.19
1179.74	-10.02	713.46	3Q120 QUAD, HORIZONTALLY FOCUSING	2.214
1187.98	-10.20	713.09	HORIZONTAL 4-4-30 TRIM	0.000
1242.16	-11.39	710.65	UPSTREAM END, PRODUCTION TARGET	
2296.84	-34.60	663.14	UPSTREAM END OF 10 METER BEAM DUMP	
2984.97	-49.74	632.14	UPSTREAM END OF P803 DETECTOR HALL	

Table 6.2: Beam-Sheet for Combined MI Abort/120 GeV Extraction System.

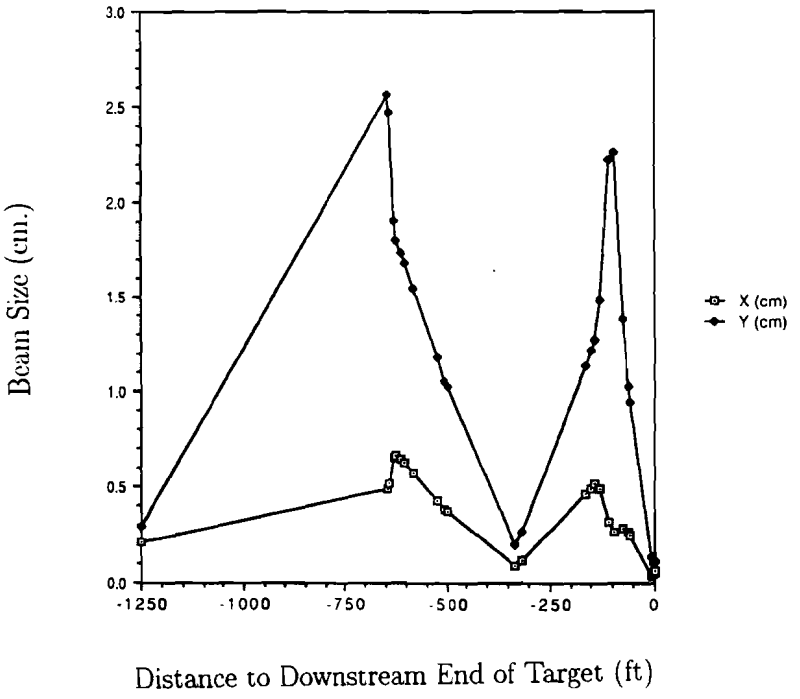

Figure 6.5: Overall View of Beam Envelope. The Horizontal and Vertical Half-Sizes are plotted *vs.* location. The half-size is the distance from the center to the 2σ edge.

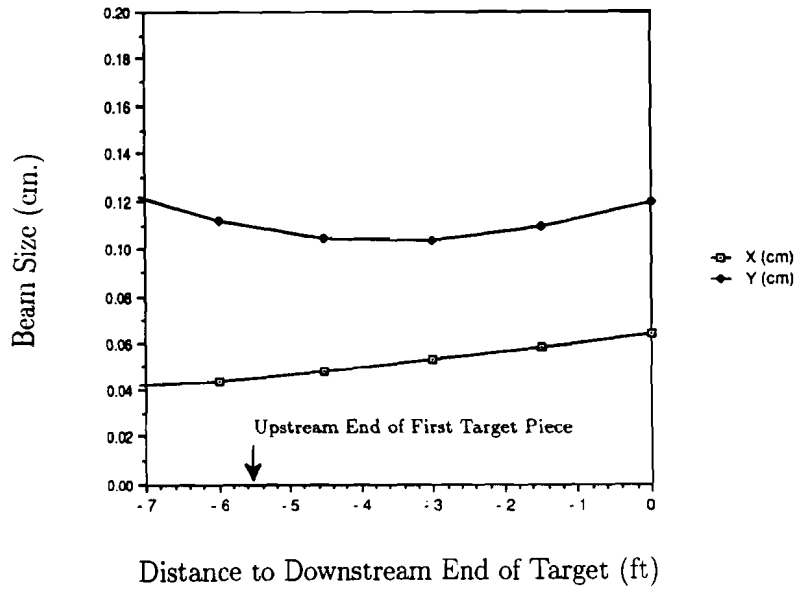

Figure 6.6: Beam Envelope near Target. The Horizontal and Vertical Half-Sizes are plotted *vs.* location. The half-size is the distance from the center to the 2σ edge.

6.3.3 Instrumentation of Proton Transport System

The instrumentation required for use with the proton transport system will require special considerations:

- Accurate knowledge of the incident proton flux on target is vital.
- Instrumentation to measure the position and angle of the beam on target is critical. The ν_e/ν_μ fraction in the beam is dependent on targeting angle and since the experiments are measuring this ratio, the fraction of ν_e contamination in the beam must be well known.
- At the moment the target that is being considered is 3 mm in radius and is 2 meters in length although some of the 2 meters will be voids. With such a thin target, the optics (and even survival!) of the horn depend on controlling and monitoring the incident proton beam.

These instruments must survive in an area which will be taking an unprecedented intensity of protons, making the installation, maintenance, repairs and decommissioning of the beam particularly difficult. The design for the proton transport system must take into consideration what will be needed to repair or replace components such as magnets and instrumentation, in addition to the target and the horn focusing system. The devices which are in the region of the target will become extremely radioactive after exposure to the beam. The design of the proton transport system must therefore keep personnel radiation exposure as low as reasonably possible. To this end a rail transport system is under consideration to carry the beamline elements which will have to be able to furnish all of the utilities needed, *e.g.*, power, gas, cooling, and vacuum. The transport system must also have a remote alignment capability, since some components such as the horns will be in areas which are inaccessible to personnel and may also be highly radioactive.

6.4 Target

A target of high efficiency for the production of neutrinos consists of a free rod with a small diameter which is irradiated with a beam which has at most the same diameter as the target. This ensures that the secondaries emitted at non-zero angle quickly escape laterally from the target material. The production target is modeled after a CERN design.[13]

To produce neutrinos from the Main Injector, we propose to use a target consisting of 11 cylindrical rods made of graphite, each 10 cm long and 6 mm diameter. Each rod is supported from both ends by graphite plates 1 mm thick. The spacings between such segments are 9 cm long, so the total length of the target is 2 m.

Table 6.3 lists the properties of the material which is most suitable for the proposed target: graphite grade ZXF-5Q produced by POCO Graphite, Inc.[3]

melting temp	$3600°C$
sublimation temp	$3320°C$
density ρ(g/cm^3)	1.81
specific heat c_p(cal/g $°C$)	0.17
coeff. of thermal expansion $\alpha(/°C)$	7.7×10^{-6}
thermal conductivity λ(cal/sec cm $°C$)	0.29
modulus of elasticity E(N/mm^2)	14.5×10^3
flexural strength (N/mm^2)	124
compressive strength (N/mm^2)	193
tensile strength (N/mm^2)	90
strain to failure (%)	0.78
Poisson's ratio	0.20 @ $1000°C$

Table 6.3: Properties of ZXF-5Q Graphite of POCO Graphite Inc.

We provide arguments showing that a target of such construction can sustain the full capacity of the proton beam produced by the Main Injector, with a cycle time of 1.9 sec and a spill time of 1 ms.[9]

6.4.1 Energy deposition by the proton beam in the target.

The energy deposition by the proton beam in the target material has been calculated with the FLUKA Monte Carlo program [4]. This program, commonly applied for similar purposes at CERN, provides energy deposition results which are slightly higher than other packages such as CASIM [5], GEANT & GHEISHA [6].

In these calculations we made the assumption that the proton beam intensity has a Gaussian radial distribution. The width of this distribution is such that 92% of protons enter the front surface of the target. It translates to an RMS for the distribution $\sigma = R/2.248$ and a FWHM $= 2.355 \times \sigma = 1.05 \times R$, where R is the radius of the target rod (3 mm). The calculations are made for an unsegmented target, neglecting the escape of secondaries within the gaps. This assumption makes the calculations slightly pessimistic but does not have a significant effect on the final results.

The energy deposition density $E(r)$ as a function of the distance from the target axis (r) is shown in Fig. 6.7.

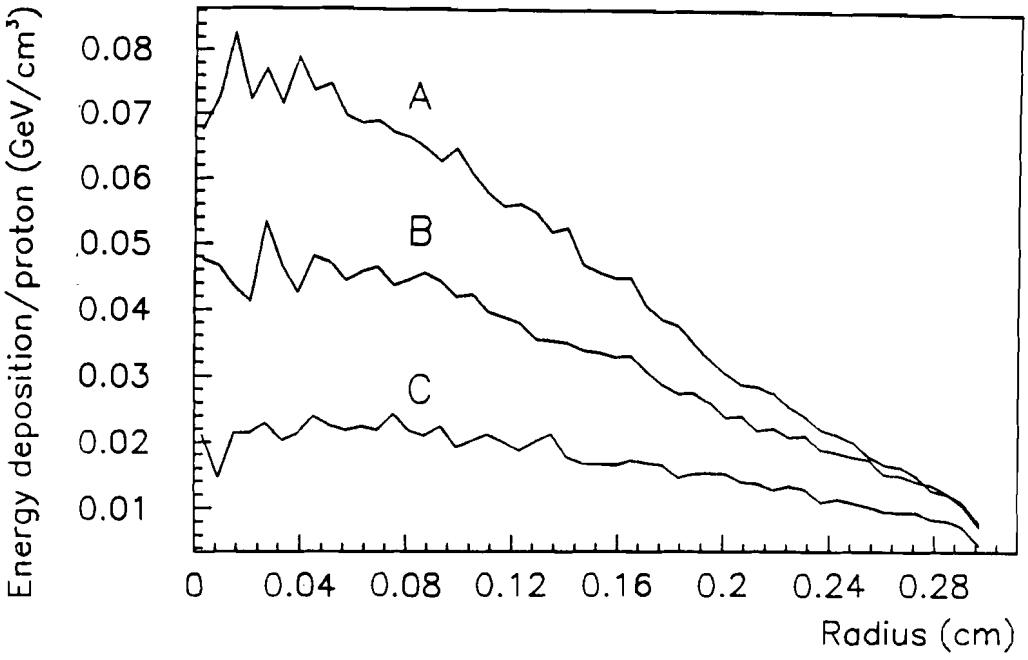

Figure 6.7: Radial energy deposition density in the 6 mm diameter graphite target for a 120 GeV proton beam: (A) for the second (and hottest) target segment; (B) for the sixth (center) segment; (C) for the last segment.

The energy deposition density can be translated into a temperature distribution in the target using the formula:

$$T(r) = 3.82 \times 10^{-11} \frac{E(r)}{c_p \rho} \Phi \tag{6.1}$$

where c_p is specific heat (cal/g $^\circ C$), ρ is the density (g/cm^3) of the target material and Φ is the number of protons in the beam burst.

As discussed later, the characteristic constants for graphite–its specific heat, coefficient of thermal expansion, and modulus of elasticity increase with temperature. However, while the specific heat increases by a factor of two between room temperature and $1000^\circ C$, the product of the expansion coefficient and Young's modulus increases only by $\approx 60\%$. For this reason we discuss the thermal stresses of the target at room temperature as the most severe conditions for target survival.

From Fig. 6.7 we see that the radial temperature distribution in the target is approximately linear in r and can be described by the formula:

$$T(r) = T_0(1 - \frac{r}{R}) \tag{6.2}$$

with the highest value of T_0 being $320\ ^\circ C$, corresponding to the largest $E(r) \approx 0.085$ GeV/cm^3 per proton and a beam intensity of 3×10^{13} protons/pulse.

This temperature distribution is almost adiabatic for the spill times of the order of few miliseconds. The evolution of temperature due to thermal diffusion is given by:

$$T(r,t) \sim exp(-\frac{r^2}{4at}) \tag{6.3}$$

where $a = \lambda / c_p \rho$ is the thermal diffusivity which for the graphite is equal to 0.93cm^2/s. The time required for the *RMS* value of the radial temperature distribution to be equal to the radius of the target is 48 ms, which is long compared to the spill time.

6.4.2 Quasi-static thermal stresses in the target

Fast and non-uniform heating of the target material together with its thermal expansion create material stresses which, if too large, can destroy the target.

The circumferential (σ_ϕ), radial (σ_r) and longitudinal (σ_z) stress components are given by:[10]

$$\sigma_\phi = \frac{\alpha E}{1 - \nu} [\Phi(R) + \Phi(r) - T(r)]$$

$$\sigma_r = \frac{\alpha E}{1-\nu}[\Phi(R) - \Phi(r)]$$
$$\sigma_z = \frac{\alpha E}{1-\nu}[2\Phi(R) - T(r)]$$

where

$$\Phi(x) = \frac{1}{x^2}\int_0^x T(r) r dr \tag{6.4}$$

and α is the coefficient of thermal expansion, E is the modulus of elasticity and ν is the Poisson ratio ($\approx 1/5$ for graphite).

Substituting the assumed temperature distribution in the target, one finds:

$$\sigma_\phi = A\frac{2r-R}{R}$$
$$\sigma_r = A\frac{r-R}{R}$$
$$\sigma_z = A\frac{3r-2R}{R}$$

where

$$A = \frac{1}{3}\frac{\alpha E T_0}{1-\nu} \approx \frac{5}{12}\alpha E T_0 \tag{6.5}$$

According to the maximum shear theory, a material becomes plastic if the largest difference between two out of these three stress components exceeds the yield strength of the material. One can see from the formulae that this maximum difference is equal to:

$$\sigma_0 = A \tag{6.6}$$

which, in the center, is due to $(\sigma_\phi - \sigma_z)$ and $(\sigma_r - \sigma_z)$ and on the surface due to $(\sigma_\phi - \sigma_r)$ and $(\sigma_z - \sigma_r)$. The value of A in our condition is equal to 15 N/mm^2 which is comfortably below both the compressive and tensile strength of the graphite ZXF-5Q. It means that the target will neither overexpand from the center nor crack on the surface.

6.4.3 Dynamic thermal stress

When the heating time of the material is comparable to the sound propagation time along the target, the created wave may destroy the target if the wave stress exceeds the yield strength of the material. This dynamic stress is given by the formula:

$$\sigma_z^{dyn} = \begin{cases} \frac{1}{3}E\alpha T_0 & \text{for } l > \tau v_{sound} \\ \frac{1}{3}E\alpha T_0 l/(v_{sound}\tau) & \text{for } l \leq \tau v_{sound} \end{cases} \tag{6.7}$$

For our graphite $v_{sound} = \sqrt{E/\rho} = 2.9 \times 10^5$ cm/s, which for the pulse duration $\tau = 1$ ms, gives $v_{sound}\tau = 290$ cm. Thus the dynamic stress, which is in any case below the graphite yield strength, is decreased further by a factor of 1/29 and does not create any danger for the stability of the target.

6.4.4 Discussion of the choice of the target size

The choice of target radius is dictated by a compromise between the thermal stresses and the losses of the secondaries in the target material. First, let us consider the fraction of secondary particles which are absorbed as they pass radially outward through the target. The yield drops by 7% in changing the target diameter from 1.5 to 3.0 mm and by 20% in changing from 1.5 to 6.0 mm.[11]

The stresses have their maximum value of $E(r)$ at the target axis $r = 0$. This value dramatically increases as the target size decreases (with a corresponding decrease of the beam size $\sigma = r/2.248$). For $r = 1$, 2, and 3 mm the values of $E(0)$ are 0.085, 0.2, and 0.7 GeV/cm^3 respectively. An intensity of 3×10^{13} for these radii correspond to instantaneous temperature rises of 2600, 750, and 320°C. The maximum stress for radii of 1, 2, and 3 mm are 120, 35, and 15 N/mm^2. Looking at the strength properties of Table 6.3, combined with yields and temperature rises lead us to choose a target of r = 3 mm and a beam size of $\sigma =$ 1.34 mm.

6.4.5 Target cooling

In removing the thermal energy deposited in the thin target rods we are constrained by the need to avoid the use of high density material which would absorb secondaries and destroy the azimuthal symmetry of the beam. A practical solution is to support the rods at their ends with thin graphite plates and cool them with forced gas convection. The most efficient cooling can be obtained using Helium. Helium has the additional advantage of providing a neutral atmosphere for graphite, which would burn in air.

The natural convection in Helium (no Helium flow) is determined from the relationship between the Nusselt, Grashof, and Prandtl numbers.[9] For a cylindrical target 6mm in diameter one gets:

$$k_c \approx 16 \times 10^{-4} (\text{cal/cm}^2 \text{ s } °C) \tag{6.8}$$

For a transverse gas stream the coefficient of convection can be calculated from an equation bounding Nusselet, Reynolds and Prandtl numbers:

$$k_c = C\ v^{0.466}\ d^{-0.534}\ (\frac{T_R}{T_m})^{0.117} \tag{6.9}$$

where v is the gas velocity, d is the diameter of the rod, T_R is its absolute temperature, and T_m is absolute temperature of the gas. One can see from this formula that the coefficient of convection k_c is $\approx \sqrt{v/d}$, while its dependance on the temperatures is very weak (special arrangements for cooling of the Helium gas do not improve the convection cooling). For further calculations we will use:

$$k_c = C\ v^{0.466}\ d^{-0.534}\ \ (\mathrm{cal/cm^2\ s\ ^\circ C}) \tag{6.10}$$

with $C \approx 58 \times 10^{-4}$ when v is measured in m/s and d in mm.

As one can see in Fig 6.7 the largest energy depositions are in the first two segments of the target. The mean energy deposited in the first segment is 0.029 GeV/cm^3/proton, while in the second it is 0.031 GeV/cm^3/proton, which translates to a temperature rise of 143°C and 153°C respectively, when the initial temperature is room temperature. This temperature rise depends on the initial temperature because the specific heat (c_p) is temperature dependent and varies from 0.17 cal/g °Cat room temperature to about 0.4 cal/g °Cat 1000 °C.(see Fig 6.8). The data presented in Fig 6.8 can be fit by the formula:

$$c_p = -0.827 + 0.177\ ln(T)\ \ (\mathrm{cal/g^\circ K}) \tag{6.11}$$

which reproduces the measured values with an accuracy of few percent. Then the temperature rise due to the energy deposited (ΔE) in the target rod by 120 GeV proton beam should be calculated from a more complex formula than that given before:

$$\int_{T_{in}}^{T_{fi}} c_p(T)\ dT = 3.82 \times 10^{-11} \frac{\Delta E}{\rho}\ \Phi \tag{6.12}$$

where ΔE is measured in GeV/cm^3 per proton and Φ is the number of protons in the beam burst.

The heat balance during the accelerator cycle is described by the equation:

$$c_p \rho V \frac{dT}{dt} + \epsilon \sigma_B S(T^4 - T_m^4) + k_c S(T - T_m) = 0 \tag{6.13}$$

considering the heat losses by radiation and convection. After the target had been heated by a beam burst, this equation was solved using a Runge- Kutta method [7]. Independently, the computer program ACSL [16][8] was used to investigate the evolution of temperature as a function of time. A cooling time between the beam bursts of 1.9 sec was assumed. The cycles of heating and cooling were repeated starting from the initial temperature $T_{in} = T_m = 300^\circ K$ until the dynamic equilibrium was reached. This was achieved after about 30 cycles. The calculations were performed for cooling by radiation only, radiation and natural convection, and for radiation and convection cooling at various velocities of Helium. The results are presented in Fig 6.9. They represent the temperature variation at the thermal equilibrium of the hottest segment *i.e.* the second segment of the target. The hatched area represents the

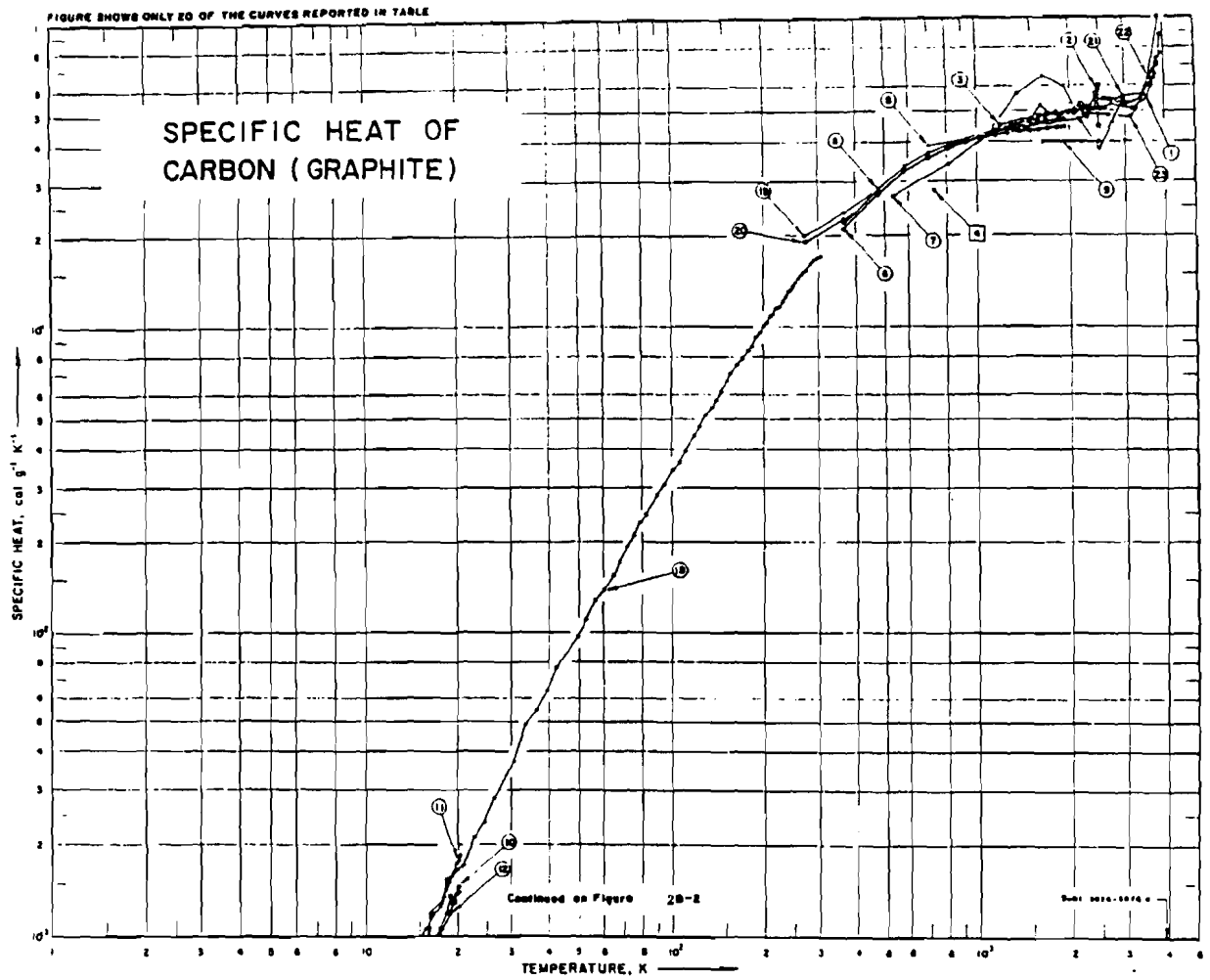

Figure 6.8: The specific heat of graphite as a function of temperature.

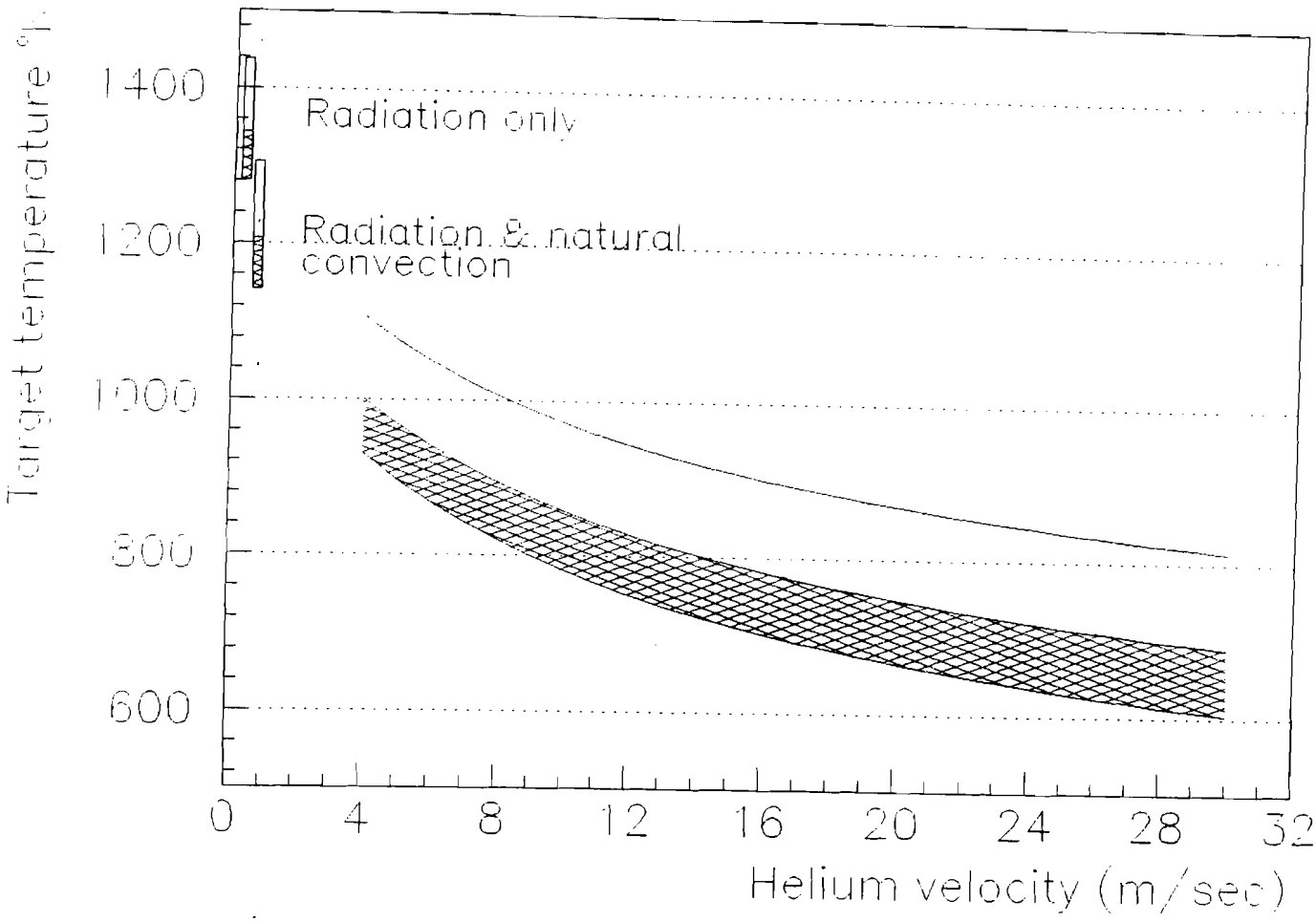

Figure 6.9: Temperatures of the target for different velocities of the cooling helium gas. The lowest curve is the temperature at equilibrium, the next higher for temperatures after every beam spill, the highest is for the hottest place in the target. The curves are calculated at 4×10^{13} protons/1.9 sec pulse, somewhat higher than the expected intensity.

range of the rod's mean temperatures during the cooling cycle: the lower boundary shows temperatures before the beam burst, and the upper one gives the temperatures just after the beam burst. The highest curve shows the temperatures of the hottest point on the rod axis.

None of these temperatures approach the graphite sublimation point, however, they are significantly above the ignition temperature in air. Cooling by radiation only, would thus require evacuation of the target box. Since it is technically easier to provide a modest flow of Helium gas through the target box than to evacuate it, Helium convection cooling is the most economical solution. The additional advantage provided by such cooling lowers the temperature range by as much as $400°C$. This also helps decrease the slow sublimation of the target material.

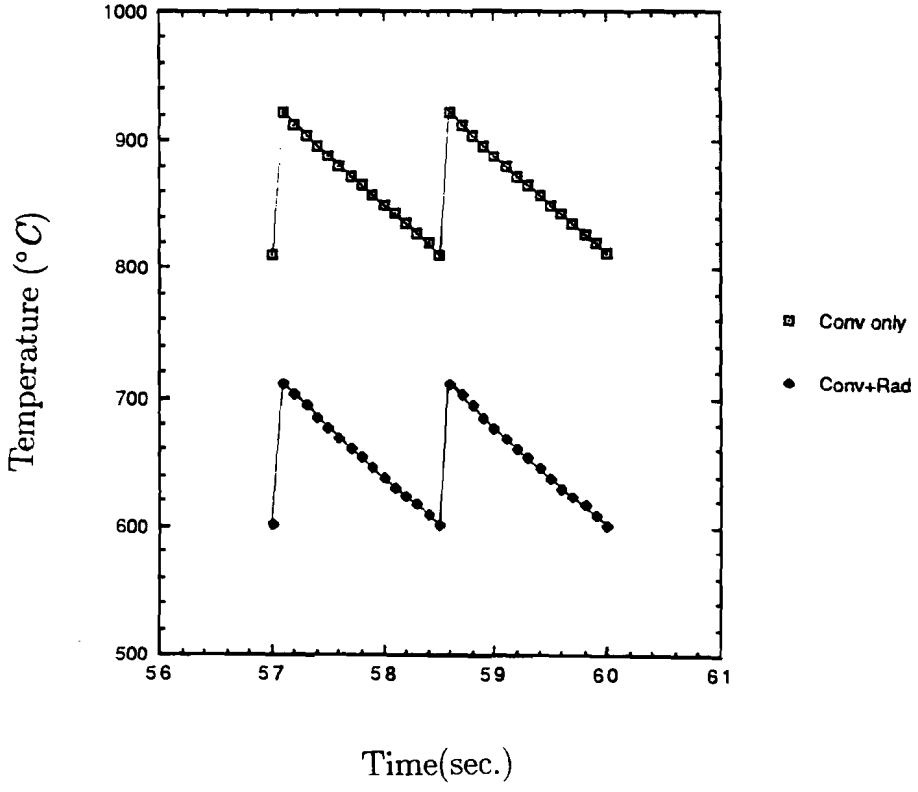

Figure 6.10: Radial temperature distribution in the 6 mm target as a function of time after the steady state has been achieved. The top curve is for radiative cooling, the bottom for both radiative and convective cooling.

6.5 The Double Horn

A simple wide-band double horn system has been designed in order to maximize flux while maintaining overall reliability.

In order to understand how a two horn focusing system works we present the following, very simplified considerations. A horn is a cylindrically symmetric current sheet as shown in Fig 6.11. The magnetic field between the inner and outer conductors is trivially calculated from Ampère's Law:

$$B = \frac{\mu_o}{2\pi}\frac{I}{r} \tag{6.14}$$

where $\mu_o/4\pi = 10^{-7}$ N/A. When the current I is measured in kA, the distance from the symmetry axis r in cm (it is important to note that r is a distance from a *local* azimuthal symmetry axis of the current sheet which may be different from the ideal axis of the conductor due to deformations like sagging caused by its weight), $B = I/5r$ is obtained in kGauss. There is no magnetic field inside the inner conductor or outside the outer conductor. Hence particles which stay within the inner conductor are unaffected; if particles of the appropriate charge pass outside the horn, they are focused back in.

The trajectory of a charged particle in such a field cannot be expressed by an analytical function, but can be easily determined by numerical methods. The bending angle of the trajectory in the field is given by:

$$\int \frac{B\ dl}{p} = \frac{10^{10}}{c}\,\theta \tag{6.15}$$

if B is in kGauss, l in m, c in m/sec, and p in GeV/c. In further analysis we assume, that a particle along its trajectory is moving in a magnetic field of such strength as at the entrance to the field. After substituting B and noting that the transverse momentum $p_t = p\ \theta$ we get:

$$\frac{l}{r} = \frac{165}{I}\ p\ \theta = \frac{165}{I} p_t \tag{6.16}$$

Thus keeping the ratio l/r constant (conical shape of the current sheet) we obtain a device focusing particles of the same transverse momentum.

The system of two horns is shown schematically in Fig 6.12. The first horn is designed to focus certain $p_{t1} = p\theta_o$. The second horn focuses $p_{t2} = p\theta_2$ so the whole system focuses

$$p_t = p_{t1} \pm p_{t2} = \frac{I}{165}\left(\frac{l_1}{r_1} \pm \frac{l_2}{r_2}\right) \tag{6.17}$$

As discussed later, the first horn is made of two cones, each with $l_1 \approx 2$ m and $r_1 \approx 6$ cm, so it focuses $p_t \approx 2 \times \frac{2}{6} \approx 0.67$ GeV/c if the current $I \approx 165$ kA. This p_t region is at the

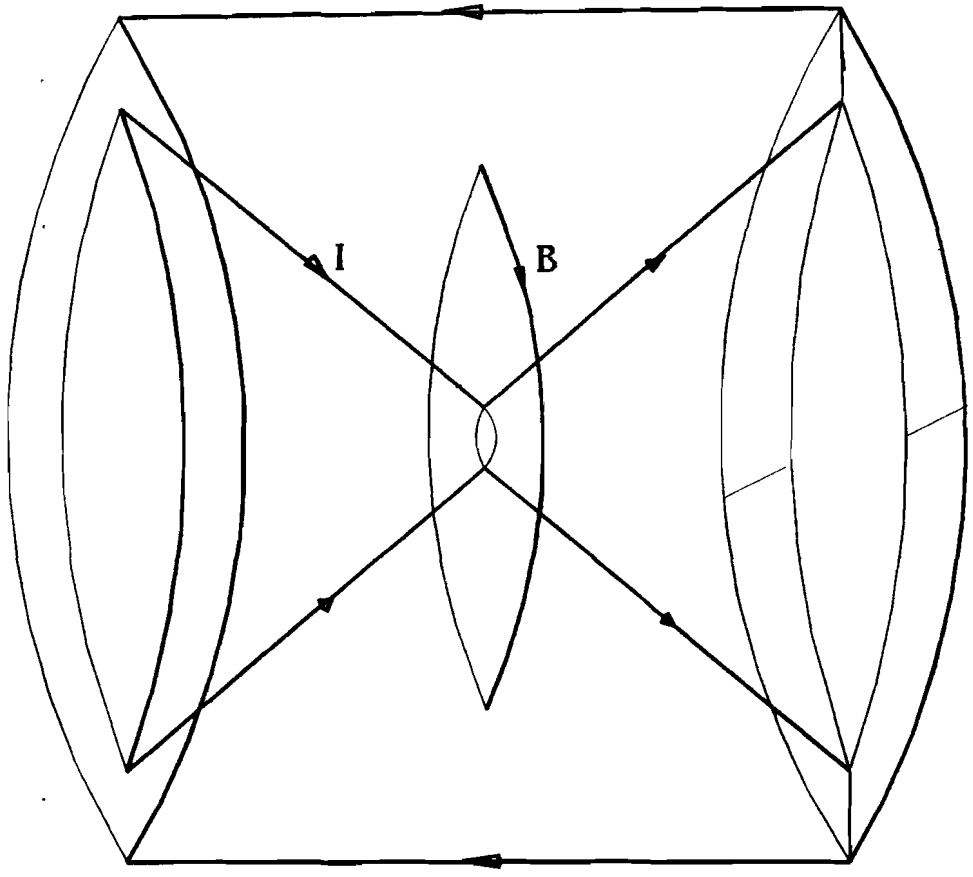

Figure 6.11: Cylindrically symmetric current sheet called a horn.

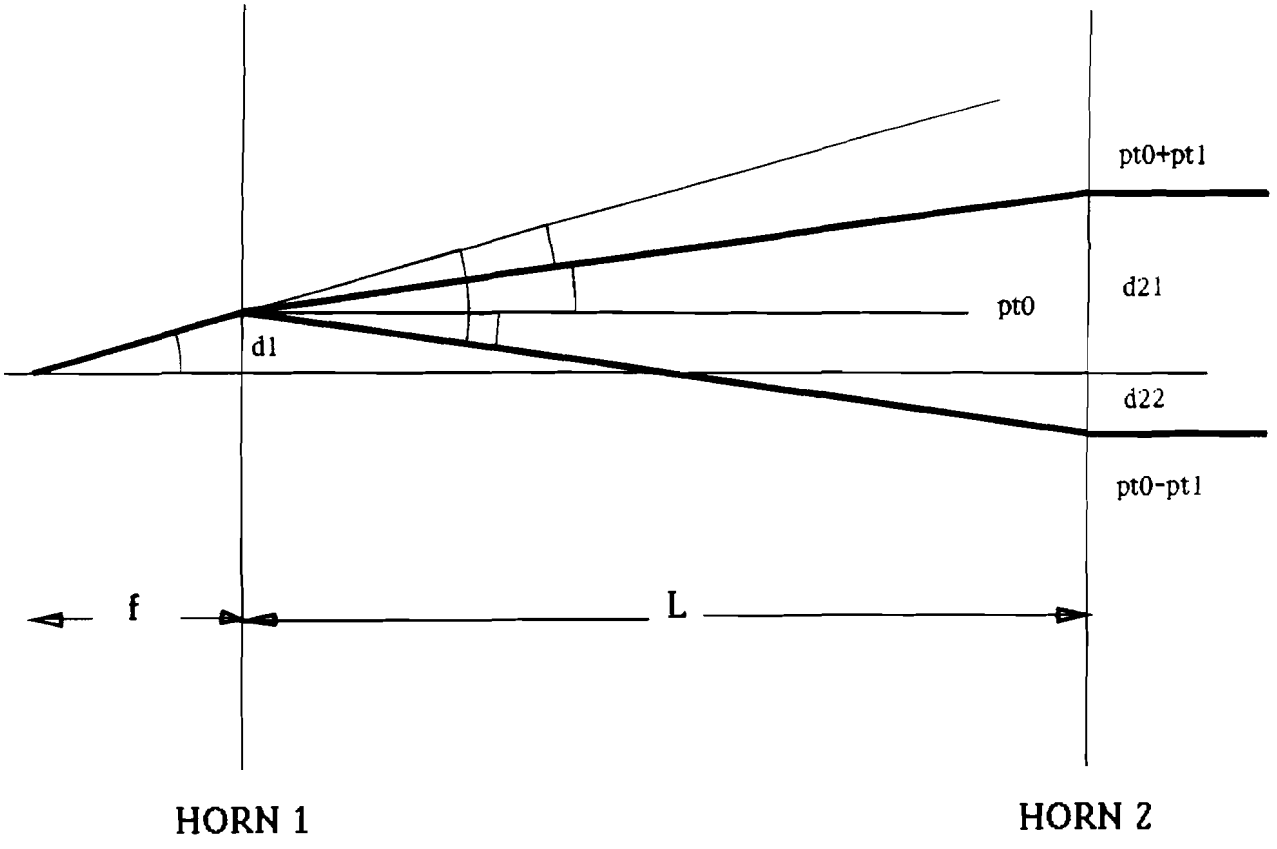

Figure 6.12: Optics of the Double Horn System.

maximum of production in the laboratory system. The second horn is a single cone with $l \approx$ 3 m and $r \approx 15$ cm, so it focuses $p_t \approx \frac{3}{15} \approx 0.2$ GeV/c. Thus the whole system focuses $p_t \approx$ 0.67 ± 0.2 GeV/c.

The acceptance of the horn system depends on the incident angle and for a particular focusing value of p_t, on the initial momentum. It is apparent that the acceptance of the first horn depends on the distance from the target to the center of the horn and on the horn radius. For a target 2 m long whose center is 4 m distant from the horn center the acceptance is 20 mrad for the close end of the target and 12 mrad for the far end. Remembering that the horn is designed to focus $p_t \approx 0.65$ GeV/c, this acceptance acts to cutoff particles with momenta $p < 35$ GeV/c for the close end and $p < 55$ GeV/c for the far end. This cutoff is not so sharp due to the existence of the second horn.

The distance between the horns (L) must be at least such that the particles with $p_t \approx$ 0.65–0.2 GeV/c have enough range to cross the symmetry axis of the horn system and enter the second horn: $L > \frac{0.06}{0.2}\, p \approx 0.3 \times 40 \approx 12$ m. On the other hand the distance must be short enough so the particles with $p_t \approx 0.65 + 0.2$ GeV/c are accepted i.e. $L < \frac{0.10}{0.2}\, p \approx 0.5 \times 40 \approx$ 20 m. These simple considerations are provided only to give a rough glimpse in understanding how the double horn focusing system works. Its correct optimization require application of numerical methods. Some further details are discussed further in this document.

As has been mentioned before, the first horn looks like a "conical vee", while the second horn is a cone. Fig. 6.13 shows the layout. There is about 15 meters between the two horns. For simplicity, this region will not be evacuated. It represents about 2% of an interaction length and 5% of a radiation length of air at STP. The inside diameters of the inner conductors are made relatively large so that the primary proton beam is unlikely to strike them. The trade-off between the wall thickness required to withstand the axial forces and the radius inside the narrow neck determines how far the proton beam can move without hitting the inner conductor and possibly melting it.

The characteristic feature of the "vee" design is that particles of low momentum and wide angle continue to be focussed toward the axis but not over-focussed in such a way as to miss the second horn. Particles of the correct charge are bent toward the horn, pass through it, and then enter the $B = 0$ region. The combination of Horn # 1 and Horn # 2 has a high efficiency for capturing particles out to $p_\perp = 0.9$ GeV/c. Fig. 6.14 shows the neutrino flux as a function of energy for the short-baseline experiment. The computer program NUADA is used with the following parameters: (a) a two interaction length continuous target, (b) 320 m. decay region, (c) shield and recess of 220 m., (d) detector radius 1 m., (e) 170 kA horn current, and the production spectrum of Fermilab FN–349. The same Figure also indicates the efficiency for the proposed double horn compared to the "perfect focusing" case. Fig. 6.15 shows the same result in terms of event rate rather than flux.

Particles which decay in flight will encounter three distinct regions:

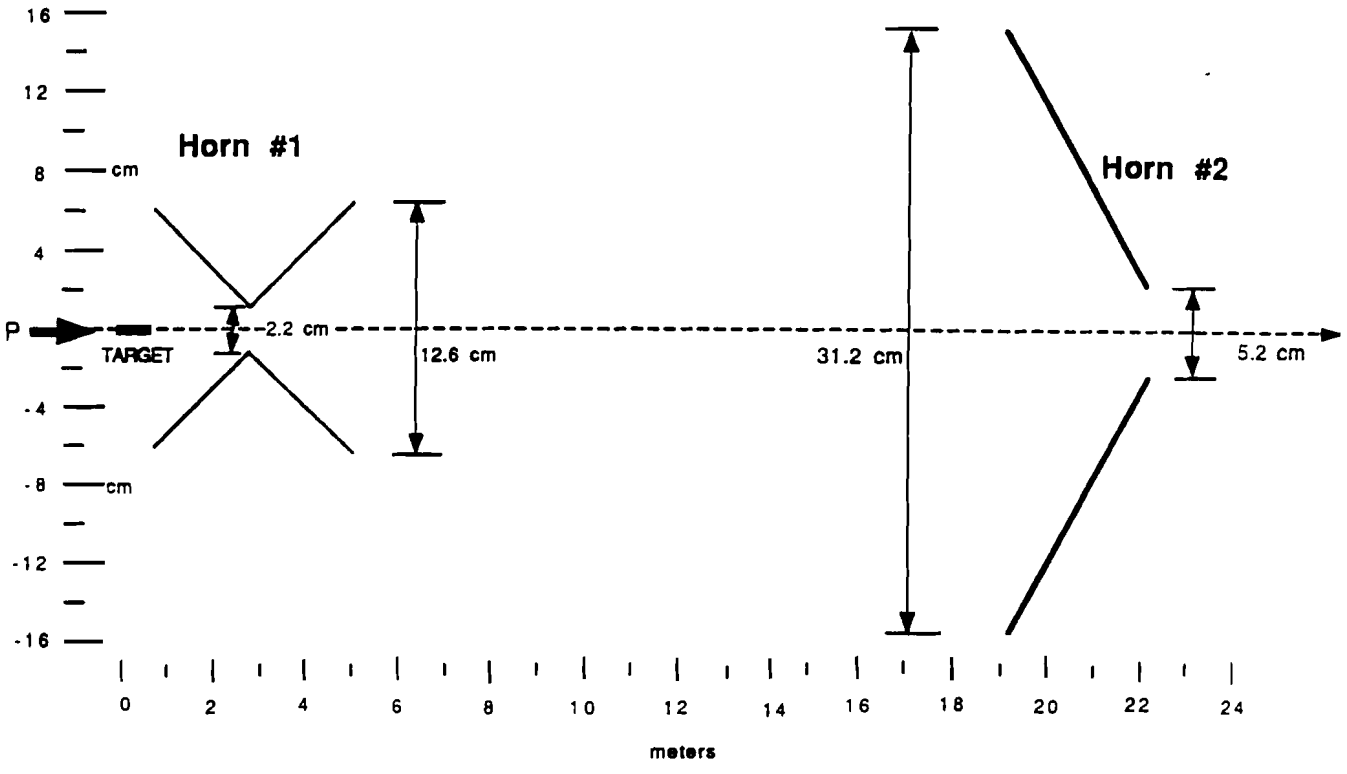

Figure 6.13: Schematic Drawing of the Double Horn System.

- Air, from the production target through the end of the second horn (≈ 30 m).
- Helium, from the second horn to the beginning of the 50 cm diameter steel collimator at ≈ 45 m.
- Vacuum, from the collimator to the dump (≈ 245 m.)

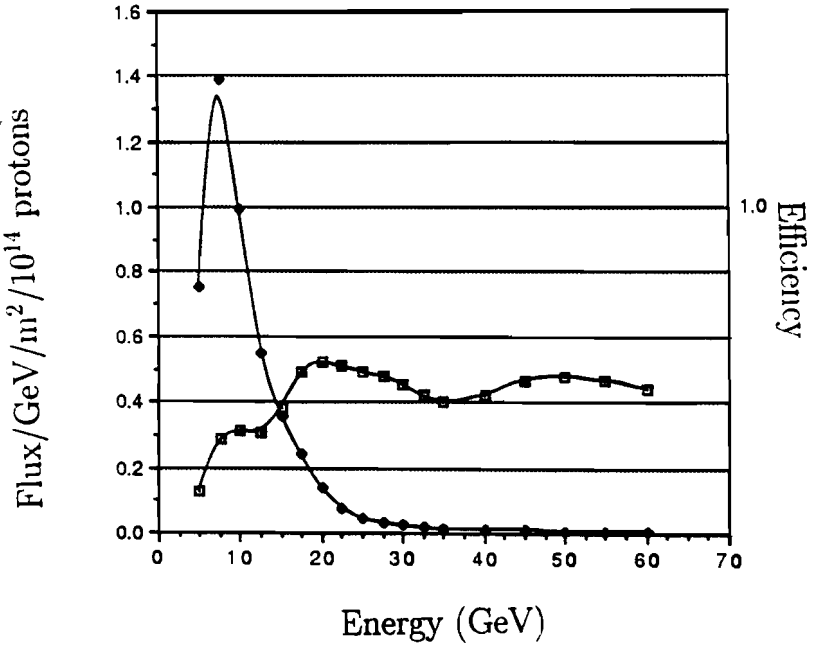

Figure 6.14: Flux of the two horn system at 170 kA (diamonds, peaked curve). Efficiency, equal to the flux ratio of the double horn to perfect focusing (squares, flatter curve)

6.5.1 The Inner and Outer Conductors

Secondary particle absorption losses in the horn material is considerable because the angle of the horn inner conductor is small relative to the particle trajectories it focuses. Making the wall thickness of the inner conductor as thin as possible is essential for keeping the flux high. At the same time making it too small will result in either (a) collapsing the conductor, shorting out the horn, or (b) pulling the conductor apart, causing an open circuit. A balance must be struck between the forces tending to pull and collapse the conductor with maximizing the flux. Since the magnetic pressure acting on the conductor walls is given by $P = B^2/2\mu_o$ the most severe stresses produced by a current pulse are at small radii at the horn neck.[14]

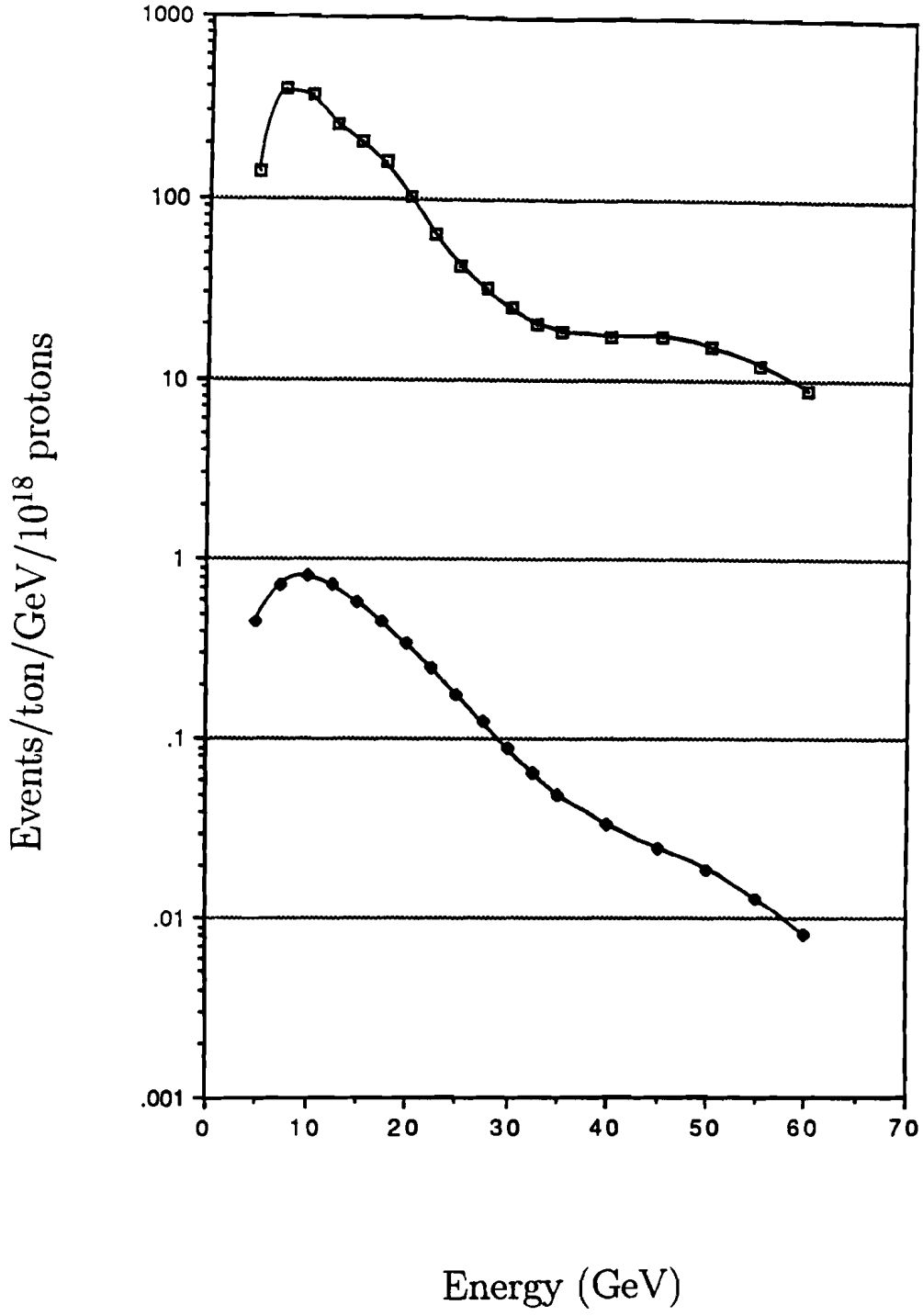

Figure 6.15: Event Rate and Wrong-Sign Background in Two-Horn System. The higher curve (squares) is the ν_μ signal and the lower (diamonds) is the $\bar{\nu}_\mu$ background.

In addition to absorption in the inner conductor, absorption will occur in the connecting flanges, if the conductor is made from short sections which are bolted together. Maintaining good electrical contact between the flanges and making them water tight also require special care. On the whole it is best if the inner conductor can be made of several pieces connected by flanges. Initial contact has been made with Le Fiell Manufacturing[1] for the "spin-method" of construction. Machining the conductors from a solid piece of aluminum is an alternative. Both need to be pursued. Support points between the inner and outer conductors of each horn will be needed along the axis, in order to prevent the inner conductor sagging due to its weight and to damp its transverse vibration modes. These supports are envisioned to be thin, rigidly attached to the outer conductor, and allow the inner conductor to float longitudinally. The outer conductor for Horn # 1 has a radius of 15 cm; Horn # 2 has 25 cm. The thickness of the outer conductor is not an issue with respect to absorption. The outer conductor is equipped with a system of external pipes by which LCW is sprayed onto the inner conductor. It also may be possible to use continuous forced convection to cool one or both of the horns. Such a system would be much simpler and would eliminate the need for water-tight joints between various conductors and insulators. At this juncture no work has been done on this option, but it is very attractive.

The wall thickness of inner conductors is adjusted so it can withstand the dynamic fatigue stress limit of 6061-T6 aluminum which is 10000 N/cm^2 @ 5×10^8 cycles.[2] This value is less than the static value by a factor of approximately 2.5. The distributions of axial (A), circumferential (T) and radial (R) stresses produced by a current pulse of 200 kA in the inner conductor have been calculated [14] and are shown in Fig 6.16. The resulting von Mises' stress distribution (M) is also shown in this Figure. The largest stress, at the neck, is still only about 60% of the fatigue limit. Prior to construction a full analysis of the stresses will be done with the finite element program ANSYS. The first approach to such analysis is already in progress at UCI applying a PATRAN program [15].

The axial force acts to fracture or pull apart the wall material. The inner conductor of the first horn is expected to stretch by about 0.6 mm due to a current of 200 kA. The radial force, smaller in magnitude, tends to deform the horn. In this sense, it is like a vacuum vessel where a thin walled tube buckles according to a rather definite pattern, depending on its relative dimensions and the conditions of restraint at its ends. Fig. 6.17 shows the most common forms assumed by tubes as they collapse. The "variable of strength" for this case is Young's Modulus, E. The smallest radii at the neck of the horns only require about 0.1 mm to support this force. Thus the wall thickness is determined primarily by the axial force in the narrow neck region, and by the energy of vibrations at the large radii. Fig. 6.18 shows the thickness profile for the horn inner conductors and Fig. 6.19 is an isometric view. Although the end flanges are shown as an integral part of the inner conductors, they will most likely be end plates welded onto the inner conductors. Because these regions are at points where the radius is large, the forces are much reduced over the neck region, making welding acceptable.

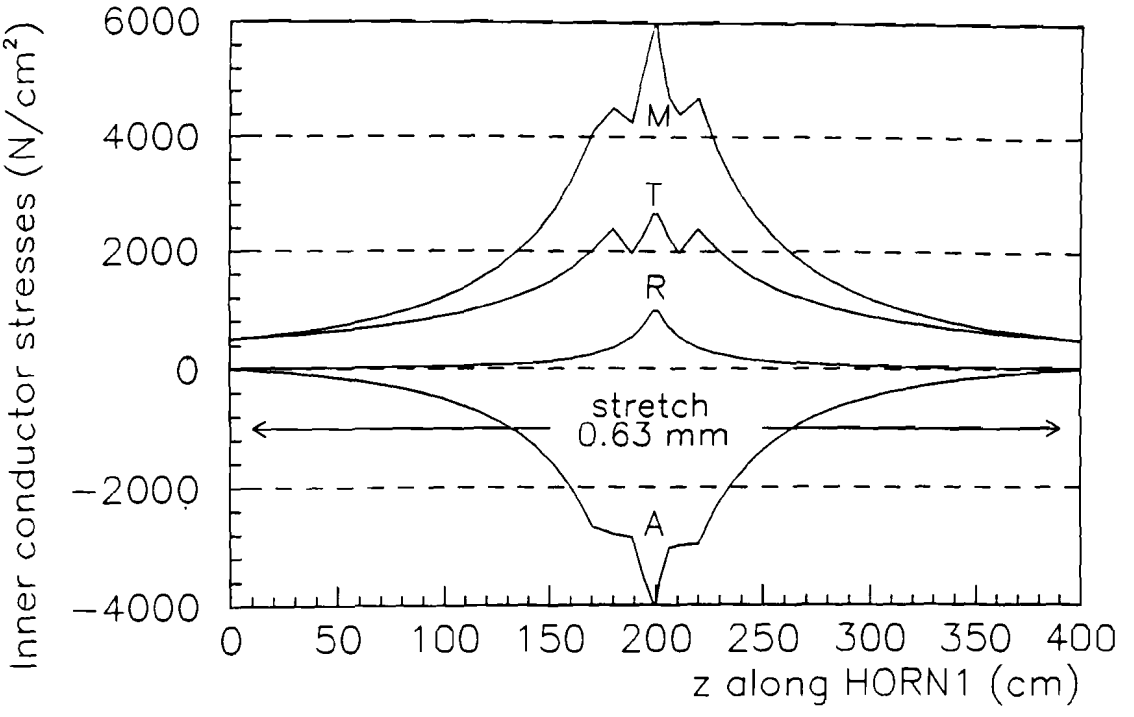

Figure 6.16: Distibutions of axial (A), circumferential (T), radial (R) and von Mises' stresses produced by a current pulse of 200 kA in the inner conductor of the Horn 1.

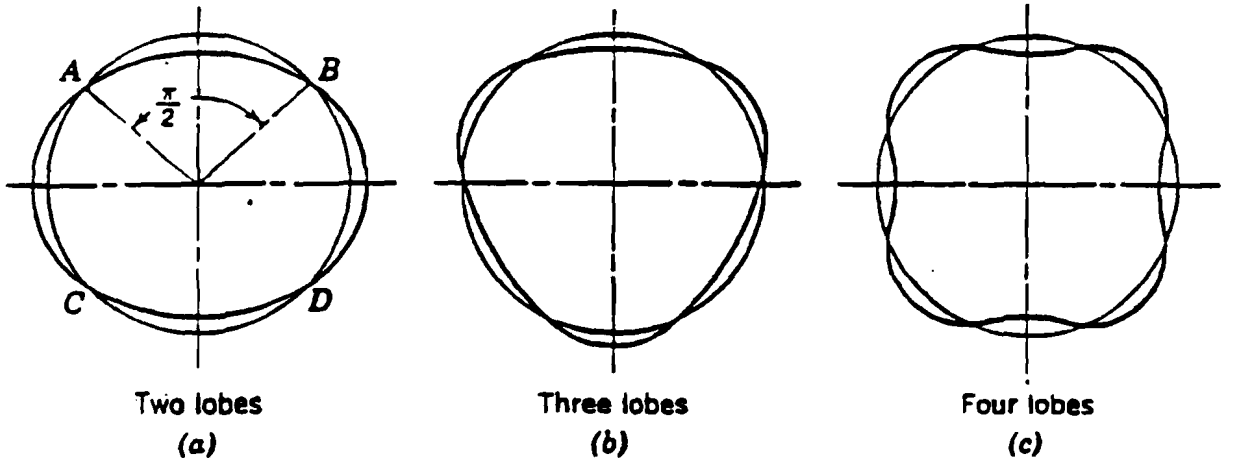

Figure 6.17: Forms of Collapse for a Horn, showing Buckling Configurations for Thin-walled Cylinders subject to Lateral Pressure Tending to Collapse the Horn.

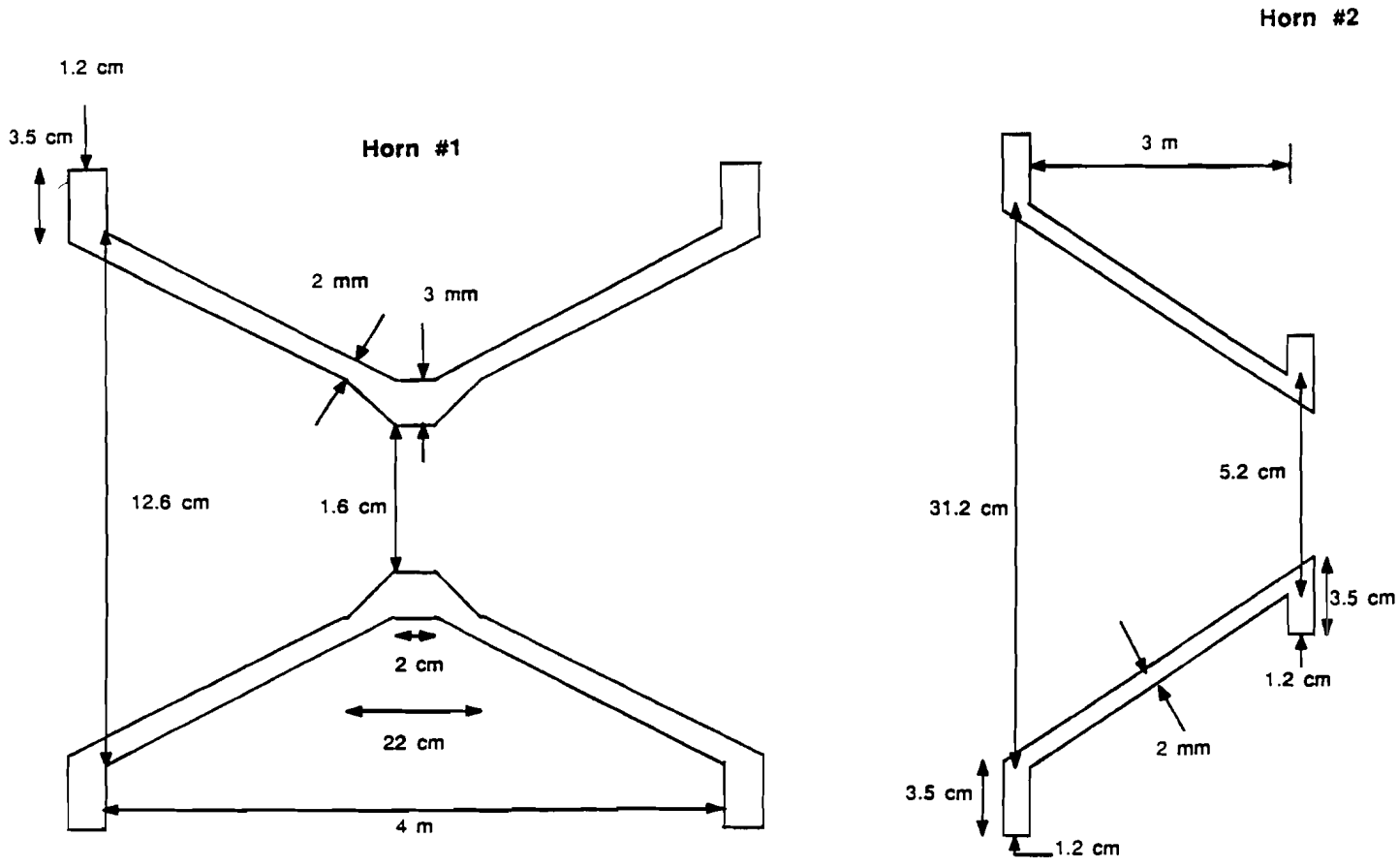

Figure 6.18: Thickness Requirements for the Horn Inner Conductors.

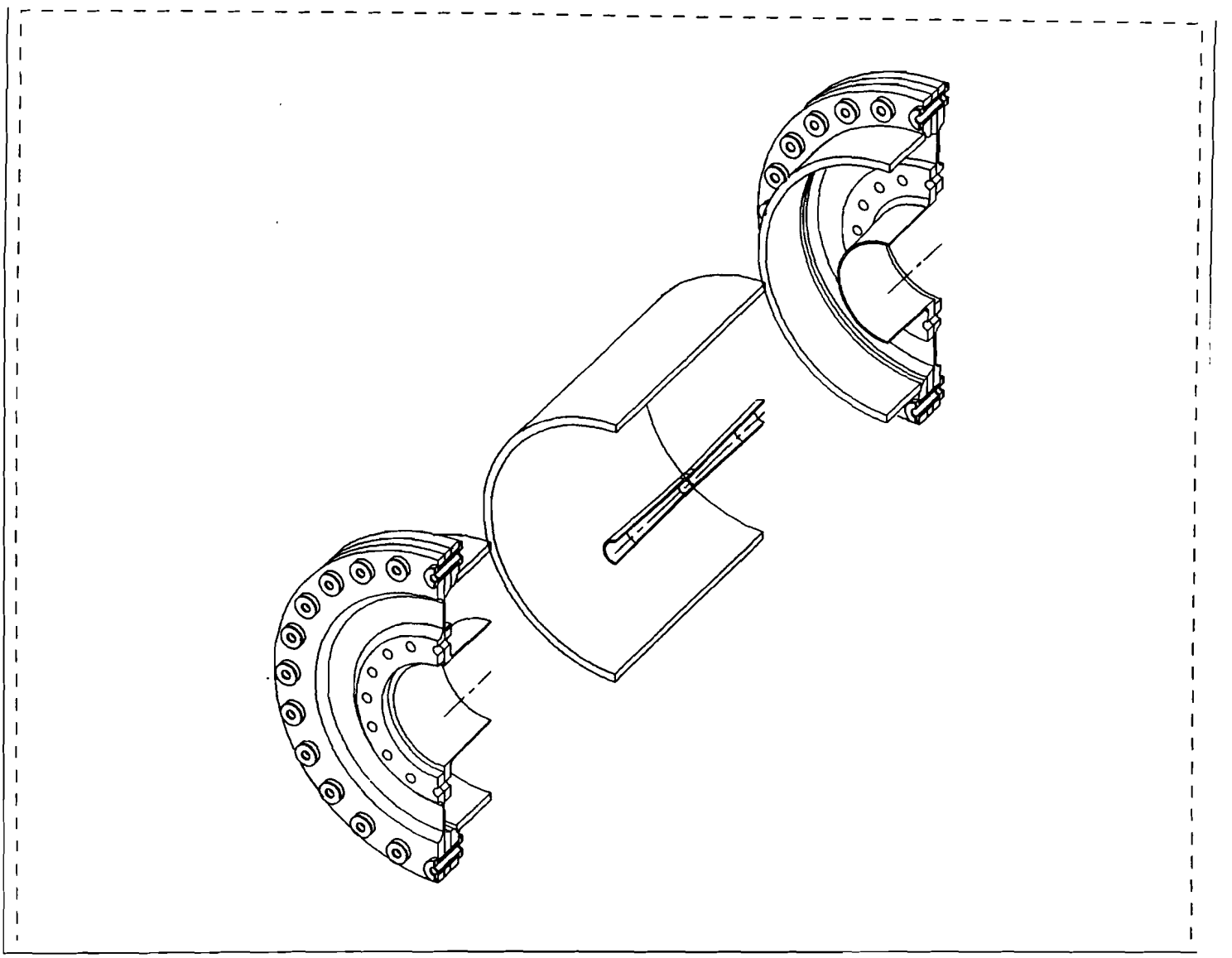

Figure 6.19: Isometric Cut-away of Horn # 1.

6.5.2 Electrical Considerations and Monitoring

The function of the Horn Power Supply System is to deliver a specified current to two series-connected magnetic focusing devices located just downstream from a 120 GeV high intensity primary proton beam target. The current will follow the shortest simplest path: (1) transformer to Horn # 1 inner conductor, (2) to Horn # 2 inner conductor, (3) to Horn # 2 outer conductor, (4) to Horn # 1 outer conductor, (5) back to the transformer. The magnetic fields generated focus the pions and kaons produced from the target into a parallel beam. Capability for reversing the current through the horns is designed in to provide both neutrino and anti-neutrino beams. In order to produce the required magnetic field (approximately 40 kg @ 200kA at the neck of the horn), a resonant capacitive discharge power supply system design utilizing a transformer is discussed.

This design meets the general specifications shown in Table 6.4.

Peak horn current	200,000 amperes
Total Transformed Load Inductance	2.8 mH
Total Transformed Load Resistance	0.98 Ω
Spill Length	1 ms
Current deviation (peak to peak) during spill	10%

Table 6.4: Requirements for the Horn.

Design Discussion

The general schematic form of the proposed design is shown in Fig. 6.20. The design proposal is for a resonant capacitive discharge system with a high current transformer for impedance matching the horns and strip transmission lines to the capacitor bank. The transformer provides significant benefits for systems requiring a long pulse: (1) all high voltage is confined to the primary circuit, (2) the primary circuit operates at comparatively low current, and (3) the high currents are confined to the secondary with a correspondingly lower voltage. Additionally, polarity reversal is enormously less difficult in the primary circuit. For the secondary, there are compelling arguments for a transformer in that the horn design is less demanding with low voltage; clearances can be smaller, the problems with water cooling are reduced, and the transmission lines can be simpler. The system calls for a 1500 μF capacitor bank consisting of three banks of five stacks each with six 16.6 μF capacitors per stack. Capacitors will be charged in parallel to a maximum of 20 kV by resonant charging. The switch device is expected to be a high voltage thyristor stack. A possible fallback from this

design will be two parallel ignitrons similar to the previously used NL-1040. A control system timing pulse will initiate the charge discharge cycle to meet the timing of the beam pulse. The timing differential between the capacitor charge and the triggering of the switch are to be set to minimize the time the bank sits at the peak voltage. The current and voltage waveform behavior will thereafter be determined by the circuit parameters. It is yet to be determined whether a clip switch or back diode will be required to eliminate the undershoot observed in the circuit simulations. Undershoot is undesirable in that adds to the heating load on the horns and transmission lines. Electronics must be designed to monitor a wide range of horn system parameters such as horn fields (dB/dt coils) and the transformer primary and secondary currents and voltages. The major effort here is to minimize fault damage if a failure occurs, so careful waveform analysis is critical. Fig. 6.20 shows the horn system circuit schematic with calculated and estimated component values in Table 6.5. *RXFORM* and *LXFORM* are the total transformer primary and reflected secondary resistances and inductances. For ease of analysis, each of the horns are assumed to have equal parameters though they in fact differ. Because of physical layout considerations, the second section of the stripline which goes between the horns is assumed to be four times longer than the first section which goes from the transformer to the first horn. Fig. 6.21 is a cross-sectional view of the preliminary stripline being considered. Aluminum is the material of choice for the parallel plate conductors. A parallel plate stripline is an inherently low inductance structure that can carry high currents with low losses. To contain the enormous forces generated during the current pulse, the plates will be bolted at appropriate intervals along the length. The insulation for this application will be ceramic sheets (for radiation resistance) placed along the length with provision for insulation overlap. Fortunately, the peak voltage in the transformer secondary circuit will not exceed 1000 volts; thus the insulation plan need not be unduly exotic.

Physical Layout

The Capacitor Bank, Charging Power Supply, Switch Tubes, Diagnostic electronics, and Controls are to be located in a low radiation air conditioned area remote from the transformer and horns. The capacitor bank and switch tubes are to be mounted in an interlocked area normally inaccessible to personnel. The connection between the capacitor bank and the transformer primary will be multiple (5) RG220 cables in parallel. While the layout of the horn power supply enclosure is relatively straightforward, the plan for the transformer, strip lines, and horns will require considerable engineering. This is because the very high radiation levels necessitate well-designed remote handling equipment for repair or replacement of this equipment.

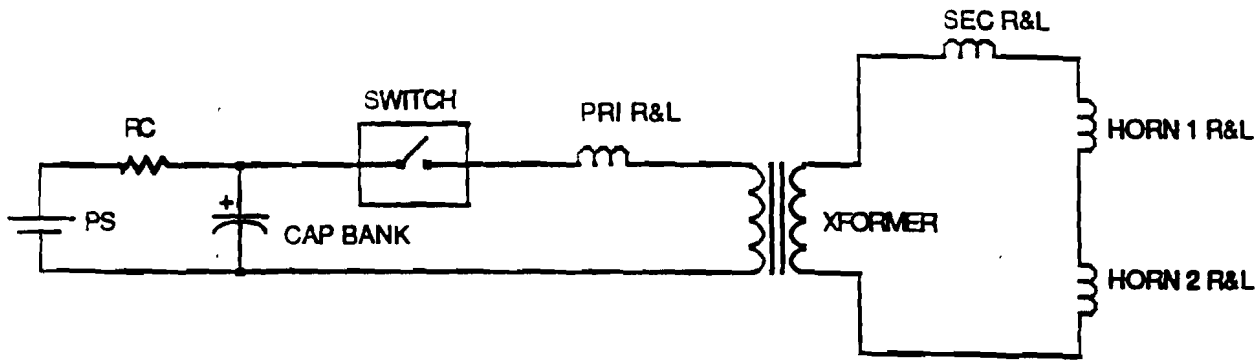

Figure 6.20: Electrical Schematic of the Horn.

Element	Value (Ω/Henry)
RCOAX	4.0×10^{-2}
LCOAX	1.0×10^{-5}
RXFORM	7.5×10^{-2}
LXFORM	5.0×10^{-4}
Primary R	1.0×10^{-4}
Primary L	3.0×10^{-7}
R(Horn 1)	5.0×10^{-4}
L(Horn 1)	1.5×10^{-6}
Secondary R	4.0×10^{-4}
Secondary L	6.0×10^{-7}
R(Horn 2)	5.0×10^{-4}
L(Horn 2)	1.5×10^{-6}

Table 6.5: Values for Electrical Elements of the Horns.

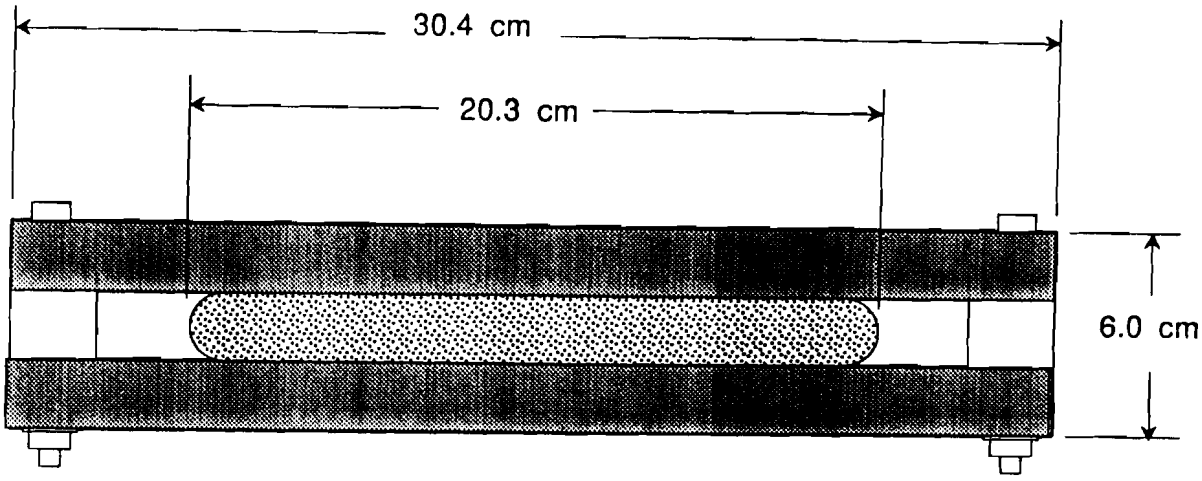

Nominal 1.6 cm Ceramic Insulation Full Length (not shown)

Figure 6.21: The Horn Stripline.

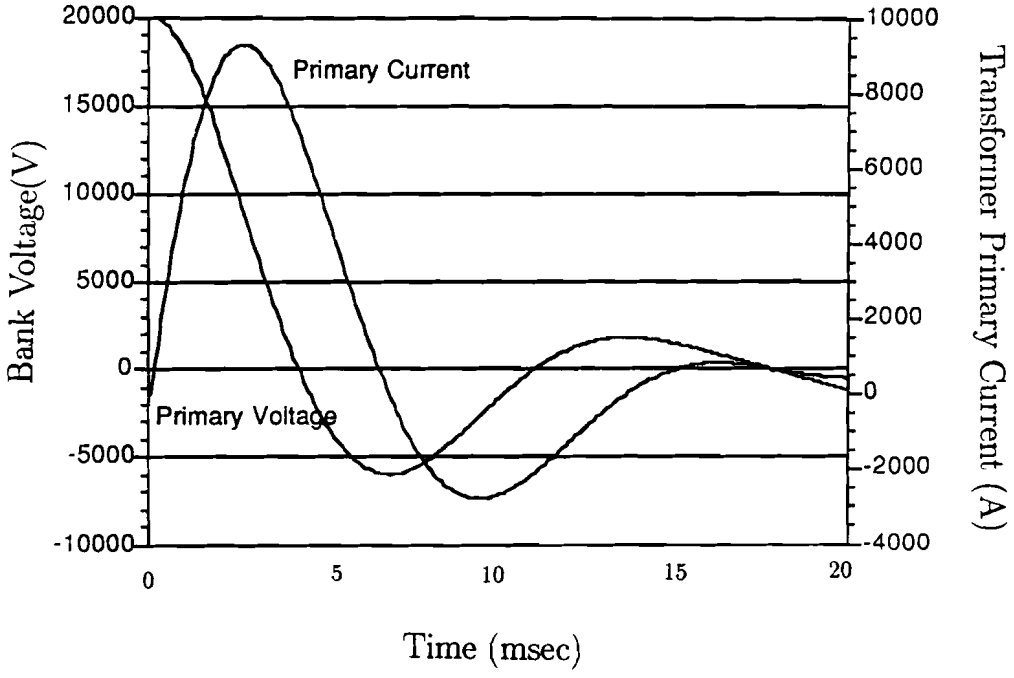

Figure 6.22: Primary Waveform for the Horn.

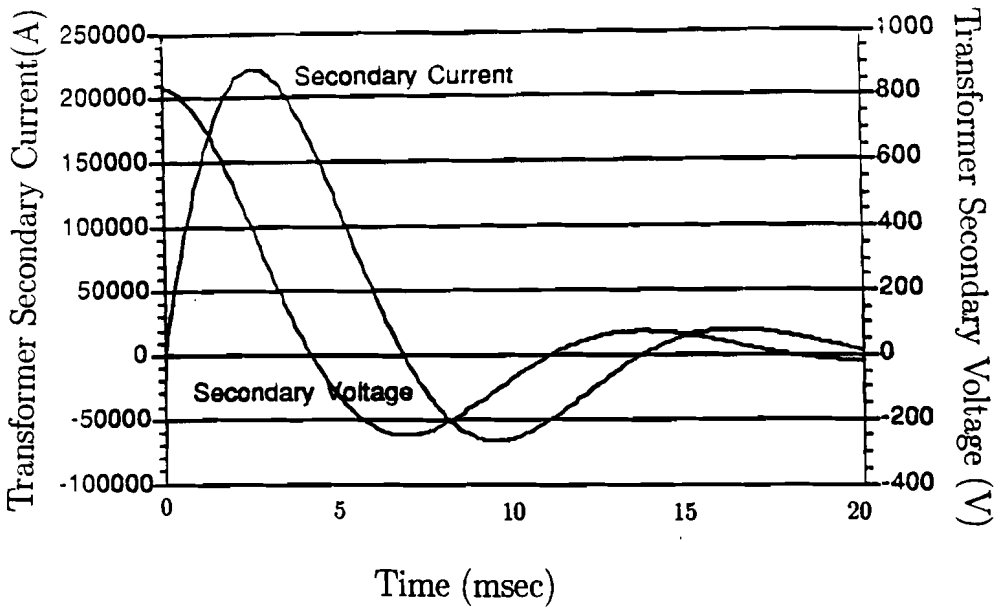

Figure 6.23: Secondary Waveform for the Horn.

6.5.3 Radiation Handling and Shielding

The transport system for the target and two horns is envisioned to be bedplates moving and resting on a rail system as shown in Fig. 6.24. The bedplates will not be lubricated, but will have brass bearings and will remain in the target tube throughout the run. To account for initial movement of the target hall and steel surrounding it, provision will be made to realign the rail system after "settling" has occurred.

Before making this "fine" adjustment, a coarse alignment must be made. If the entire steel cross-section "settles" by more than 1 foot, the horns as presently designed will not be able to lie along the decay axis. The present trainload can accommodate as much as 1 foot of settling if the steel is set 6 in. high during construction since the trainload could then be internally adjusted to make up the difference between the final settled position and the ideal position: the distance between the bottom of the horns and the top of the bedplate can be raised or lowered by 6 in.

Final alignment adjustments for the first horn will be accomplished by a system of jacks and right angle drives actuated by cranks situated upstream of the target tube. Adjustments for the second horn will be accomplished in a similar way except the cranks will protrude out the downstream end of the target tube. Because the weight of each of the elements is relatively small, the bedplates can be made of aluminum. This also alleviates the force that arises when the current flowing in the stripline interacts with the induced magnetic field of the steel bedplate. To maximize the shielding around the elements, they will be placed inside a square target tube of 100 cm on a side. There will be two trainloads: one for the horns and stripline between them and another for the target/convection system/shielding.

In that way, work associated with the target can be done without disturbing the horns and their alignment. Because the stripline will rigidly connect Horn # 1 with Horn # 2, both will have to be pulled out to work on either of them or the stripline. In order to close off the target tube from the rest of the enclosure, a backscatter shield will be placed at the upstream end at the mouth of the target tube.

Because of the very high residual radiation levels expected, it is possible to make only minor repairs. In addition, all electrical insulation will be machinable ceramic with a radiation resistance of 3×10^{10} rads.[22]. If a failure occurs, the entire component will be replaced; this will be necessary in the event of a cooling water leak as well, since the electrical circuit will certainly be compromised. This means in the initial construction, duplicates will be made of each horn, the stripline and the transformer.

The horn trainload, consisting of six bedplates of 12 feet each will be modularized into manageable pieces. The disposal of the horn and supporting bedplate, or any subsection will be accomplished by inserting it into a steel container of 3 feet by 3 feet by 15 feet. The steel container will have a wall thickness of 4 inches and the lid will fit into a self-aligning beveled top. It will also serve as the on-site transport, being pulled out of the enclosure with a crane and loaded unto a flatbed truck.

Disconnecting the horn train into smaller sections as well as disconnecting it from the transformer has not been worked out.

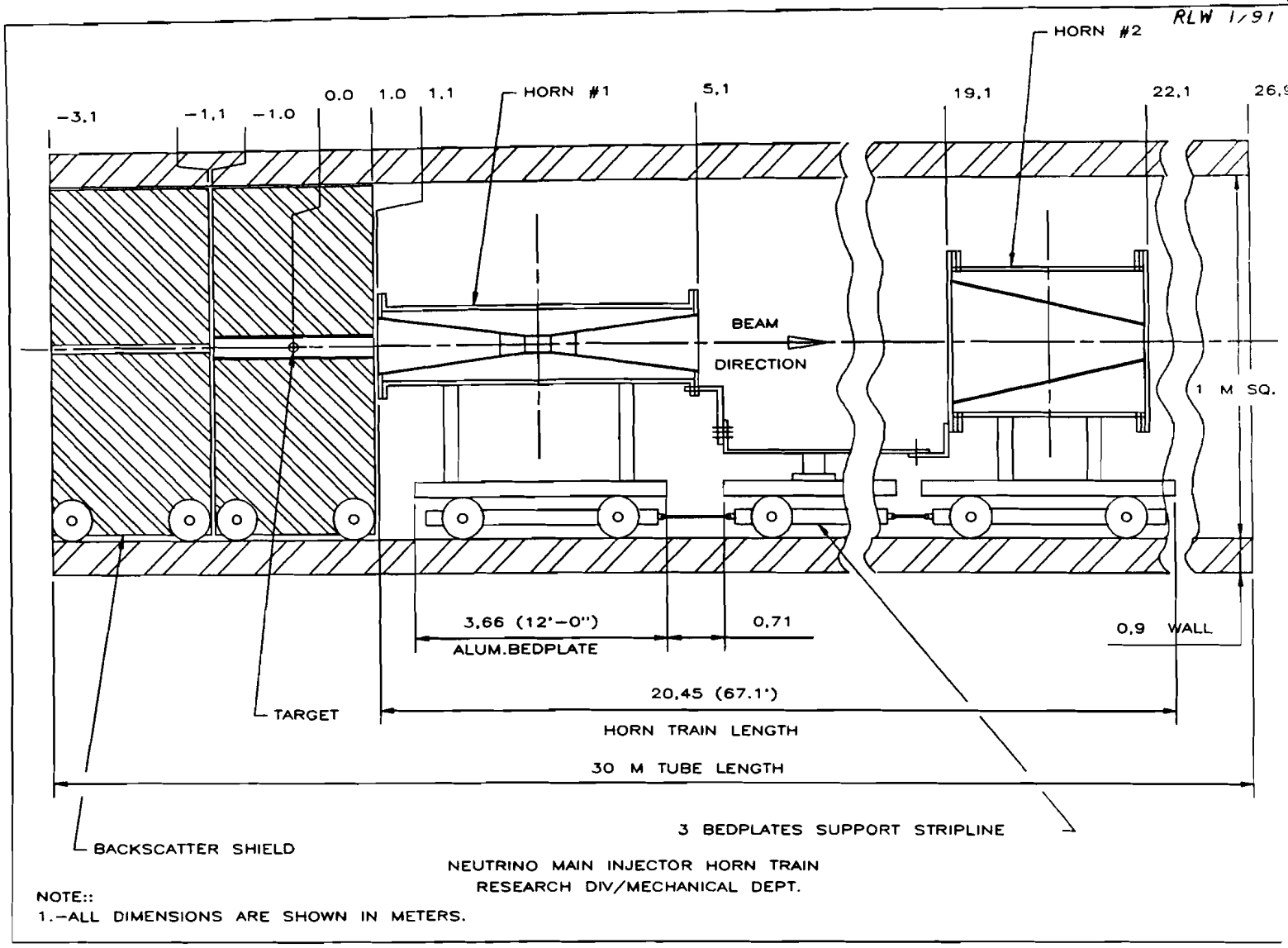

Figure 6.24: Schematic of the Bedplates carrying the backscatter shield and horns inside the 1 meter $\times$ 1 meter iron target tube.

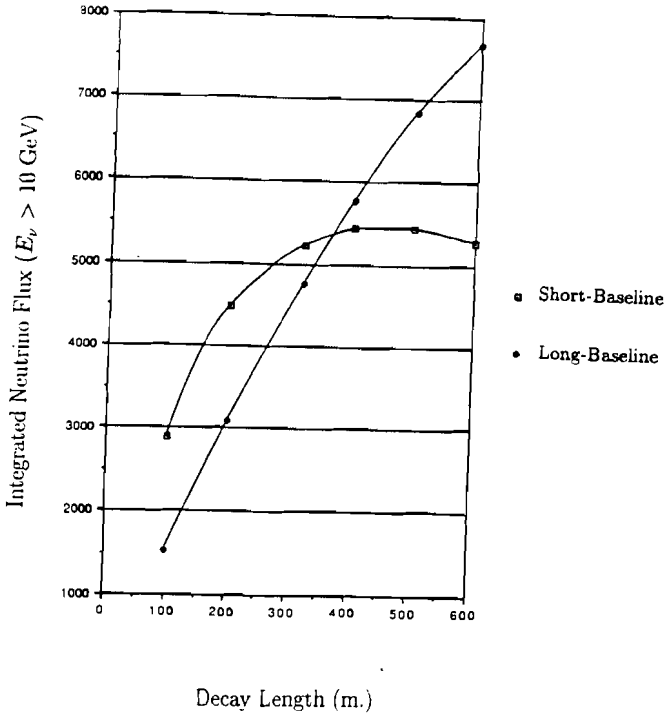

Figure 6.25: Event Rate for Long and Short-Baseline Experiments as a function of the length of the decay volume. Diamonds refer to the long-baseline experiment; squares, to the short-baseline. The scale is arbitrary.

6.6 Decay Region and Beam Dump

The length of the decay pipe was chosen to be 320 meters. This represents a compromise between the short-baseline and long-baseline experiments. The relationship between neutrino flux and decay length is shown in Fig. 6.25. As the decay length is varied, the first half (excluding the region of the train) has a 1 meter diameter. The second half of its length has a diameter of 1.5 meters. One can see that there are no gains beyond 320 meters for a short-baseline experiment, while the gains are almost linear for a long-baseline. Since construction costs increase with the length of the underground pipe, we have chosen 320 meters as a compromise.

The diameter of the decay pipe is determined primarily by cost. NUADA shows an increase of only 5% in going from a diameter of 1 meter to 1.5 meters. It also shows the integrated flux to be the same for 1.5 and 2 meters. Because of some amount of "settling" will occur after construction, we have chosen to use a diameter of 1 meter for the first half and 1.5 meters for the second half of the decay volume.

A beam dump is located at the end of the decay region to absorb those pions and kaons which have not decayed as well as the diffracted and non-interacting protons. Because the

dump is far downstream of the target, the natural divergence of the proton beam means a large spot size on the dump. This in turn translates into a small local energy deposition in the aluminum core. The beam dump will consist of two modules of 8 feet each. The first has a water-cooled aluminum core about 24 inches by 24 inches by 8 feet, surrounded by steel with outside dimensions 10 feet by 10 feet. The second is the same as the first, except that the water-cooled aluminum is replaced by water-cooled copper. The distribution of beam power for an intensity of 3×10^{13} and 1.5 second cycle time is shown in Fig. 6.26 (we recall that power and heating levels were calculated at 1.5 sec to allow a safety margin).

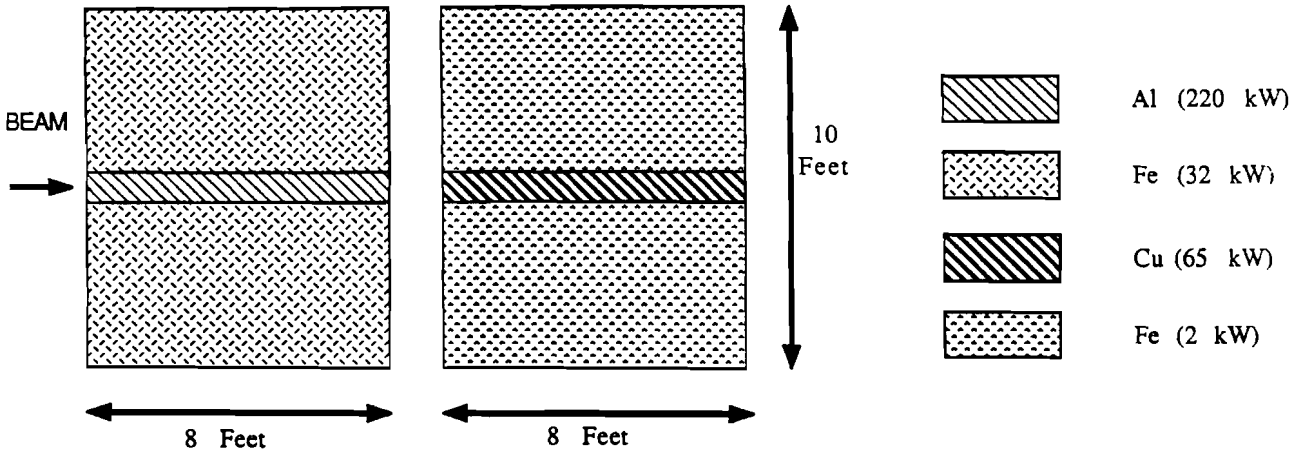

Figure 6.26: The heat distribution of various mechanical sections of the Beam Dump.

6.7 Calculation of the Beam Neutrino Output

The neutrino output of the wide band beam line discussed so far has been calculated employing a Monte Carlo technique by several groups, each interested in slightly different aspects of the beam characteristics. All these calculations were based on two models for production of secondaries in 120 Gev proton interactions with the target nuclei:

1. a model which has been used over a decade in the NUADA program fitted to the most accurate data for interactions of 400 GeV protons with beryllium nuclei [18],
2. a new model, based on fits to inclusive cross sections measured by the SAS spectrometer at FNAL for p + p at 100 and 175 GeV [19] and for p + A (A being C, Al, Cu, Ag or

Pb) at 100 GeV [20] interactions.[21]

While the final neutrino outputs resulting from these two models agree within 10-15%, evident differences between them cannot be resolved because there is no data for p + C 120 GeV interactions.

The existing beam Monte Carlo programs then follow particles through the horn focusing system and the decay tunnel and collect information about the resulting neutrinos. One of these programs, developed by the IMB group uses the GEANT package for following particles in matter, which allows them also to take account of interactions in the material along the beam line such as the air, horn conductors, or decay pipe window. These interactions can diminish the final neutrino flux by as much as 30% if the horn conductor thicknesses are not correctly optimized.

The results of calculations show, that at the distance of the short baseline detector P-803 neutrinos of different flavors have energy spectra integrated over the detector acceptance such as in Fig. 6.27. The rate of CC interactions other then muon neutrinos in this detector is expected to be 0.6% for $\bar{\nu}_\mu$, 0.8% for ν_e and 0.04% for $\bar{\nu}_e$.

The ν_μ flux on the beam axis at the distance of the IMB detector (570 km) is expected to be $10^4/m^2/10^{13}$ protons. The variation of the flux and the mean neutrino energies with an angle from the beam axis, an important characteristics for the Long Baseline experiments, are shown in Fig. 6.28. Note the smaller slope of these variations for angles below 0.5 mrad. This feature of the beam puts less demanding requirements for the accuracy with which the beam has to be aimed toward the Long Baseline detectors.

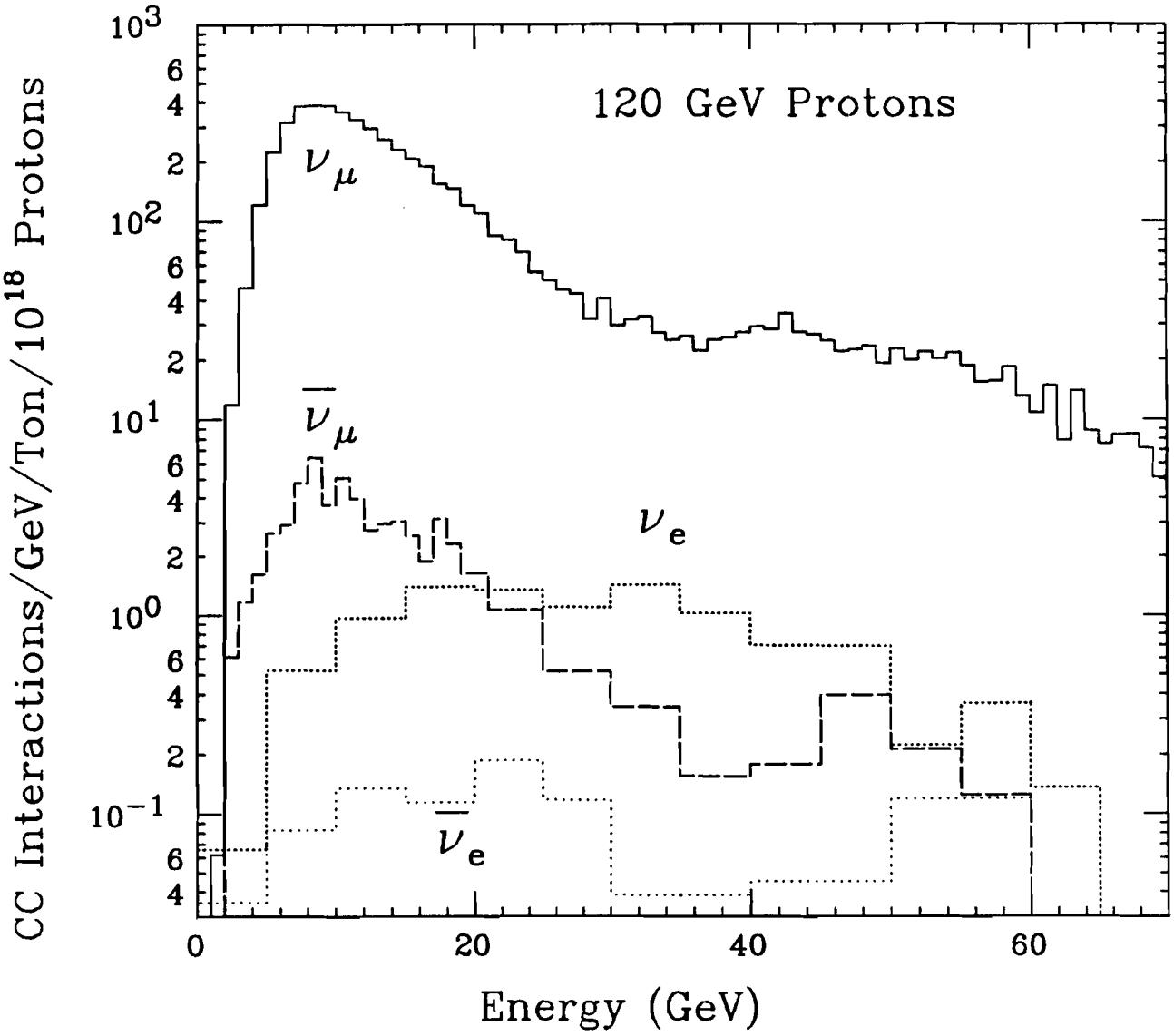

Figure 6.27: Results from a Monte Carlo simulation of the charged-current event rates for ν_μ and ν_e and for background $\bar{\nu}_\mu$ and $\bar{\nu}_e$ at the P–803 detector. The calculation assumes the target, horn, and beamline discussed in this Report and a 120 GeV proton beam with the horn set to focus positively-charged particles.

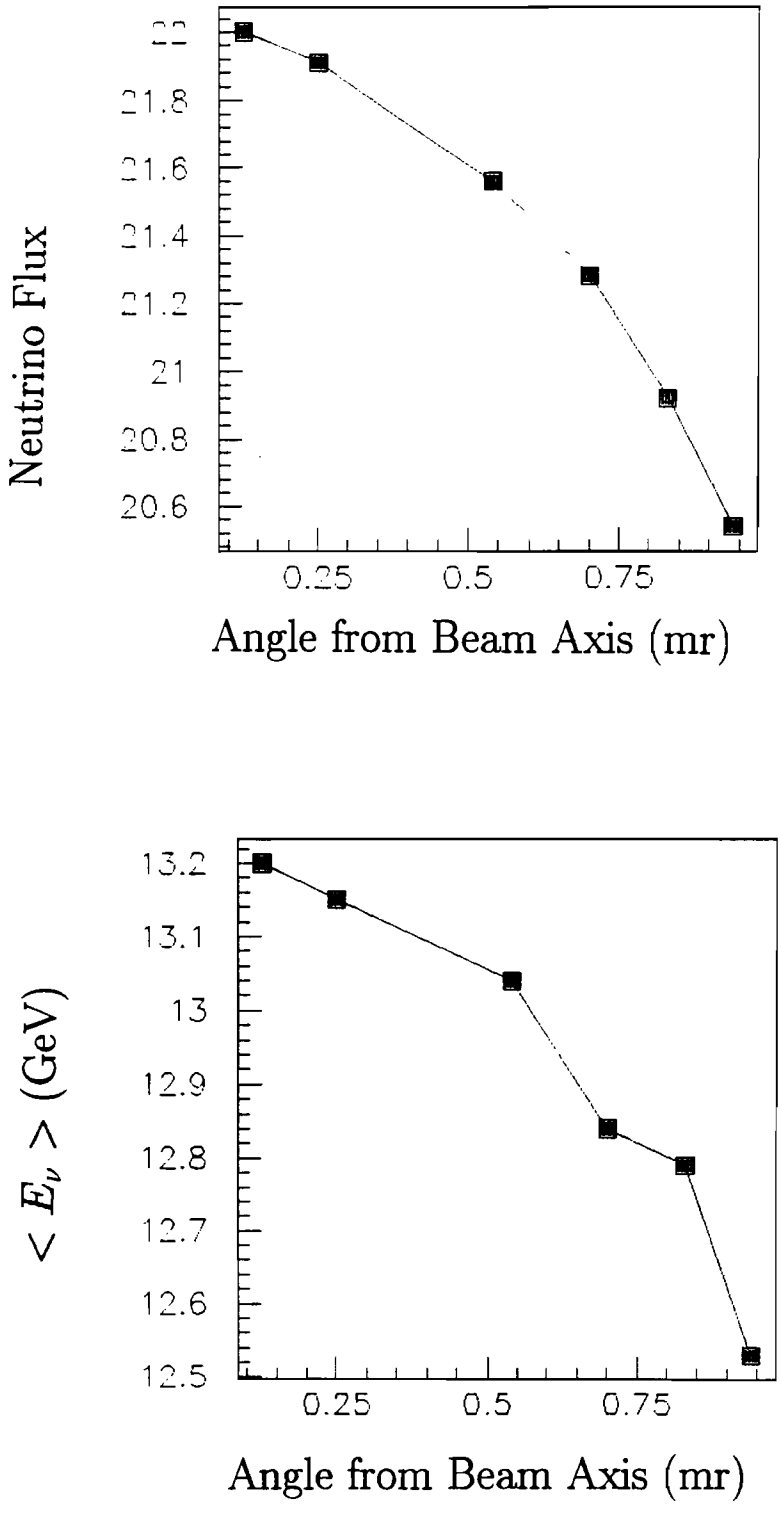

Figure 6.28: Variations of flux and the mean energy of neutrinos with angle from the beam axis.

References

[1] LeFiell Manufacturing, 13700-T Firestone Blvd. Santa Fe Springs, California 90670.

[2] Metals Handbook 9th Edition. (1979), Vol. 2, Properties and Selection: Non-Ferrous Alloys and Pure Metals, p. 61.

[3] POCO Graphite, 1601 South State Street, Decatur, TX 76234.

[4] W. Gajewski UCI Tech. Note 13/90 (1990).

[5] A. Malensek. Private communication.

[6] R. Svoboda LSU-HEPA 3-90 (1990).

[7] W. Gajewski UCI Tech. Note 1/91 (1991).

[8] A. Malensek. Private communication.

[9] These arguments follow closely the prescription from the Technical Note CERN LABII/BT/74-1 by W. Kalbreier et al, "External Targets at the SPS".

[10] S.P. Timoshenko and J.N. Goodier "Theory of Elasticity", McGraw-Hill Book Co., 3^{rd} Ed., (1970), eqs. 249, 250 and 253.

[11] N. Stanton. Private communication.

[12] Fermilab Upgrade: Main Injector, Conceptual Design Report, January 1989, p 4.

[13] R. Bellone, A. Ijspeert, and P. Sievers, CERN 86/ST//TE/A/113, "Targets for High-Intensity Beams at CERN: Design, Operational Experience, and Developments," June, 1986.

[14] W. Gajewski UCI Tech. Note 2/91 (1991).

[15] PATRAN by PDA Engineering, Costa Mesa, CA. copyright 1989.

[16] (Advanced Continuous Simulation Language), Mitchell and Gauthier Associates, copyright 1986, Concord, Mass.

[17] As a guide we have followed the arguments in the technical note CERN 72-11/Lab I by J.C. Dusseux, J.B.M. Pattison and G. Ziebarth, "The CERN Magnetic Horn (1971) and its Remote-Handling System".

[18] H.W. Atherton *et al.*, Precise Measurements of Particle Production by 400 GeV/c Protons on Beryllium Targets, CERN-80-07.

[19] A.E. Brenner *et al.*, Phys Rev D 26,1497,(1982).

[20] D.S. Barton *et al.*, Phys Rev D 27,2580,(1983).

[21] Proposal P-805.

[22] Mykroy/Mycalex Ceramics, 125 Clifton Boulevard, Clifton, New Jersey 07011.

Part III

Civil Construction

7 Safety Issues for Main Injector Beams

7.1 Radiation Safety

There are several radiation safety concerns associated with the proposed neutrino beamlines of the Main Injector Project. They are no different in kind from those found in the existing Fermilab fixed target program, although some of these concerns are heightened by the higher beam intensities and repetition rates of the Main Injector Beam. These concerns are:

- shielding of prompt radiation (both neutrons and muons)
- activation of target and beamline components
- activation of soil and air
- concentrations of radioactivity produced in groundwater

The necessary shielding dimensions have been specified based on results from the Monte Carlo code CASIM.[1] CASIM allows one to model arbitrary beamline geometries and associated shielding geometries composed of several different materials and/or regions. Magnetic fields may also be included. The results of a CASIM calculation are the distribution of inelastic interactions per incident particle within the specified geometrical limits as well as total inelastic interactions per particle within each material and/or region. Using well-established conversion factors, the CASIM results may be converted into dose rates at the surface of bulk shielding or into levels of activation. When coupled with models describing the transport of radioactivity,[2] the results also may be used to estimate concentrations of radioactivity generated in groundwater. A separate version of CASIM can be used to calculate the muon fluence.

Beam Energy	120 GeV
Beam Intensity	3×10^{13}per pulse, 1×10^{20} per year
Repetition rate	1900 pulses per hour
Target	1.1 meter long graphite

Table 7.1: Beam and target parameters relevant to double horn beam radiation shielding requirements.

There are a few additional facts that are important to keep in mind when considering necessary shielding dimensions.

- For typical targeting or beam loss situations the star density, and therefore the prompt radiation dose rate due to neutrons at the surface of a shield, decreases by about a factor of ten for each three feet of soil or one foot of steel that is added transverse to the beam.
- The prompt dose rates and the levels of residual activation are proportional to the incident beam intensity per pulse and the repetition rate, and are approximately proportional to the incident beam energy.

7.2 Radiation Safety in the 120 GeV Beam

7.2.1 120 GeV Double Horn Beam Shielding Requirements

The beam and target parameters that determine the shielding requirements for a downward slanted (45 mrad) 120 GeV double horn beam are listed in Table 7.1.

A cylindrically symmetric shielding design that satisfies the requirements for prompt radiation and residual activation of soil and groundwater for the slanted beam is shown in Figure 7.1. The target and horn are contained within a target tube 100 cm in diameter. The shield around the target/horn region is composed of two parts:

1. a steel region 90 cm thick radially and 30 meters in length that contains about 89% of the total stars produced per incident proton. The shielding is located within a concrete enclosure having walls approximately 45 cm thick.

2. a region of soil about 465 cm thick and extending over the first 80 meters of the target tube and decay pipe that is protected by an impermeable barrier to prevent the transport of radionuclides.

There is a steel "backstop" beginning 73 meters from the target which is 280 cm. in diameter, 7 meters in length, with a 50 cm diameter hole. It is designed to reduce the star density in the soil surrounding the downstream decay pipe. This decay pipe increases in diameter from 1 meter to 1.5 meters at a distance of 160 meters from the target in order to reduce the number of secondary particles emerging from the hole in the backstop that could strike the soil. In addition, the decay pipe downstream of the "backstop" is surrounded for its entire length by soil contained within an impermeable barrier 975 cm in diameter. The decay pipe terminates in a beam dump sufficient to absorb the full beam intensity.

7.2.2 Dose Rates Due to Prompt Neutron Radiation

Normal Running

The necessary transverse shield thickness is determined by the desired dose rate at the surface of the shield. The Fermilab Radiation Guide requires that the dose rate due to normal operations be less than 2.5 mrem per hour for unfenced outdoor areas that are minimally occupied.[3]

CASIM calculations for the shielding geometry illustrated in Figure 7.1 have a maximum star density in the region outside the target tube steel shielding that is about 4.1×10^{-14} stars/cm^3/proton at a radius of 510 cm. This corresponds to a dose rate of 23 mrem per hour using the beam intensity and repetition rates in Table 7.1 and the standard conversion factor of 10^{-2} mrem per star/cm^3. To reduce this to 2.5 mrem per hour requires an attenuation factor of 0.11. This can be obtained by an additional 88 cm of earth shielding. Therefore, the earth shielding required in this region must extend to a radial distance of at least 598 cm (19.6 ft) from the beam axis. Equating 1 foot of steel to 3 feet of earth implies that 728 cm (23.9 feet) of earth-equivalent overburden is needed over the target tube.

In the region immediately downstream of the target tube steel shielding but upstream of the steel backstop, the maximum star density is about 1.4×10^{-13} stars/cm^3/proton at the same radial distance of 510 cm giving a dose rate of 80 mrem/hr at this point. To reduce this to 2.5 mrem per hour requires an additional 137 cm of earth cover. Therefore, the earth shielding must extend out to a distance of at least 647 cm (21.2 ft) from the beam axis in this region. Note that the inner diameter of the enclosure has been reduced to 200 cm in this region. This results in 547 cm (17.9 feet) of earth-equivalent shielding here.

The maximum star density adjacent to the steel backstop is about 1.75×10^{-13} at a radial

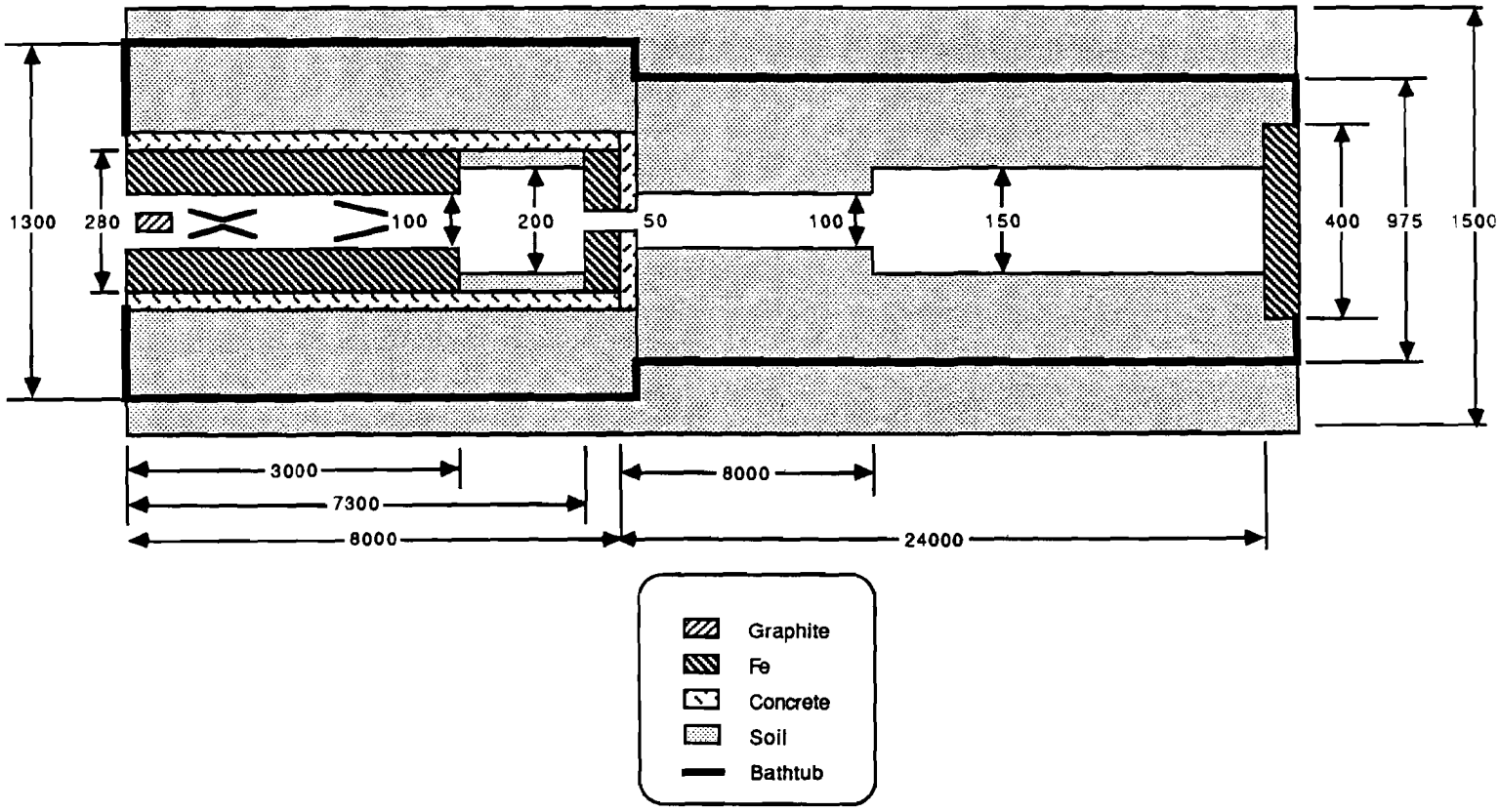

Figure 7.1: Radiation Protection System for the 120 GeV Slant Beam. The Figure is not to scale; all units are in cm.

distance of 510 cm, resulting in a dose of 100 mrem per hour. To reduce this to 2.5 mrem per hour requires an additional 146 cm of earth. This means that the earth overburden must extend out to at least 656 cm from the beam centerline in the backstop region. Including the steel, there is a total of 861 cm (28.2 ft) of earth-equivalent shielding surrounding the backstop.

Star densities downstream of the backstop are largest in the region of the decay pipe beyond 240 meters from the target since there is a line of sight back to the target beyond this point. The maximum star density is about 1.6×10^{-14} stars/cm^3/proton resulting in a dose rate of 9.1 mrem per hour at a radius of 510 cm. To reduce this to 2.5 mrem requires an additional 52 cm of soil. Therefore, the earth overburden must extend to a distance of 562 cm from the beam centerline. The total earth-equivalent shielding required in the design is about 487 cm (16.0 feet), based on a decay pipe diameter of 150 cm in this region.

Accident Conditions in Minimally Occupied Areas

The dose rate due to accident conditions for unfenced, minimally occupied outdoor areas is required to be less than 10 mrem per hour if interlocked radiation detectors are not used.[3] We list them below:

Pre-Target Enclosure The pre-target enclosure will contain magnets and other devices that could be struck by the beam if it is mis-steered. In the absence of interlocked radiation detectors a full intensity beam loss for one hour on the upstream face of a 10 foot long EPB type dipole was assumed as the accident condition. For calculational purposes, the magnet was assumed to be housed in a 2 meter diameter tunnel, surrounded by a one foot thick concrete wall and soil. A CASIM calculation using that geometry indicated that 756 cm (24.8') of earth-equivalent shielding, including the 1 foot thick concrete wall, was necessary to reduce the accident dose rate to the 10 mrem per hour guideline.

Target Tube Region The accident condition is not the determining factor on the amount of shielding required for the target area since the shielding is already designed to accept the full Main Injector Intensity for normal running. The"accident" condition is no worse than normal running for the target area.

Decay Pipe Region The 7 meter thick steel backstop acts as a fixed collimator to prevent beam that has been mis-steered in the pre-target hall from striking the soil surrounding the downstream decay pipe. The beam will either strike the backstop or strike the face of the beam dump steel shielding at the end of the decay pipe. In either of these two cases sufficient earth shielding will be present to reduce the accident dose rate to less than 10 mrem per hour. The minimum amount necessary for the backstop will be estimated by modeling a scraping loss on the inner surface of the backstop. The beam

dump at the end of the decay pipe will have more than adequate shielding since the slanted beam line will force it to be about 70 feet below the surface.

7.2.3 Ground Water Activation from the 120 GeV Beams

The US Environmental Protection Agency has established radiation dose limits that restrict the annual dose received from drinking water to less than 4 mrem. This limit leads to limits on the concentrations of various radionuclides in the groundwater.[4] The accelerator-produced isotopes of principal concern are ^{3}H and ^{22}Na.

The EPA concentration limits are based on only one isotope being present in the ground water. That is, if a typical individual drank water containing a single radioisotope with a concentration equal to the EPA limit for one year, they would receive a dose of 4 mrem. If more than one isotope is present then the properly weighted sum of the concentrations must not result in an annual dose of more than 4 mrem to someone who used that as their sole source of drinking water.

The concentration limits and other relevant factors for ^{3}H and ^{22}Na are given in Table 7.2.

	^{3}H	^{22}Na
Mean lifetimes (years)	17.7	3.74
Migration rate (ft per year)	7.5	3.2
Allowed concentrations (pCi per ml)	20	0.2
Leachable atoms per star	0.075	0.003

Table 7.2: Radionuclide parameters for use in groundwater activation calculations.

We use a model previously employed at Fermilab to estimate ground water concentrations.[2] The total amount of leachable radioactivity of each isotope produced outside impermeable barriers surrounding the target tube and decay pipe is estimated based on results from CASIM, and soil studies done on their leachability. In the most general case, the activities produced in one year of running are assumed to be transferred downward to the aquifer at fixed rates and allowed to radioactively decay *en route*. The amount of activity for each isotope that remains at the elevation of the aquifer is then conservatively assumed to be diluted by an amount of water equal to that used by a single individual in one year (40 gallons per day, 365 days per year) to arrive at estimated concentrations.

For the slant beam ground water protection design, no credit for radioactive decay has been taken. This is because the slanted beam construction can potentially result in an easy pathway to the aquifer for radioactivity produced in unprotected soil.

The extended nature of the neutrino decay pipe makes it uneconomical to use only steel shielding, as is often done in other types of fixed target experiments. Instead, a combination of steel shielding surrounding the highest loss points and impermeable barriers encasing regions of soil will be used. With this design it proved possible to arrive at a design that contains 89% of the total radioactivity in steel shielding. Essentially all of the remaining activity is contained within soil regions protected by the impermeable barriers. Less than 0.02% of the total activity is produced outside the protected region.

The results of the groundwater activation estimates can be expressed as a sum of ratios to the EPA-allowed concentrations for each isotope. If this sum of ratios is less than one, then the EPA criteria are assumed to be met. For the shielding geometry of Fig. 7.1 and an assumed intensity of 1×10^{20} protons per calendar year the ratio of ^{3}H to its allowed concentration is estimated to be 0.04 and the ratio for ^{22}Na is estimated to be 0.70 for a total of 0.74.

7.2.4 Activation of Beam Line Components

Scaling from previous neutrino experiments, beamline components can be expected to become activated to levels of tens to perhaps even hundreds of rads per hour depending on the total activating flux and the allowed cooling times. It will not be possible to approach these components to repair them. Provisions will be made to remotely disconnect and remove devices and place them in shielded coffins for storage.

7.2.5 Muons

Muons should be easily handled for the slant beam case. The pre-target enclosure will be below grade near the Main Injector elevation, so any muons produced due to accidental losses should remain below the surface. The decay muons produced after the target will benefit from the downward direction of the beam line and should likewise present no radiation concern.

7.2.6 Air Activation

The beam will pass through about 80 meters of air, resulting in the production of ^{11}C, ^{15}O and ^{13}N, These short-lived isotopes will pass through a stack and be monitored to assure compliance with release limits. Simple scaling from the Tevatron neutrino program would imply activity releases about 7 times greater for the Main Injector neutrino program.

7.3 Radiation Safety in the Tevatron Beams

We concentrate here on safety in the Sign-Selected Quadrupole Triplet. The existing enclosure and dump for the Quadrupole Triplet runs should be adequate even at the higher intensity of the Main Injector.

7.3.1 Ground Water Activation from the Tevatron Beams

The Phase 1 P-815 experiment will be located in the existing neutrino area. Additional shielding will be required for the sign-selected beam running mode to reduce soil and ground water activation to acceptable levels. This is because the targeting and beam dumps are located in a part of the neutrino area that is not protected by any impermeable barriers.

The activity produced in the surrounding soil will be reduced by placing 3 foot thick concrete blocks within the enclosure to create a shielded cave for the target, magnets and dumps. Additionally, steel shielding will be added to the beamline magnets and the E744/E770 dumps to give a minimum of 13.5 feet of earth-equivalent shielding before reaching the soil in the radial direction. There is room within the existing enclosure to place this amount of shielding along the sides and top. There is not sufficient room below the beam line since it is only 3 feet above the floor. To increase the shielding below the beamline, it will be necessary to remove portions of the floor beneath the target, beamline elements and dumps so that an additional 1.5 feet of steel may be added, for a total of 4.5 feet of steel below the beam. We sketch the arrangement in Fig. 7.2.

CASIM was used to model the proposed shielding geometry and arrive at the total activity produced in the soil outside the enclosure.The magnet polarities and targeting angles were arranged to dump the beam in the first of the two dumps for the sign-selected beam. A one interaction length target and 5×10^{18} 800 GeV protons per year were assumed (this is consistent with 10^7 sec/year as described in Sec. 2.1.2). Since this is a horizontal beam we made the standard assumption that the isotopes radioactively decayed while migrating to the aquifer. The migration rates and other parameters were given in Table 7.2. The aquifer was assumed to be located 63 feet below the beamline elevation. The ratio of ^{3}H to its allowed concentration was calculated to be 0.86, while that for ^{22}Na was 0.13, giving a total of 0.99. Since this is less than 1, the EPA criteria are satisfied.

7.3.2 Prompt Shielding

A cylindrically symmetric approximation to the shielding design shown in Fig. 7.2 was used in a CASIM calculation to estimate the amount of earth-equivalent shielding required to reduce

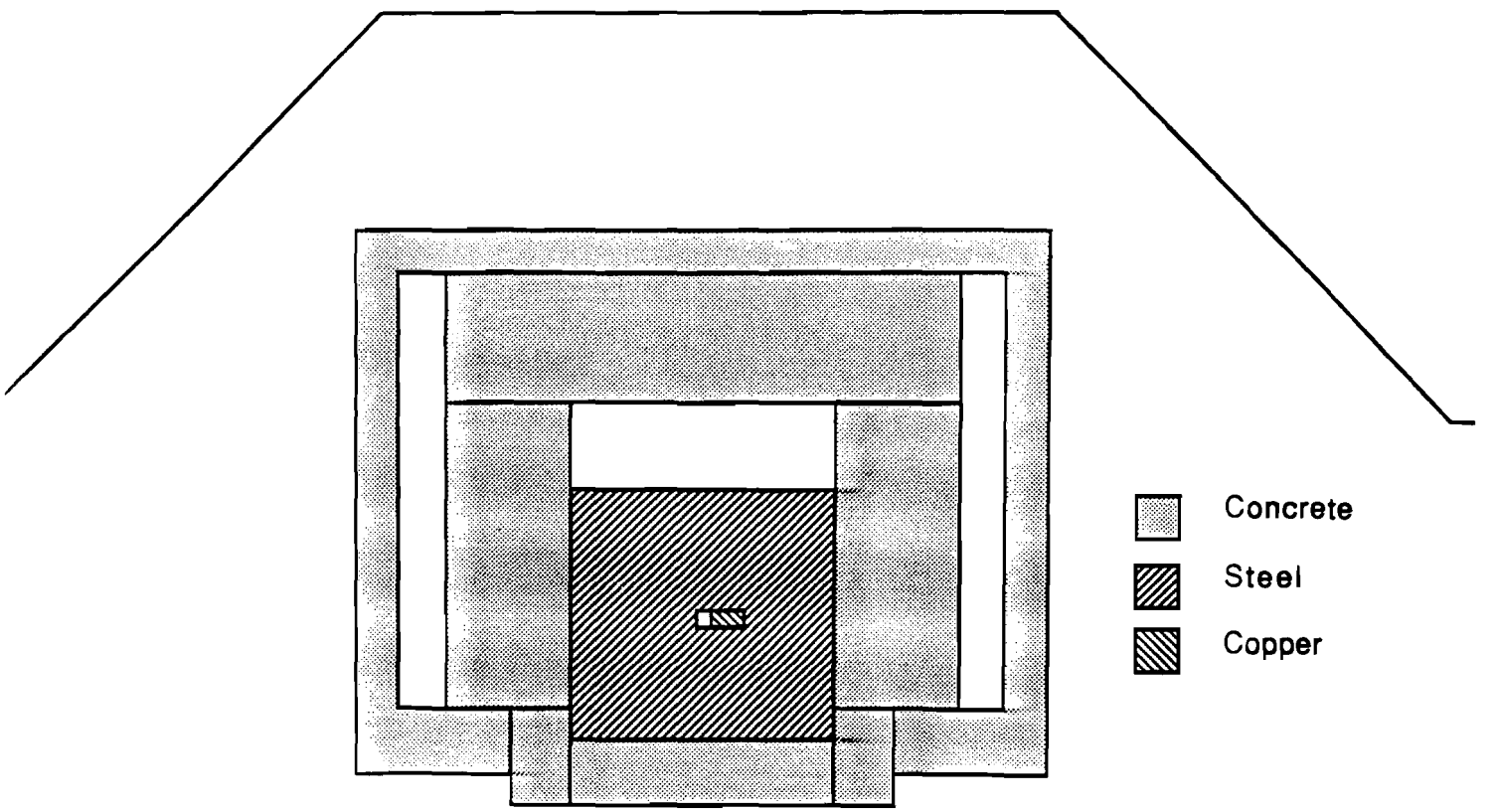

Figure 7.2: Radiation Shielding for Sign-Selected Quadrupole Triplet (not to scale).

the prompt radiation dose rate to 2.5 mrem per hour, the appropriate level for a minimally occupied outdoor area not protected by signs and ropes. The proposed concrete shielding cave and its enclosure walls, together with the steel surrounding the beam dump, provide 16.7 feet of earth-equivalent shielding. The dose rate immediately outside the enclosure was calculated to be 56.9 rem per hour for an 800 GeV beam incident on a 30 cm long Be target. The intensity was assumed to be 4×10^{13} protons per spill and 60 spills per hour. To reduce the rate to 2.5 mrem per hour requires an additional attenuation of 4.4×10^{-5}. This can be provided by an additional 400 cm (13.1 ft) of earth overburden, assuming the standard attenuation factor of ten for each three feet of earth. Therefore, the total amount of earth-equivalent shielding required over the beamline in the region of the target and dumps is 29.8 feet.

7.3.3 Activation of Beamline Components

The activation levels will be comparable to the existing Tevatron 800 GeV neutrino program. Existing procedures will be used to deal with activated components in the beamline.

7.3.4 Air Activation

Airborne activation levels will be comparable to the previous Tevatron neutrino program and will be dealt with using existing procedures and monitoring.

7.4 Other Safety Issues

Life safety in addition to radiation protection involves cryogenic concerns such as cryo-storage and oxygen deficiency hazard (ODH), fire hazards such as using flammable gases, electrical hazards involving high currents and/or high voltages, environmental protection hazards such as the use of liquid scintillator or PCBs, effects of large-volume magnetic fields, and many aspects of construction and assembly (use of cranes, hoists, *etc.*)

Addressing these concerns may be divided according to beam lines and experiment type.

Cryogenic magnets are not used in any of the proposed beam lines, thus no ODH hazards are present. Fuel is minimal in beam-line enclosures since concrete is used throughout, magnets are steel and copper, piping is all metallic, and only cable insulation need be considered. Egress requirements and fuel quantities are similar to those for the New Main Injector, which are under review and will be discussed in a forthcoming Preliminary Safety Analysis Review. The Main Injector neutrino beam has the additional problem of a horn focusing

system involving both high voltages and large electrical currents. Though its operation is normally remote, further study is needed.

P-815, the Tevatron effort, is an upgrade of an existing apparatus which has passed several safety reviews by the Laboratory. This upgrade includes no items presenting safety concerns other than those for existing equipment. Similarly, detectors for all long-baseline efforts other than DUMAND presently exist and have passed safety reviews.

The short baseline effort P-803 is a new effort and has not been reviewed, though many of the safety considerations are similar to those for previous Fermilab experiments. P-803's large air-core cryogenic magnet previously was used for the Fermilab 15 Foot Bubble Chamber, and magnetic-field safety procedures are well established. The ODH problem presented by a large cryogenic system in an underground hall is a hazard which has been addressed by the D0 collider facility. Elevator shafts and stair-wells sealed from the main hall have been provided for egress under ODH conditions; standard ODH procedures (local oxygen masks, remote viewing, etc.) also will be provided as needed. Electrical apparatus is conventional and similar to that used in other underground experimental halls. Construction and assembly safety concerns also are similar to those faced by the CDF and D0 colliders.

References

[1] "High Energy Particle Interactions in Large Targets", A. vanGinneken and M. Awschalom, Fermilab, Batavia, IL, 1975.

[2] "Soil Activation Calculations for the Anti-Proton Target Area", Peter J. Gollon, Fermilab TM–816.

[3] Fermilab Radiation Guide, Fifth Edition, Chapter 6.1.3, March 1988.

[4] "Derived Concentration Guide for Accelerator-Produced Radionuclides in Surface Water Discharge and Drinking Water," J. D. Cossairt, Fermilab Environmental Protection Note #1, March 13, 1990.

8 Civil Construction

8.1 Overview

The Civil Construction for the Main Injector Neutrino Program is driven by three considerations:

- The statistical requirements of the experiments demand extended decay regions; hence the facilities must extend for hundreds of meters.
- The intense beams, especially for the 120 GeV program, demand considerable attention to environmental shielding. The cost of civil construction is dominated by satisfying the shielding requirements over the hundreds of meters of beamline.
- Long-baseline oscillation experiments require beams pointed into the Earth ("slant beams"). The excavation, shielding, and construction techniques must be suited to the depth of the facility.

We have designed a system compatible with these constraints; analyzed in this section are options for siting the proposed neutrino experiments, methods of meeting environmental safety needs, and construction techniques for "slant beam" designs. A detailed design is considered for a new 120 GeV short/long baseline neutrino oscillation program.

8.2 Tevatron Program Construction

Relatively little new construction is required for the Tevatron program; hence the best solution is to use the existing facilities. As described in Sec. 5, the Quadrupole Triplet beam has already been operated; the Sign-Selected beam will operate immediately upstream of

it in N01. The major change necessary is to ensure acceptable groundwater activation and prompt doses for the new beams and higher intensities of P–815.

As detailed in Section 7.3, current ground water shielding around the existing decay pipe should be adequate, without need for additional upgrades. Integral beam luminosities (scaled for Tevatron energies) of the P-815 program will be less than those of the prior Main Ring Neutrino runs for which this system was designed and operated.

The major civil construction then required for P–815 is modification of the floor in the existing Enclosure N01 to guarantee adequate groundwater shielding around the target and beam dumps. The beam center is 3.0 ft. above floor level, with a requirement of 4.5 ft. of steel shielding radially around the dump center. Figs. 5.3 and 7.2 indicate the shielding required and their location in the N01 tunnel. Floor trenching and rebuilding is required for a linear distance of 48 ft. including both beam dumps. The existing tunnel floor is a structural part of the system design. Interim bracing is required during construction of a new reinforced concrete pit.

After installation of the dump shield, illustrated in cross section in Fig. 7.2, access will be precluded through this section of N01. This condition also existed in prior Tevatron neutrino runs, with existing enclosure exits allowing adequate access to either end of the beam dump area. After the replacement of the floor the beam elements can still be removed along the existing train and spur system.

8.3 120 GeV Program Construction; Design for Environmental Shielding

Unlike the proposed Tevatron neutrino experimental program, integrated beam luminosity for the short baseline oscillation experiment P-803 will be far in excess of previous Main Ring running. This precludes using the existing Neutrino area target tube, decay pipe and beam dump system without substantial upgrades. The major civil construction requirement for P-803 will be to achieve the environmental radiation shielding specifications detailed in Section 7.2. The need for a shielded system over a distributed length of 330 meters, from the target to beam dump, has a considerable impact on experiment costing and siting options.

A major goal of the design of the 120 GeV neutrino oscillation facility is to provide construction which safely addresses environmental radiation shielding needs, as presented in Section 7.2. Fermilab experience is that this is best done with massive steel shielding around all areas where significant radioactivation is produced. We choose this technique in the regions where activation is most intense, such as around the target and horn system, as shown in Fig. 7.1. At the beam dump, a steel "backstop" of large radial extent and sufficiently long to absorb the full hadron shower is used.

Over the extended region of the 240 m. long decay pipe, the activity is much reduced and we can use less costly methods. In this region we will use a multilayer impermeable membrane barrier. The membrane will also encompass the target and beam dump regions. We point out that 89% of the total radioactivity produced is contained within the target/horn steel shield, while 95% of the total is contained in steel, including the beam dump. Hence the membrane is only used to contain a small fraction of the total radioactivity.

The design of barrier environmental shields has progressed considerably since construction of the existing NCenter "bathtub" system, in the early 1970's. The existing shield is also far too small for Main Injector intensity requirements. Projected for the P–803 design is a new multilayer shield constructed of 40–60 mil. thick layers of very low density polyethylene. Each layer is assembled with seamless construction techniques; details of the environmental shield construction are shown in Figs. 8.1 and 8.2.

8.4 Siting Options for Short Base Line Oscillation Experiment P-803

The approach taken in selecting potential sites for P-803 is three-fold. An analysis of the existing NCenter neutrino system has been carried out, with emphasis on determining those parts of the facility which must be rebuilt to stage the Main Injector short base line neutrino program. Details of this analysis are presented below. Relative costing comparisons have been made with the requirements for a new site for the short-baseline (SBL) experiment. Finally, a comparison has been made of the cost requirements for a stand-alone short baseline experiment, and for coupling the SBL detector as the front detector for a long baseline facility.

8.4.1 Existing NCenter Area Option

The advantage of the existing NCenter facility for staging P-803 would be the ability to utilize significant portions of the present construction. Many of the experimental needs such as primary beam transport enclosures, service buildings, and electrical power requirements could be met in this manner. Some of the reusable existing construction includes:

Switchyard primary beam transport enclosures An extracted beam design from the Main Injector to N01 has been developed [TM1599], which enables cost efficient beam transport for the 120 GeV beam using existing enclosures. New berm pipes between tunnel sections must be built, but require only modest cost. Status of primary beam enclosure shielding for existing tunnels is currently under evaluation for the Tevatron program using digitized aerial survey data [VANGO]. Again, any required upgrades

for the Main Injector program should be of minimal cost, especially considering the reduced primary beam energy.

Pretarget beam enclosure N01 This enclosure is more than adequately sized for the pretarget primary beam elments to be used for P-803. Repositioning of elements would be required between runs of the 120 GeV and Tevatron neutrino programs, but new civil construction should not be required.

Service Buildings Power supply and control space requirements for the 120 GeV neutrino program are comparable to the facilities required for previous runs using a horn focusing system. The existing service buildings should be reusable here.

Electrical Substation/Feeders This system should also be adequate to support the 120 GeV SBL neutrino program. Logistical incompatibilities between the Main Injector and Tevatron programs, require alternate running cycles; this provides a saving in capital power requirements.

A significant part of the existing NCenter neutrino facility must, however, be rebuilt to meet radiation shielding requirements for P-803. The crucial requirement is the greater radial shielding necessary for the Main Injector program. Some of the facilities for which demolition and complete rebuilding are required are:

- NC target hall.
- NC decay pipe membrane system.
- NC beam dump enclosure.

Demolishing 1350 ft. of existing facilities would be a major expense. The task would be greatly complicated because the soil in the present bathtub has low-level radioactivity. This soil must then be carefully staged and replaced in the new impermeable membrane construction.

The short transverse distance to adjacent beam lines NWEST and NEAST also has a significant impact on construction requirements. Construction of the needed environmental decay pipe shield for P-803 would require major demolition of adjacent construction, including:

- All NE facilities for a distance of more than 1000 ft.
- Enclosures NW2, NW3, and the upstream portion of NW4.

Additional facility modification would be needed as follows:

1. Construction protection of NMuon enclosures over a distance of 1030 ft.
2. Removal of 2685 Tons of steel from the existing NC muon shield. This is required for placement of the P-803 detector hall.
3. Addition of 3710 Tons of steel within the NW4 enclosure. This provides a comparable muon shield to the existing shield, as needed for P-815.
4. Reworking of utility runs along the current NC berm.

A detailed complete costing for staging P-803 in the existing NC area has not been compiled. However, the demolition and rebuilding requirements listed here have been found to increment the project cost by at least $4M beyond projected costs for a new experimental area, even after discounting for viable existing facilities. An additional disadvantage of staging the Main Injector and Tevatron neutrino programs in the same area is that they are logistically incompatible, requiring separate running periods as well as significant change-over of elements.

Hence, the current judgment is that a new experimental site for staging P-803 is strongly preferred to rebuilding the existing NCenter facility.

8.4.2 New Area Siting for P-803

Requirements for optimal siting of the short baseline neutrino oscillation experiment include utilization of existing primary beam transport systems, or minimal construction need for new beam transport; ready access to utilities; and large undeveloped space for construction of the shielded 330 meter target, decay pipe, and beam dump system. Other considerations are the possibility of combining the short and long baseline neutrino oscillation facilities.

A particularly advantageous site is to the East of the Main Injector. This makes it possible to combine the 120 GeV extraction system with the machine abort channel, as detailed in Section 6.3.1. Additionally, sharing utilities with the Main Injector construction is feasible, and a large open area is available for the neutrino beam system construction. Finally, this siting permits the option of aiming the neutrino beam at the IMB detector, creating a long baseline program for minimal additional cost.

Other new area siting options could also be tied in to the existing Switchyard primary beam system. For the purpose of analyzing and costing one design in detail, we have chosen to consider the siting of the neutrino oscillation program using a direct extraction from the Main Injector at MI-50.

8.4.3 15 Ft. Bubble Chamber Magnet Move

If P-803 is to be sited in a new area, the 15 ft. Bubble Chamber magnet would first have to be transported and lowered into a pit of the necessary depth, and then be reassembled and operated as much as 100 ft underground. We have investigated the move of the Bubble Chamber magnet and find it presents no significant difficulties. Local rigging contractors have all of the special equipment needed for moving the magnet from Lab B to the new site, and lowering it into position. It will take two man years of effort from the RD/Cryogenics Department to prepare the magnet for moving.

The costs reflect expenses necessary for modernizing the magnet refrigeration system, allowing remote operation via the beamline control system, increasing reliability, and reducing manpower required for magnet operation. These include a modern screw compressor and satellite style multibus process controller. The costing shown assumes that only the dewar and coldbox from the old system are available and all other components must be purchased new. If the physics program in the new muon lab were changed, it is possible that many of the expensive components such as liquid nitrogen dewar and compressor would not have to be purchased.

We have looked at operations with the magnet located in a 100 foot pit with the proposed operating conditions. At the full desired field, the old coldbox will have a refrigeration capacity twice as large as the magnet boiloff. Cool- down will probably take six weeks with the present coldbox. In operations at the Bubble Chamber liquid hydrogen was available as a cooling fluid. The new location will not have hydrogen and cooldown will be extended because of additional cooling the refrigerator expansion engine must do. An ODH system is necessary and is provided in the estimate. Additionally, special ventilation for the pit will be required. Liquid nitrogen, in the pit for cooling the magnet shield, will need to be removed by powered ventilation if a spill should occur. No other difficult issues have been discovered.

8.5 Civil Construction Techniques for Oscillation Experiments

We have considered a variety of construction techniques to minimize cost for the proposed neutrino oscillation facility. Avantages of each are strongly coupled to the depth [and hence penetration angle] of the beam line. These include trench construction, the standard technique for shallow beam systems; slurry wall construction, which minimizes the transverse space needed for a deeper facility; and tunnel boring, as would be needed for a very deep facility such as the DUMAND proposal P-824. Fig. 6.2 illustrates the required beam line downward bend angles for the range of long baseline proposals.

8.5.1 Trench Construction

This is the technique of choice for a short baseline facility. It combines ease of construction with minimized cost, and has no disadvantages at depths to 25 ft. below grade. For a long baseline facility aimed at either the IMB or Soudan detectors, excavation would be required to depths of 80–100 ft. At these depths, trench construction is still a viable and cost-effective technique.

There are two options within the trench construction method.

V-Version Here the trench follows a 1/1 (x/y) slope from grade to the confined earth system (33 ft. deep and 42 ft. wide), and a 3/1 slope at greater depths. The disadvantage is that to maintain the minimum required trench slope, excavation at the required depths will requires considerable transverse excavation, growing linearly to approximately 300 ft. near the detector hall.

Y-Version A 1/1 slope is followed from grade. At the upstream end the depth is 25 ft. and grows in three increments to 62 ft. at the detector hall; the main difference from the V-Version is that along the entire length the additional 33 ft. (defining the confined earth system) is constructed straight-down using a retaining wall. This method requires somewhat more construction near the base but involves less transverse excavation, since the 3/1 slope is unnecessary. The transverse excavation near the top is 165 ft. across for most of its length. This option is displayed in Fig. 8.4.

A detailed cost-comparison indicates the Y-trench is less expensive than the V; we have therefore chosen to present the Y-trench as the preferred option, although given the closeness of the costs, we will present the V-version costs in Part IV.

Figs. 8.1 and 8.2 illustrate cross-sectional views of the target enclosure and environmental shield using trench construction in the V and Y–versions respectively.

8.5.2 Slurry Wall Construction

A slurry wall system is constructed by vertical excavation of a 2 ft. wide trench section, which is filled with bentanite slurry as the excavation proceeds. Concrete is then added to displace the slurry and form a solid concrete retaining wall. The advantage of this construction technique is that walls of significant depth can be constructed with far less total excavation than in the trench method. Slurry walls become cost competitive with trenching at greater depths and allow deep excavation in narrow spaces.

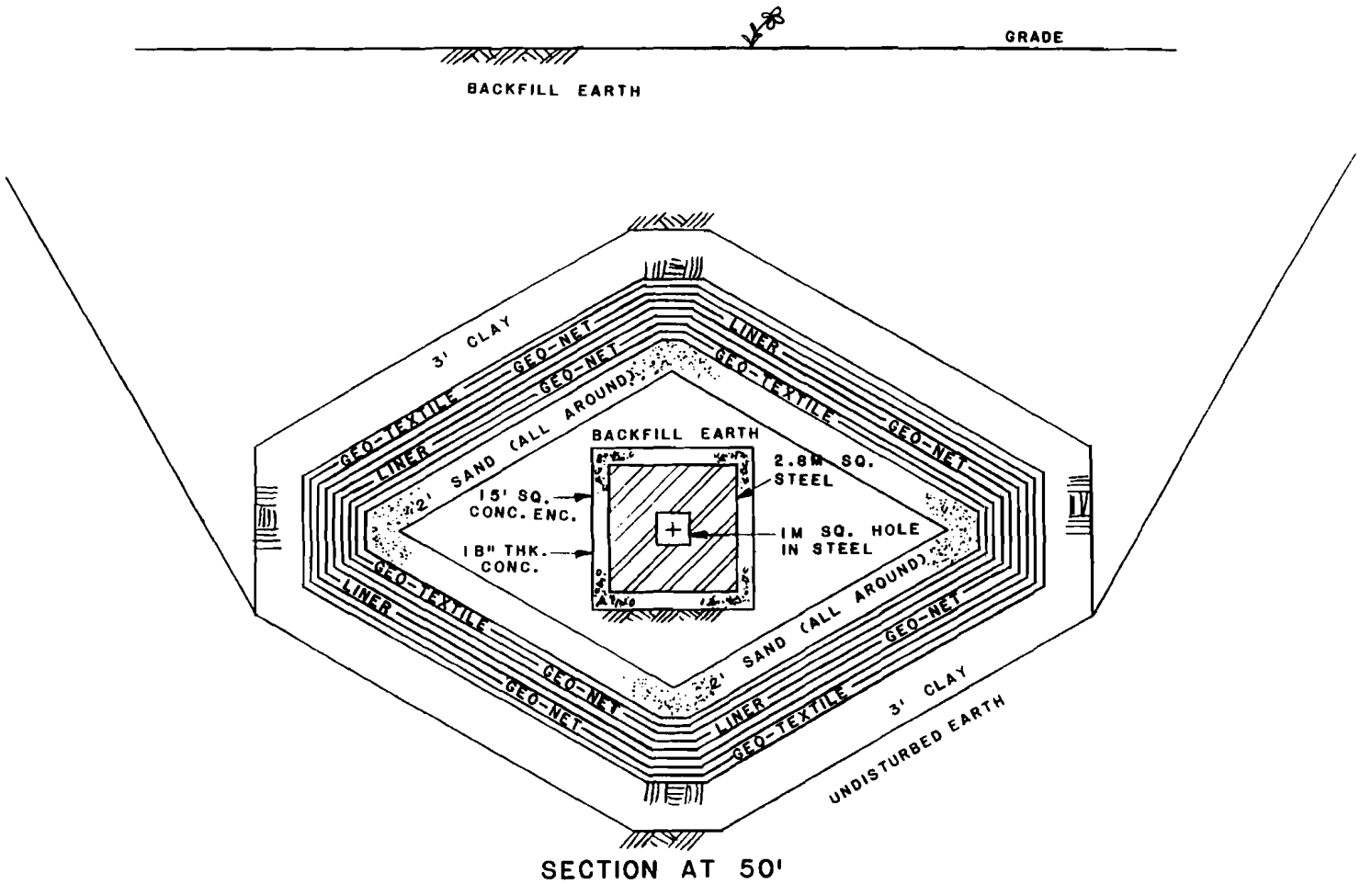

Figure 8.1: Cross-Sectional View of Shield System for V–Trench Construction. The picture is not to scale.

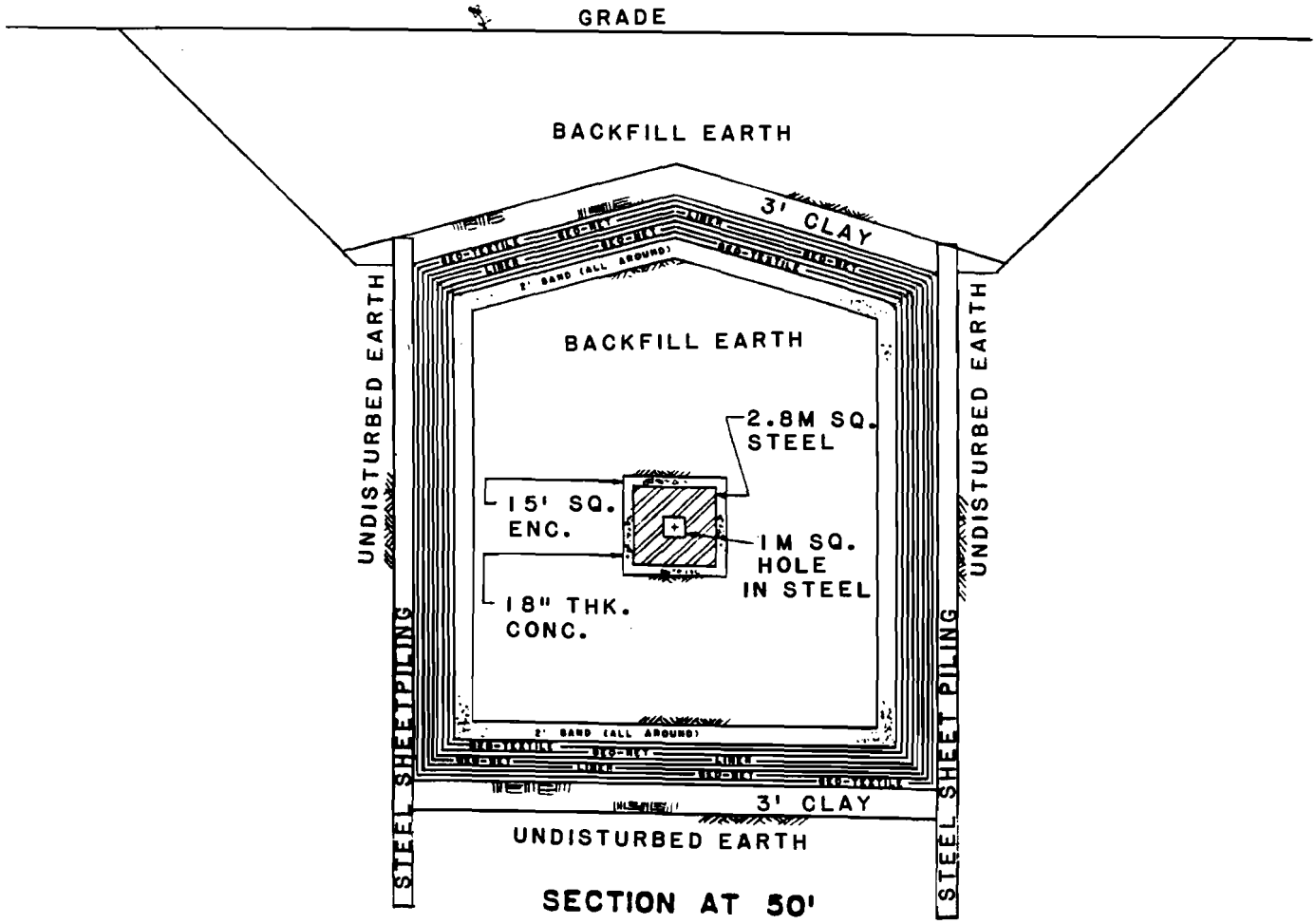

Figure 8.2: Cross-Sectional View of Shield System for Y–Trench Construction. The picture is not to scale.

8.5.3 Tunnel Boring

This construction method is advantageous for deep tunnels, especially when the bulk of the beam line would be below the dolomite or "bedrock" layer, typically beginning at depths of about 80 ft. at the Fermilab site. This is the optimum technique for an oscillation experiment using the DUMAND detector, where the decay pipe system reaches depths of over 500 ft. Initial mobilization costs are significant, but boring costs are not a strong function of the tunnel depth.

8.5.4 Relative Costs for Oscillation Experiments vs. Baseline Length

As part of the design effort for the Main Injector neutrino program, a detailed study has been done of the relative beam line facility costs as a function of baseline length for current oscillation experiment proposals. In each case, for ease of comparison, the experiment location is assumed unchanged. Thus the comparison is that of cost *vs.* beamline projection angle, and hence depth, below the horizon. These costs are benchmarked to projected facility costs for the short baseline experiment.

Total decay tunnel length from target to beam dump is 320 m. for each case, as specified in Section 6.7. The environmental safety shield is sized as in Section 7.2. Details of the target and two–horn focusing system remain unchanged for each configuration. Additional dipole magnets and thus pretarget tunnel length are required as the baseline is increased. The dominant additional cost incurred is due to the added depth of the decay pipe, beam dump, and short-baseline (SBL) detector hall.

Cost summaries are presented in Chapter 10. Here, relative costs compared to those for the short baseline facility are presented as a function of baseline length. Construction techniques are determined to be most cost effective using trenching for the short baseline beam, as well as when aimed at the IMB and Soudan detectors. The greater depth of the SBL detector hall is best reached using the slurry wall technique for each of these long base line facilities. DUMAND would require tunnel boring, as explained earlier.

A crucial finding of this study is that for baseline lengths of less than 1000 km the incremental cost of staging P–803 along a line aimed at an existing distant neutrino detector is fractionally small. Table 8.1 presents these costs compared to that for the SBL facility only. We also show relative costs for DUMAND combined with a simple SBL detector and no SBL facility at all.

P–803 could be sited on the line to either the IMB or Soudan detectors without compromise, as well as being the "near" detector for either long baseline effort. The great depth required for the DUMAND line would add significant complications to staging and running

PROPOSAL	BASELINE LENGTH	RELATIVE COST
P–803 Short Baseline	0.5 km	1.00
P–805 IMB + P–803	577 km	1.08
P–822 Soudan 2 + P–803	822 km	1.22
P–824 DUMAND + SBL	6239 km	2.17
P–824 DUMAND + simple SBL	6239 km	1.89
P–824 DUMAND + no SBL	6239 km	1.57

Table 8.1: Incremental Costs for Long Baseline Facilities, Normalized to Short Baseline Cost.

the short baseline detector experiment. (For example, the 15 ft. bubble chamber magnet coils could not be tipped the required 30° out of the horizontal.) Additionally, significant detector design modifications would be required due to logistical and safety requirements. It is felt that P-803 would not be a viable complement to this very long baseline effort. Costed for inclusion in Table 8.1 is a deep detector hall in which a simpler short baseline detector could be mounted.

8.6 Civil Construction Design for a Combined SBL/LBL Facility

We have found that the cost of P–803 on a slant beam pointed at either IMB or Soudan 2 is only marginally more expensive than P–803 alone. Therefore we have chosen a combination of the short baseline experiment P-803 on a slant beam trajectory toward the IMB long baseline detector P-805 for a detailed design and cost study. Projected facility siting is to the East of the Main Injector, using the extracted 120 GeV beam from MI-50 as described in Section 6.3.1. The indicated region indicates the size and location of the necessary excavation. The overall layout on the Fermilab site is shown in Fig. 8.3; plan and elevation views of the experimental facility itself are shown in Figure 8.4.

Civil construction for the extraction channel and machine abort are considered separately as part of the Main Injector Conceptual Design Report. Beam is transmitted from the extraction channel to the Pretarget Enclosure for the Neutrino program. Primary beam elements are located in this enclosure which provide the required downward bend of 44.8 mrad. as well as focusing of the beam on the primary target. The size of the Pretarget Enclosure is 20 ft wide by 160 ft long. The enclosure includes a shielded alcove in which the target/horn train may be staged as well as a drop hatch through which elements are removed by crane.

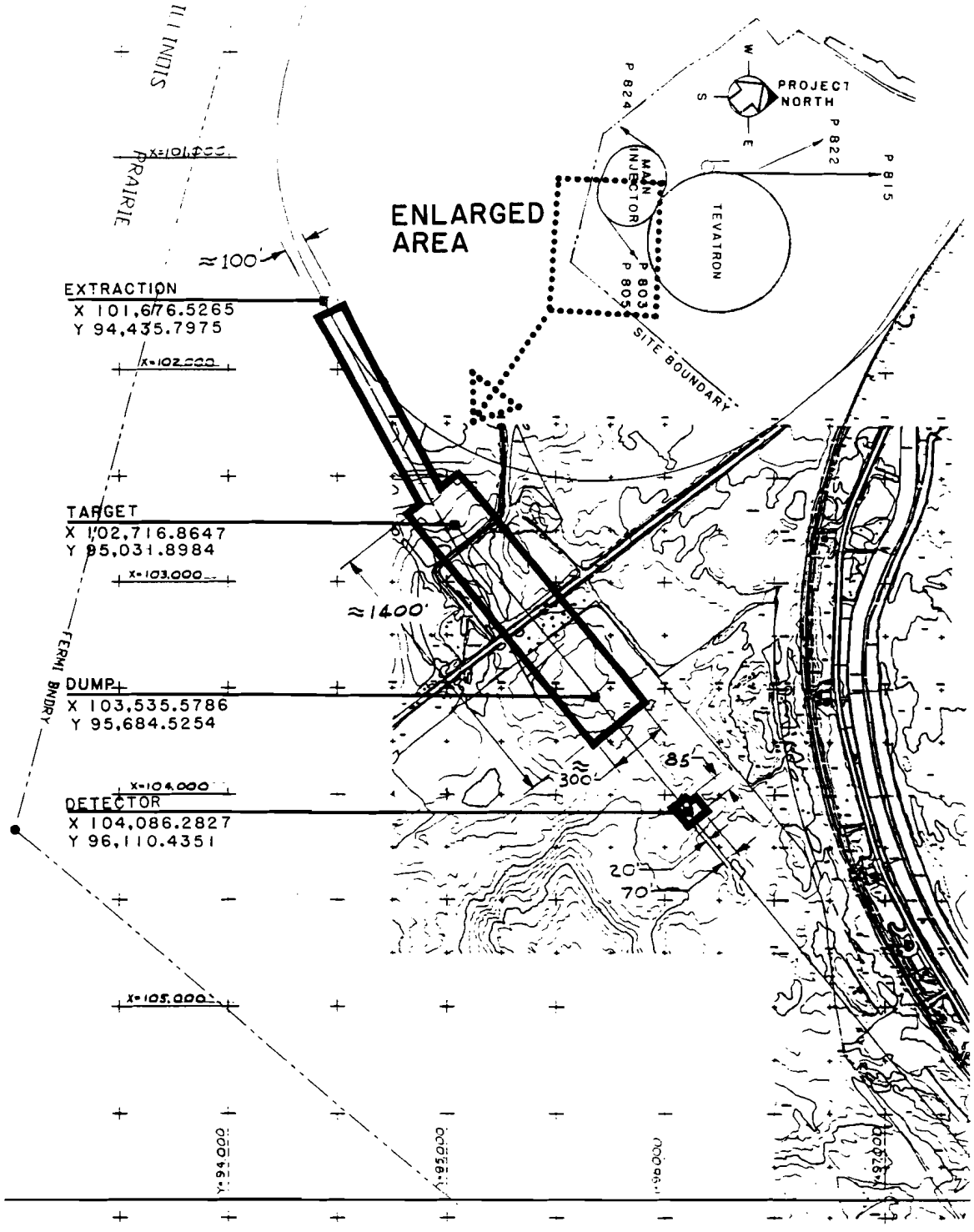

Figure 8.3: The orientation and size of the P–803/IMB Combined Beamline. The region up to the dump is indicated by the heavy lines; the P–803 detector is the small square following the beamline.

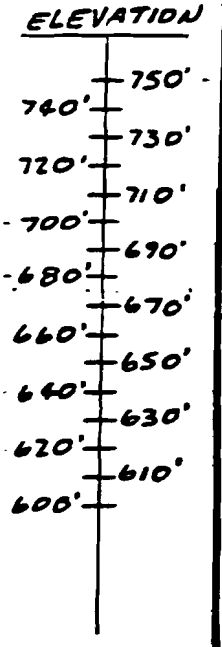

ITEM NO.	PART NO.	DESCRIPTION OR SIZE	QTY. REQ.

PARTS LIST

UNLESS OTHERWISE SPECIFIED			ORIGINATOR	BROWNING	
FRACTIONS	DECIMALS	ANGLES	DRAWN	BROWNING	5-13-91
±	±	±	CHECKED	KULA	
1. BREAK ALL SHARP EDGES 1/64 MAX.			APPROVED	S. Kula	5-13-91
2. DO NOT SCALE DWG.			USED ON		
3. DIMENSIONING IN ACCORD WITH ANSI Y14.5 STD's.			MATERIAL-		
√ MAX. ALL MACHINED SURFACES					

FERMI NATIONAL ACCELERATOR LABORATORY
UNITED STATES DEPARTMENT OF ENERGY

NEUTRINO PROPOSAL
P803 & P805 "SLANT BEAM" – "Y" VERSION
PLAN & ELEVATION

SCALE	FILMED	DRAWING NUMBER	REV.
NOTED		2900.210-XE-177846	

Figure 8.4: A fold-out Schematic of the P–803/IMB Combined Beamline Layout. The picture is drawn to scale.

Entrance to the Target/Horn hall is at the downstream end of the Pretarget enclosure. The size of this hall is 15′ × 15′ × 263′L. It contains the target/horn access tunnel of cross section size 1 m × 1 m, which is surrounded by steel shielding as described in Section 7.2. The size of the hall is dictated by the radial steel shielding requirement. The hall is then surrounded by earth shielding encapsulated in the impermeable multilayer membrane system described in Section 8.3.

The 240 m. decay pipe of diameter 1.0 to 1.5 m. is located downstream of the Target/Horn hall. This pipe is also surrounded by the impermeable shield over its full length, as is the downstream beam dump. Diameter of the shielded earth cylinder in the decay pipe region is 32 ft. over the full length of the decay pipe. Fig. 8.4 illustrates the excavation needed for trench construction, along with the slurry wall option shown as a dashed line. For this design, slurry wall excavation in the decay pipe region added a projected cost penalty of 12% of the project total, but could be an alternative if the limits of trench excavation were to extend into environmentally sensitive areas. For the location considered here, trench construction should be viable and is the most cost effective option.

The depth of the beam dump at the downstream end of the decay pipe is approximately 77 ft. below grade at beam center. This is near the geological boundary between the upper glacial till layer and underlying dolomite. As the beam dump location is near the shallow well aquifer level, it is very conservatively designed with 6 ft. of radial steel shielding, also surrounded by the impermeable shield.

No construction is required in the 200 m. region downstream of the beam dump, as the short base line detector muon shield utilizes existing earth. This enables very considerable cost savings compared to a steel muon shield, with only a small loss in flux for the short baseline detector (approximately 20%). The long baseline detector is unaffected.

The SBL detector hall is then located 200 m. downstream of the beam dump with the detector centered a total of 538 m. downstream of the primary target. The depth of the detector hall, with floor elevator more than 120 ft below grade, is most efficiently reached using slurry wall construction. Floor space of the detector hall is 40 ft × 55 ft. A service building and counting house space are then located at and near grade level above the detector hall pit, as shown in Fig. 8.4.

Costing details for this combined short/long baseline slant beam facility are presented in Chapter 10.

Table 8.2 presents the power requirements for the facility. We have costed the 750 KVA supplies but not the power cost for the other items in the Table.

	DESCRIPTION	QUANTITY	AC POWER	
	MAGNET / POWER SUPPLY			
1.	3Q60 / ACME 22.5KW	1	20	
2.	3Q60 / ACME 22.5KW	1	20	
3.	KICKER	2	-	
4.	B-2 / TRANSREX 500KW	1	400	
5.	4-4-30 / P.E.I. 20	1	20	460 KVA
6.	STEEL BEAM DUMP	—	—	
7.	KICKER	2	—	
8.	B-2 / TRANSREX 500KW	6	2070	
9.	3Q120 / LING 55KW	2	65	
10.	B-2 / TRANSREX 500KW	2	600	
11.	3Q120 / LING 55KW	1	30	
12.	4-4-30 / P.E.I. 20	1	20	2785 KVA
13.	TARGET	—	—	
14.	FOCUSING HORN	2	50	50 KVA
	SUPER CONDUCTING MAGNET EQUIPMENT			
15.	400HP COMPRESSOR	1	350	
16.	10HP COMPRESSOR OIL PUMP	1	11	
17.	25HP SHIELD COMPRESSOR	2	48	
18.	40KW COLD BOX	1	40	
19.	5HP MAGNET VACUUM FOREPUMP	1	6	
20.	3HP MAGNET VACUUM DIFFUSION PUMP	1	4	
21.	25HP RECOVERY COMPRESSOR	2	48	
22.	150KW MAGNET POWER SUPPLY	1	150	
23.	10KW ENGINE SPEED CONTROLS	2	24	
24.	7.5HP UTILITY VACUUM PUMP	1	8	
25.	MISCELLANEOUS	—	111	800 KVA
	WATER PUMPS			
26.	100HP PUMP/CONVENTIONAL MAGNETS	2	200	
27.	100HP PUMP/STEEL BEAM DUMP	1	100	300 KVA
	ELECTRONICS 750 KVA SUPPLY			
28.	DETECTOR HALL SERVICE BUILDING	2	150	
29.	DETECTOR HALL PIT	2	150	300 KVA
	HOUSE POWER			
30.	MAGNET SERVICE BUILDING	—	100	
31.	DUMP SERVICE BUILDING	—	50	
32.	DETECTOR HALL SERVICE BUILDING	—	100	
33.	DETECTOR HALL PIT	—	200	
34.	MAGNET/TARGET/HORN TUNNEL	—	100	550 KVA
	TOTAL POWER LOAD			5245 KVA

Table 8.2: P–803 and P–805 Slant Beam Power Load

Part IV

Costs: Experiments and Civil Construction

9 Experiment Costs

In estimating costs for all experiments we followed the Main Injector CDR Rev. 2.3 for EDIA/Contingency Guidelines and assigned the following contingencies:

- Estimates based on previous actual purchases, quotes, or catalogue prices are assigned 15%.
- Undocumented Engineering Estimates are assigned a 30% contingency.
- Labor is assigned a 30% Contingency.

We discuss the estimated cost for P–815 and P–803. The cost to the Laboratory for upgrades to any of the long-baseline experiments is negligible. The cost for Civil Construction is estimated separately.

9.1 P-815 Cost Estimates

The design of the detector presented in this Report is preliminary; P–815 Phase II has not yet submitted a proposal and we have used a model of the expected detector upgrade, based on consultation with the experimenters and available information from the P–815 Phase I document. These costs should therefore be regarded as highly preliminary.

We enumerate several other issues before giving the costs of the detector upgrade:

1. P-815 has proposed a run in 1994 to measure the electroweak parameters $\sin^2\theta_W$ and ρ. The SSQT will have already been operated for one run and hence the beam will exist at the time discussed in this Conceptual Design Report; the cost was estimated in the P-815 proposal and estimated to be $\approx$ \$300K. The groundwater protection will also be established at that time for \$150K. This is based on estimates of the cost of

steel in the floor at $500/ton (for $100K) and an additional $50K for installation.[1]. This cost is included in the "Existing P–815 Items" in the Total Cost Estimate.

2. P-815 Phase I will test the calorimeter upgrades in a single cart equal to 1/6 of the system costed below. This cost is included in the "Existing P–815 Items" in the Total Cost Estimate.

3. The carts need to be re-built since they will now be larger to accomodate the new instrumentation. We guess $150K.

4. Additional ADC's for the new scintillation conters will be required. The primary cost here will be for additional ADC's; the additional FERAs required will cost $400K.

5. The cost of fan-in/discriminator units is explicitly given. There should be very little additional logic but we will assign an additional $200K to cover contingencies.

6. PREP Costs are based on known use in E-744/E-770 and have been upgraded to reflect the larger number of channels in the new detector.

7. Labor Costs are based on discussions with the Physics Department which took into account the nature of the technical assistance required.

9.1.1 Beam Line Construction

The Sign-Selected Quadrupole Triplet will have been commissioned before the construction of the Main Injector; hence its costs do not apply here. Restoring the Quadrupole Triplet is a straightforward exercise, since most of the elements were simply transferred to the Sign-Selected beam 100 ft downstream in the same tunnel. We have learned from our experience in the $\sin^2\theta_W$ analysis in E-744/770 that Quadrupole Triplet runs of P–815 will require better beam monitoring and therefore make the estimate that the old monitoring system will have to be doubled in complexity at a cost of $50K.

9.1.2 Detector

Scintillator/PMT Upgrades

The preliminary design of the P-815 Phase II calorimeter calls for nine 1 ft wide, 10 ft long and two 6 in wide, 10 ft long staves per plane. Each stave has two PMT's for a total of 22 channels per plane. There are 168 planes for a total of 16,800 ft^2 and 3696 channels (exclusive of the already-constructed cart). We have two quotes from vendors: Nuclear Enterprises and Mitsui Plastics and the average was $100/$ft^2$. Amperex 2202's should be

adequate for our purposes and are currently \$170 each. Ken Gray of the Physics Department Scintillator Laboratory estimated that two technicians for just over one year could perform the gluing, assembly, *etc.* We assumed they would be paid \$25K/year times 1.3 for benefits and overhead. We have also arbitrarily doubled his estimate and assigned the standard 30% contingency.

Table 9.1: Preliminary Cost of Scintillator/PMT Upgrades for P-815 Phase II.

Item	Number	Unit Cost	Raw	Comment	Contingency	Total
Non-Electronics						
Scintillator	16,800 ft^2	\$100/ft^2	\$1680	[2]	15%	\$1932
PMT	3696	\$170	\$628	[3]	15%	\$723
Base	3696	\$50	\$185	[4]	15%	\$213
Power Supply	3696	\$100	\$370	[5]	15%	\$425
Light Pipe	3696	\$50	\$185	[6]	30%	\$240
Stand	168	\$200	\$33.6	[7]	15%	\$38.6
Delay Cable	3696	\$30	\$11.1	[8]	15%	\$12.8
Lemo	3360	\$15	\$50.	[9]	15%	\$57.9
SHV	3696	\$15	\$55.	[10]	15%	\$63.8
Labor	4.4	\$32.5	\$143	[11]	30%	\$186
EDIA	2	\$30	60	[12]	30%	\$66
Sub-Total (non-electronics)			\$3341			\$3958
Electronics						
Fan-In/Discriminator	3696	\$100	\$370	[13]	15%	\$425
Crate Controllers	14	\$4000	\$56.0	[14]	15%	\$64.4
Sum Logic	3696	\$100	\$370	[15]	15%	\$425
Sub-Total(electronics)			\$796			\$914
Total			\$4137			\$4872

† Unit Costs are in \$. Raw and Total Costs are in 1990 K\$. Labor in Man-Years.

9.1.3 Drift Chambers

We require an additional 43 drift chambers identical to those constructed in 1985. The precise cost is difficult to reconstruct but \$1.2M is an approximate figure from Drasko Jovanovic, who headed the Physics Department at that time, exclusive of labor and inflation. From this we assign a rough estimate of \$1.5M, which agrees well with the tabulation below. M. Lamm was the post-doc in charge of construction; he calculated 16 man-weeks per chamber. Again, all prices are in 1990 dollars.

We have not assigned an EDIA since this is a repetition of a completed project; the plans, drawing, *etc.* still exist and no significant modification is expected.

Table 9.2: Preliminary Cost of Drift Chambers for P-815 Phase II

Item	Number	Unit Cost	Raw	Comment	Contingency	Total
Parts	43	$20,000	$860	[16]	15%	$989
Labor	13.23	$32,500	$430	[17]	30%	$559
Sub-Total(Construction)			$1290			$1548
Electronics						
Amplifier/Discriminator	4128	$12	$50	[18]	15%	$57.0
Nevis TDC's	33 crates	$10,000	$330	[19]	15%	$380
FADC's	23 crates	$10,000	$230	[20]	15%	$265
Spectra-Strip	8156	$5	$41	[21]	15%	$46.9
Sub-Total(electronics)			$651			$749
Total			$1941			$2297

†Unit Costs are in $. Raw and Total Costs are in 1990 K$.Labor in Man-Years.

Spectrometer

We have not yet chosen a method for determining muon momentum and therefore cannot assign a cost. However, as an upper limit we can assign the estimated cost of the air-core toroid at $5M from a Saclay engineering design.[22]. This will not be adequate for future studies but we state it in order to give an approximate assessment of the impact on the Laboratory.

9.1.4 Preliminary P–815 Phase II Costs, without Spectrometer

We present the estimated cost of the first-order design of the P–815 detector below. The collaboration expects to present the P–815 Phase II proposal in mid-to-late 1991 with a more accurate estimate at that time. We have explicitly separated the costs of the Phase II test cart, to be built and operated during the P–815 Phase I run, from the Phase I costs.

Table 9.3: Preliminary Costs for Detector Upgrades, without Spectrometer

Project	Cost
Scintillator/PMT	\$4872
Drift Chambers	\$2297
Rigging, Installation	\$150
ADC Upgrade	\$400
New Logic	\$200
Total for Upgrade(including EDIA/Contingency and Labor)	\$7919
P–815 Phase I	\$1990
P–815 Phase II Test Cart	\$1010
Total Cost	\$10919

†Costs are in 1990 K\$.

References

[1] P–815 proposal.

[2] We base the cost on the average of two vendors and therefore use 15% contingency. The first is Nuclear Enterprises America, 7 Deer Park Drive, Monmouth Junction, NJ 08852. The second is Mitsui Plastics, 1–11 Martine Avenue, White Plains, NY 10606. The NE price is 30% more but it is not clear Mitsui can manufacture the scintillator to specifications.

[3] The cost is based on the Amperex 2202 which will satisfy the requirements. It is manufactured by North American Philips, 3601 Algonquin Road, Rolling Meadows IL 60008.

[4] A base design for the Amperex 2202 exists and can be used without modification.

[5] Power Supplies are taken to be the LeCroy 1440 series.

[6] We must design the Light Pipes and have therefore assigned a 30% contingency.

[7] The stands will be made of Unistrut and are of minimal cost and complexity.

[8] Delay cable is standard RG-58.

[9] Lemo cable is a standard item.

[10] SHV connectors are a standard item.

[11] We have an estimate of 2 man-years for the project from the technician in charge of the Physics Department Scintillator Shop. We assume a standard 30% contingency on Labor. Technical staff are assumed to cost \$25K/year with a factor of 1.3 assigned for benefits. We also expect to set up a test system to measure the gains and map the responses of the scintillators. The university collaborators expect to assign a graduate student and post-doc for these tasks as well as help in the fabrication.

[12] Since the majority of the cost is material for scintillator a strict percentage assignment is inappropriate. We estimate EDIA as the complete cost of the construction of two stands (20 counters) which is \$30K.

[13] The fan-in/discriminator units will supply the same logic as for E-744/770 and are standard LeCroy items.

[14] The crate controllers for the LeCroy fan-in/discriminators are also standard items.

[15] The sum logic is the same as for E-744/770 and is standard LeCroy logic; we scaled the E-744/770 requirements to the appropriate number of channels.

[16] The cost of $20K per chamber is typical for the size and number of wires involved. It agrees well with estimates from the Physics Department; unfortunately, data from the E-744/770 budget codes are no longer available.

[17] The project took 688 man-weeks not including startup. We apply the 30% contingency for that period.

[18] This is the 1985 cost scaled by 30%.

[19] This is the 1985 cost; some components have decreased in price.

[20] Same as [19].

[21] 1990 catalogue price for Spectra-Strip.

[22] Letter-of-Intent for a Muon Experiment at Fermilab, Draft, and references therein, C. Guyot *et al.* We have requested a copy of the Saclay Engineering Report on which the estimates are based and scaled the cost of the spectrometer discussed here to the size required for P–815.

9.2 P–803 Detector Costs

This cost estimate for P803 was assembled with information from a number of sources. Wherever possible with the high cost commercial items, a quote or estimate was obtained from at least one supplier. Estimates for items similar to past projects at Fermilab are based on the cost of the past project. All estimates based on pre-1990 numbers have been adjusted to current dollar values.

PREP costs were estimated by making a module count of all low-voltage, high-voltage, and triggering modules and then *doubling* the result.

A contingency of 15% is added to the raw cost estimate for thoroughly engineered or commercially available products. A contingency of 30% is added to the raw cost of assembly labor.

The EDIA time estimates are only approximations based on previous experience. The cost estimate of \$60K/year for EDIA includes salary, benefits and other overhead expenses. A contingency of 30% is added to the EDIA raw cost.

PREP and Data Acquisition						
Element	Unit Cost	Quantity	Raw Cost	Comment	Contingency	Total
NIM Logic	\$1000	100	\$100K	[1]	15%	\$115K
Crate	1500	15	23		15	26
CAMAC	1000	20	20	[1]	15	23
Crate	3000	2	6		15	7
FASTBUS			25	[1]	15	29
Crate		1	25		15	29
PM HVs	200	200	40	[1]	15	46
PWC HVs	250	50	13	[1]	15	15
Vis. scaler	1000	10	10	[1]	15	12
Spill mon.			10	[1]	15	12
Volt. mon.			10	[1]	15	12
Coax cables	15	1000	15	[1]	15	17
Subtotal						343K

Table 9.4: Costs of PREP and Data Acquisition for P–803

Emulsion Facility						
Element	Unit Cost	Quantity	Raw Cost	Comment	Contingency	Total
Structure	50/sqft	1500	75	[2]	15	86
Electrical			10		30	13
Plumbing			10		30	13
HVAC			10		30	13
Environ.			50	[3]	30	65
Equipment			100	[4]	30	130
Installation			25		30	33
EDIA	60K/year	0.25 year	15		30	20
Subtotal						373K

Table 9.5: Costs of Emulsion Facility for P–803

Emulsion						
Element	Unit Cost	Quantity	Raw Cost	Comment	Contingency	Total
Emulsion	12K/liter	200	2400	[5]	15	2760
Subtotal						2760K

Table 9.6: Costs of Emulsion for P–803

Scintillating Fiber Tracker						
Element	Unit Cost	Quantity	Raw Cost	Comment	Contingency	Total
Fiber ribbon(180Kx1.7 m)	0.75/m	306K	230	[6]	30	298
Image intensifier	25K ea	6	150	[7]	30	195
Scint. R&D			100	[8]		100
Readout R&D			250	[9]		250
EDIA	60K/year	1 year	60		30	78
Subtotal						921K

Table 9.7: Costs of Scintillating Fiber Tracker for P–803

Drift Chambers (mechanical)						
Element	Unit Cost	Quantity	Raw Cost	Comment	Contingency	Total
Materials	5K	18	90	[10]	30	117
End plugs	2	54	108	[10]	30	140
Machining	10K	18	180	[10]	30	234
String wire	4K	18	72	[11]	30	94
Misc. assy.	1K	18	18	[11]	30	23
EDIA	60K/year	0.5 year	30		30	39
Subtotal						647K

Table 9.8: Costs of Drift Chambers (mechanical) for P–803

Drift Chambers (Electrical)						
Element	Unit Cost	Quantity	Raw Cost	Comment	Contingency	Total
Amp/TDC MUX/cables	50/chan	15324	766	[12]	15	881
EDIA	60K/year	1 year	60		30	78
Subtotal						959K

Table 9.9: Costs of Drift Chambers (electrical) for P–803

EM Calorimeter (Mechanical)						
Element	Unit Cost	Quantity	Raw Cost	Comment	Contingency	Total
Lead alloy	0.80/lb	44	35	[13]	15	40
Plastic tube	0.15/ft	154	23	[14]	15	26
Circuit boards	4.02/sqft	7000	28	[15]	15	32
Hardware			12		15	14
Container			24		30	28
Tooling			12		15	14
Misc.			12		15	14
Labor			90	[16]	30	117
EDIA	60K/year	0.5 year	30		30	39
Subtotal						324K

Table 9.10: Costs of EM Calorimeter (mechanical) for P–803

EM Calorimeter (Electrical)						
Element	Unit Cost	Quantity	Raw Cost	Comment	Contingency	Total
Amp/ADC readout	40/chan	12440	498	[17]	15	573
EDIA	60K/year	0.5 year	30		30	39
Subtotal						612K

Table 9.11: Costs of EM Calorimeter (electrical) for P–803

Hadron Calorimeter(Mechanical)						
Element	Unit Cost	Quantity	Raw Cost	Comment	Contingency	Total
Zinc	1.52/lb	300K	456	[18]	15	524
Plast. sleeves			18		15	21
Plast. profiles			15		15	17
Circuit bds.			54	[19]	15	63
Hardware			15		15	17
Tooling			15		15	17
Labor			100	[20]	30	130
Misc.			12		15	14
EDIA	60K/year	0.5 year	30		30	39
Subtotal						842K

Table 9.12: Costs of Hadron Calorimeter (mechanical) for P–803

Hadron Calorimeter (Elect.)						
Element	Unit Cost	Quantity	Raw Cost	Comment	Contingency	Total
Amp/ADC readout	40/chan	9832 chan	393	[21]	15	452
EDIA	60K/year	0.25 year	15		30	20
Subtotal						472K

Table 9.13: Costs of Hadron Calorimeter (electrical) for P–803

Mechanical Support Structure						
Element	Unit Cost	Quantity	Raw Cost	Comment	Contingency	Total
Materials			20	[22]	30	26
Labor			30		30	39
EDIA	60K/year	0.25 year	15		30	20
Subtotal						85K

Table 9.14: Costs of Mechanical Support Structure for P–803

Veto Hodoscope						
Element	Unit Cost	Quantity	Raw Cost	Comment	Contingency	Total
Scintillator	180/sqft	144	26	[23]	15	30
PMT	300	48	14	[24]	15	16
Light pipe	150	48	7	[25]	30	9
Assemble	100	24	2	[26]	30	3
Base, cables	200	48	10	[27]	30	13
Stand			5	[28]	30	7
EDIA	60K/year	0.083 year	5		30	7
Subtotal						85K

Table 9.15: Costs of Veto Hodoscope for P–803

First Hodoscope						
Element	Unit Cost	Quantity	Raw Cost	Comment	Contingency	Total
Scintillator	180/sqft	44	8	[29]	15	9
PMT	1.1K	40	44	[30]	15	51
Light pipe	200	40	8	[31]	30	10
Assemble	100	20	2	[32]	30	3
Base, cables	200	40	8	[33]	30	10
Stand			5	[34]	30	7
EDIA	60K/year	0.083 year	5		30	7
Subtotal						97K

Table 9.16: Costs of First Hodoscope for P–803

Second Hodoscope						
Element	Unit Cost	Quantity	Raw Cost	Comment	Contingency	Total
Scintillator	180/sqft	149	27	[35]	15	31
PMT	1.1K	74	81	[36]	15	93
Light pipes	200	74	15	[37]	30	20
Assemble	100	37	4	[38]	30	5
Base, cables	200	74	15	[39]	30	20
Stand			5	[40]	30	7
EDIA	60K/year	0.083 year	5		30	7
Subtotal						183K

Table 9.17: Costs of Second Hodoscope for P–803

Trigger Processor						
Element	Unit Cost	Quantity	Raw Cost	Comment	Contingency	Total
1879 TDC	48/chan	2880	138	[41]	15	159
1821 Interface	7K ea.	2	14	[41]	15	16
1892 Memory	7K ea.	2	14	[41]	15	16
Fastbus crate	30K ea.	2	60	[42]	15	69
TSR card	350 ea.	94	33	[43]	15	38
Subtotal						298K

Table 9.18: Costs of Trigger Processor for P–803

Data Acquisition						
Element	Unit Cost	Quantity	Raw Cost	Comment	Contingency	Total
Read ADCs			62	[44]	30	81
Read TDCs			62	[44]	30	81
Read Hodoscopes			66	[44]	30	86
EDIA	60K/year	0.5 year	30		30	39
Subtotal						287K

Table 9.19: Costs of Data Acquisition for P–803

Online Computing						
Element	Unit Cost	Quantity	Raw Cost	Comment	Contingency	Total
VAX 3200†			80	[45]	15	92
Subtotal						92K

†1 GByte Disk & Tape Drive

Table 9.20: Costs of Online Computing for P–803

Element	Unit Cost	Quantity	Raw Cost	Comment	Contingency	Total
Offline Computing						
VAX 3200	30K	5	150K	[46]	15	173
Subtotal						173K

Table 9.21: Costs of Offline Computing for P–803

Grand Total	9553K

Table 9.22: Total Cost for P–803 Detector

References

[1] Experimenters and J. Krider provided module count and cost figures

[2] Current construction cost of wood frame structures at FNAL

[3] Environmental equipment to control and dispose of phenol, other chemicals

[4] Estimated replacement value of equipment in E653 emulsion facility

[5] Cost estimated by Japanese collaborators on P803

[6] Estimate for raw material and ribbon fabrication based on cost of \$0.60/m for E687 in 1988

[7] Cost estimated by Japanese collaborators on P803

[8] R&D to improve light yield and attenuation length of scintillator

[9] R&D to improve quantum efficiency of photocathode

[10] Estimate based on design experience at FNAL

[11] Estimate based on construction experience at FNAL

[12] Experimenters provided an estimated total cost of \$75/wire for a commercial system using Fastbus, and a reasonable estimate of \$50/wire for the custom design.

[13] Cost estimate for 20 tons of lead alloy sheet — Vulcan Lead Co. (1/4/91)

[14] Typical price of comparable plastic extrusion products

[15] 1/16" FR4, 2 oz copper both sides — Auburn Plastic Engineering (1/4/91)

[16] Estimate based on construction experience at FNAL

[17] Experimenters provided an estimated total cost of \$60–70/wire for a commercial system using Fastbus, and a detailed engineering estimate of \$40/wire for the proposed custom design.

[18] Quote on 150 tons of 36"×36"×1" zinc plate - Belmont Metals, Inc. (1/10/91)

[19] 1/16" FR4, 2 oz copper both sides - Auburn Plastic Engineering (1/4/91)

[20] Estimate based on construction experience at FNAL

[21] Experimenters provided an estimated total cost of $60–70/wire for a commercial system using Fastbus, and a detailed engineering estimate of $40/wire for the proposed custom design.

[22] All support structures stationary — rough estimate

[23] 0.5 inch thick Bicron BC-416 (12/90) (Best Bicron scintillator is twice this price)

[24] RCA 8575

[25] Materials, machining, polishing, plastic bending

[26] Glue and wrap assemblies

[27] 2 cables $40 + base components $40 + 2 hrs machining $70 + assembly $50

[28] Materials and labor

[29] 0.5 inch thick Bicron BC-416 (12/90)

[30] Phone quote on 100 Hamamatsu R2490 tubes (1/8/91)

[31] Materials, machining, polishing Winston cone

[32] Glue and wrap assemblies

[33] 2 cables $40 + base components $40 + 2 hrs machining $70 + assembly $50

[34] Materials and labor

[35] 0.5 inch thick Bicron BC-416 (12/90)

[36] Phone quote on 100 Hamamatsu R2490 tubes (1/8/91)

[37] Materials, machining, polishing Winston cone

[38] Glue and wrap assemblies

[39] 2 cables $40 + base components $40 + 2 hrs machining $70 + assembly $50

[40] Materials and labor

[41] Approximate LeCroy prices (1990)

[42] Crate, power supplies, cooling, misc. interconnections

[43] Cost estimate supplied by C. Rosenfeld from existing AMY design

[44] Estimate based on preliminary engineering design using VME crates with external readout device modules, master and memory modules and 8 mm tape controller

[45] Cost of existing units

[46] Cost of existing units

10 Costs of Facility Construction

10.1 P–803 "Level Beam" Costs — Y-Version

1.	RESONANT EXTRACTION SYTEM	$237K
2.	PRETARGET ENCLOSURE	$1756K
3.	TARGET/HORN/STEEL HALL	$2972K
4.	SERVICE BUILDING FOR T/H/S HALL	$340K
5.	VACUUM DECAY PIPE	$329K
6.	BEAM DUMP HALL	$645K
7.	B. D. H. SERVICE BUILDING	$64K
8.	DETECTOR HALL COMPLEX	$752K
9.	BUBBLE CHAMBER MAGNET	$1173K
10.	D. H. SERVICE BUILDING COUNTING ROOMS	$300K
11.	DETECTOR HALL	$434K
12.	UTILITIES	$250K
13.	ROADS, DRIVEWAYS, PARKING LOTS	$104K
14.	EARTHWORK	$ 614K
15.	CONFINED EARTH SHIELDING	$2230K
16.	RETAINING WALL SYSTEM	$3421K
		$15631K
	15% E. D. I. A.	$2345K
		$17976K
	25% CONTINGENCY	$4112K
	EXCLUSIVE OF STEEL (STEEL HAS 15% CONTINGENCY INCLUDED)	
	PRELIMINARY TOTAL	$22088K

10.2 P–803 & P–805 "Slant Beam" — Y-Version

1.	RESONANT EXTRACTION SYSTEM	$237K
2.	PRETARGET ENCLOSURE	$1756K
3.	TARGET/HORN/STEEL HALL	$2972K
4.	SERVICE BUILDING FOR T/H/S HALL	$340K
5.	VACUUM DECAY PIPE	$329K
6.	BEAM DUMP HALL	$645K
7.	B. D. H. SERVICE BUILDING	$64K
8.	DETECTOR HALL COMPLEX	$895K
9.	BUBBLE CHAMBER MAGNET	$1173K
10.	D. H. SERVICE BUILDING COUNTING ROOMS	$300K
11.	DETECTOR HALL SLURRY WALL SYSTEM	$998K
12.	UTILITIES	$250K
13.	ROADS, DRIVEWAYS, PARKING LOTS	$104K
14.	EARTHWORK	$1078K
15.	CONFINED EARTH SHIELDING	$2230K
16.	RETAINING WALL SYSTEM	$3431K
		$16802K
	15% E. D. I. A.	$2520K
		$19322K
	25% CONTINGENCY EXCLUSIVE OF STEEL (STEEL HAS 15% CONTINGENCY INCLUDED)	$4499K
	PRELIMINARY TOTAL	$23771K

10.3 P–803 & P–805 "Slant Beam" — V-Version

1.	RESONANT EXTRACTION SYSTEM	$237K
2.	PRETARGET ENCLOSURE	$1756K
3.	TARGET/HORN/STEEL HALL	$2972K
4.	SERVICE BUILDING FOR T/H/S HALL	$340K
5.	VACUUM DECAY PIPE	$329K
6.	BEAM DUMP HALL	$645K
7.	B. D. H. SERVICE BUILDING	$64K
8.	DETECTOR HALL COMPLEX	$895K
9.	BUBBLE CHAMBER MAGNET	$1173K
10.	D. H. SERVICE BUILDING COUNTING ROOMS	$300K
11.	DETECTOR HALL SLURRY WALL SYSTEM	$998K
12.	UTILITIES	$250K
13.	ROADS, DRIVEWAYS, PARKING LOTS	$104K
14.	EARTHWORK	$3969K
15.	CONFINED EARTH SHIELDING	$4474K
		$18506K
	15% E. D. I. A.	$2776K
		$21282K
	25% CONTINGENCY EXCLUSIVE OF STEEL (STEEL HAS 15% CONTINGENCY INCLUDED)	$4939K
	PRELIMINARY TOTAL	$26221K

10.4 P–803 & P–805 "Slant Beam" — Slurry Wall Version

1.	RESONANT EXTRACTION SYSTEM	$237K
2.	PRETARGET ENCLOSURE	$1756K
3.	TARGET/HORN/STEEL HALL	$2972K
4.	SERVICE BUILDING FOR T/H/S HALL	$340K
5.	VACUUM DECAY PIPE	$329K
6.	BEAM DUMP HALL	$645K
7.	B. D. H. SERVICE BUILDING	$64K
8.	DETECTOR HALL COMPLEX	$895K
9.	BUBBLE CHAMBER MAGNET	$1173K
10.	D. H. SERVICE BUILDING COUNTING ROOMS	$300K
11.	SLURRY WALL/DETECTOR HALL BEAM LINE SYSTEM	$7085K
12.	UTILITIES	$250K
13.	ROADS, DRIVEWAYS, PARKING LOTS	$104K
14.	EARTHWORK	$1173K
15.	CONFINED EARTH SHIELDING	$2230K
		$19553K
	15% E. D. I. A.	$2933K
		$22486K
	25% CONTINGENCY EXCLUSIVE OF STEEL (STEEL HAS 15% CONTINGENCY INCLUDED)	$5240K
	PRELIMINARY TOTAL	$27726K

10.5 Combined P–803/P–805 Long/Short Baseline Costs — Y–Trench Method

DETAILED LIST OF COSTS

1.	RESONANT EXTRACTION SYSTEM		237K
2.	PRETARGET ENCLOSURE		
	A. ENCLOSURE 20'W X 8'H X 160'L	960K	
	B. EMERGENCY EXIT LABYRINTH		
	3'W X 7'H X 60'L	90K	
	C. DROP HATCH	100K	
	D. RAIL SYSTEM	18K	
	E. LCW SYSTEM	50K	
	F. VACUUM SYSTEM	62K	
	G. ELECTRICAL		
	1. POWER SUPPLIES		
	a. 500KW - 1; ($52K)		
	b. 240KW - 1; ($46K)		
	c. 55KW - 1; ($21K)		
	2. SUBSTATION, 4, 500KVA	276K	
	3. 13.8KV FEEDER, MISC.	80K	
	H. MAGNETS		
	1. 20' DIPOLES (2), ($152K)		
	2. 2.5' TRIM DIPOLES (1), ($ 17K)		
	3. 10' QUADRUPOLES (2), ($100K)		
	4. KICKER SYSTEM	120K	
			1756K

3. TARGET/HORN/STEEL HALL (T/H/S-HALL)		
A. TARGET HALL	917K	
SECTIONS - 15'W X 15'H X 262'L		
B. TARGET	5K	
C. DOUBLE FOCUSING HORN SYSTEM		
INCLUDING POWER SUPPLIES		
AND SPARES (2 TRANS. 4 HORNS)	880K	
D. STEEL SHIELDING	1120K	
9.19' SQ. X 98.43' LONG (3.281' SQ. HOLE)		
9.19' SQ. X 23' LONG (1.64' SQ. HOLE)		
E. ACCESS HATCH SHAFT	50K	
		2972K
4. SERVICE BUILDING FOR T/H/S-HALL		
A. SERVICE BUILDING	250K	
25'W X 12'H X 75'L		
B. PERSONNEL LABYRINTH	90K	
3'W X 7'H X 60'L		
		340K
5. VACUUM DECAY PIPE		
A.1M DIA X 80M LONG	66K	
(3'DIA X 262' LONG)		
B. 1.5M DIA X 160M LONG	263K	
(5' DIA X 524' LONG)		
		329K
6. BEAM DUMP HALL (B.D.H.)		
A. HALL ENCLOSURE	140K	
17' W X 17' H X 28'L		
B. WATER COOLED STEEL BEAM DUMP	505K	
12' W X 12' H X 23'L		
		645K
7. B. D. H. SERVICE BUILDING		
(WITH UTILITY CORRIDOR TO DUMP)		
15'W X 15'L X 12'H AND	34K	
WATER COOLING SYSTEM FOR BEAM DUMP	30K	
		64K

8. DETECTOR HALL COMPLEX		
A. DETECTOR PIT ACCESS AND SURFACE STAGING BUILDING/ WITH CRANE 40'W X 30'H X 85'L	645K	
B. PERSONNEL ACCESS		
1. ELEVATOR	90K	
2. STAIRS, 94 RISERS	25K	
3. UTILITY SHAFT	30K	
4. DIVIDER WALLS	105K	
		895K
9. BUBBLE CHAMBER MAGNET		
A. DISASSEMBLE, MOVE, SET IN PLACE AND HOOK UP MAGNET	250K	
B. LN_2 DEWAR, 12,000 GAL.	110K	
C. COMPRESSOR, 60 GRAMS/SEC	205K	
D. PIPING	60K	
E. CONTROLS AND INSTRUMENTATION	126K	
F. ELECTRICAL	132K	
G. INSTALL REFRIGERATOR, DEWAR AND COMPRESSOR	250K	
H. GAS STORAGE	40K	
		1173K
10. SERVICE BUILDING AND COUNTING ROOMS 30'W X 30'H X 50'L (2 STORY BUILDING)	300K	
		300K
11. DETECTOR HALL/SLURRY WALL SYSTEM	968K	
AND DEWATERING DURING CONSTRUCTION	30K	
		998K
12. UTILITIES		
ELECTRICITY, WATER, GAS, ...ETC.	250K	
		250K
13. ROADS, DRIVEWAYS, PARKING LOTS	104K	
		104K

14. EARTHWORK		
EXCAVATION, FILL, LANDSCAPE	1078K	
		1078K
15. CONFINED EARTH SHIELDING	2230K	
		2230K
16. RETAINING WALL	3431K	
		3431K

TOTALS

SUBTOTAL	$16,802K
15% EDIA	$ 2,520K
TOTAL	$19,322K
25% CONTINGENCY EXCLUSIVE OF STEEL SHIELDING (STEEL HAS A 15% CONTINGENCY INCLUDED)	
$19,448K - $1,120K - $407K = $17,921K	$ 4,372K
PRELIMINARY GRAND TOTAL	$23,771K

11 Funding Profile

We present a funding profile for the Main Injector Neutrino Program including all costs for detectors and construction. The schedule assumes a Main Injector turn-on in January 1996 with a collider run to follow.

P–803 begins in FY 1992 and will have completed both beam and detector construction by the turn-on of the Main Injector. We have listed the cost of emulsion to P–803's Japanese collaborators but not included it in the totals since it will not come from U.S. funding agencies. We assume P–815 Phase I will be approved in June 1991. R&D for the calorimeter will begin in FY 1992. Initial R&D for the spectrometer will start at the same time. Detailed engineering for the spectrometer will begin in FY 1994 with construction to start in FY 1996. We stress that the P–815 Phase II costs are still only pre-proposal estimates.

Table 11.1: Sample Funding Profile for Main Injector Neutrino Program

	FY92	FY93	FY94	FY95	FY96	FY97	Total(U.S.)
P–803 Short-Baseline							
Non-Emulsion	0.47	1.8	2.7	1.7	0.18		6.8
Emulsion (Japan)			(1.4)	(1.4)			
Slant Beam Construction (incl. P–803 Hall, 15' Magnet)							
Construction	4.2	7.1	5.3	4.9	1.9		23.4
P–815 Tevatron							
P–815 Phase I	2.0	1.0	Phase I Run				3.0
P–815 Calorimeter				2.0	5.9		7.9
P–815 Spectrometer	0.03	0.03	0.44	0.50	2.0	2.0	5.0
Total (U.S.)	6.6	9.9	8.4	9.1	9.9	2.0	46.1

Costs in 1990 M$

The Slant Beam Construction costs are based on the following scenario:

- **FY92**
  1. Most of Engineering and Design
  2. Start Pretarget Hall
- **FY93**
  1. Remainder of Pretarget Hall
  2. Target Hall Enclosure
  3. Begin Vacuum Pipe, Confined Earth System, Earth Moving
- **FY94**
  1. Remainder of Vacuum Pipe, Confined Earth System, Earth Moving
  2. Beam Dump Hall
  3. Detector Hall
- **FY95**
  1. Horn Construction
  2. Remaining Service Buildings
  3. Install Components
  4. 15 ft. Magnet Installation
- **FY96**
  1. Remaining Work
  2. Roads and Landscaping
  3. Utilities

Part V

Conclusions

12 Future Work

We identify below several areas of future work which are needed.

12.1 MI/Abort Coupling

The preliminary design presented in this Report will need to evolve as the designs of the Main Injector and of the Neutrino Facility become final. The precise arrangement of beamline elements, monitoring, *etc.* given here are presented as an "existence proof" and as a guide to future work. Specifically, more work is required on

1. The power and power supply requirements.
2. The space and physical plant requirements to accomodate extraction at MI–50.

We will continue to work on these and other issues along with Main Injector personnel through the existing task force.

12.2 Normalization and Test Beams

The P–815 test beams were not discussed because the experimenters have not yet decided on the beams required, although the requirements should not be significantly different from those for previous runs in NE/NT. The members of P–815 are working with the Main Injector Neutrino Group to define these issues.

P–803 expects to calibrate their apparatus in a separate test beam, not in the P–803 area (following the philosophy of CDF and D0). A specific proposal for running time is forthcoming from the experimenters.

12.3 Target and Horns

The "conceptual design" presented here leaves many issues unresolved. We will continue the design of the target and cooling system, relying heavily on the successful design of the existing CERN target. Repairs of the target/horn system (especially those requiring the disconnection of the stripline) require more thought as well.

12.4 Decommissioning

Radioactive elements such as the horn and target would be placed in coffins and stored in the same way as were similar items in the past. The shielding system (dirt and concrete) will present no special dangers and can be handled as would beamlines in other parts of the Laboratory. The steel shielding the target poses significant radiation hazards and we will develop a specific plan in conjuction with the Radiation Safety Department which systematically plans for the decommissioning of the facility.

12.5 P–815 Civil Construction

Interim bracing will be required in the NO1 hall while the pit is being modified. We expect to take out the floor in small sections, bracing both across the floor pit and the walls in the area where the floor is removed. After the steel has been inserted, we will replace the concrete floor and when the section is again secure, move on to the next section. A more systematic engineering assessment is required here and we expect to develop it in the near future.

12.6 Fast Resonant Extractions

At present, each fast extraction involves a loss of ≈ 2 sec to the slow spill Tevatron program (none to the 120 GeV program). Discussions are ongoing with the Accelerator Division about ways to minimize the disruption to slow-spill users. We have determined the time between fast extractions could be cut to 1 sec. in a straightforward way and are studying methods for making it shorter still. An approximate lower limit from the Accelerator seems to be 350–500 msec. The experimenters are investigating running the experiment with slow-spill; this seems possible for the QCD program but difficult for the electroweak experiments. More work is required in order to understand the tradeoffs.

12.7 P–803 Civil Construction

The stability of the slant enclosure and pre-target region are a potential problem. As discussed in the text, we can accomodate up to 1 foot of settling. The amount of settling and possible responses in the design require more study.

12.8 Costs

Several sets of costs have not been addressed:

1. Costs for Magnets and Elements used in the Extraction from the Main Injector.
2. Costs for Handling Radioactive Elements of Target/Horn System.
3. Costs for Control Systems (ACNET/EPICURE).
4. Costs for Cable Plant. Some cabling costs have been estimated (for the experiments proper) but no costs have been assigned for Ethernet, control cables, *etc.*
5. Power Costs. We believe the requirements presented here are approximately correct. We presented the cost of the substations in Chapter 10 but have not yet estimated the costs for supplying power to the experiments.

The Slant-Beam design presented here is still under development and we are looking for ways to improve it, as well as for alternatives. The design, and all civil construction costs in this Report, must be reviewed by the Construction Engineering Department.

This leads to specific R&D requests for P–803 given in Table 12.1.

P–815's R&D requests are covered within the P–815 Proposal. We specifically mention in Table 12.2 two items which should be begun in the next several months: (1) the upgrades to the calorimetry, and (2) the start of engineering studies on the spectrometer. We assign the EDIA discussed earlier to the scintillator. For the spectrometer studies we assign 1 1/2 years of engineer-time (37.5 hrs/wk for 50 weeks) at the standard Fermilab charge-back rate of $30.10/hr (as used in the MI CDR Rev. 2.3).

12.9 Scheduling

There are several running modes for the Main Injector. These include:

Antiproton Production

1. Antiproton production in parallel with a fast extraction to the 120 GeV target. Here, 2.5×10^{13} of the full 3×10^{13} are available.
2. Antiproton production in parallel with a slow spill.

No Antiproton Production

1. This mode has a 1.9 sec cycle time for fast spill and the full intensity is available. This is the mode of running used as the default for our rate estimates.
2. Other modes such as collider injection and fixed target TeV injection occupy no more than 10% of MI cycles.

There is a potential conflict with the KAMI (Kaons at the Main Injector) effort since both experiments are capable of using the full machine intensity. Joint planning is necessary here; continuous running of either experiment is not envisaged under any circumstances, which allows for flexibility.

There is no conflict with the Tevatron experiment P–815. Fast resonant extraction in the Tevatron is unaffected by fast resonant extraction from the MI.

P803 R & D FOR FALL '91 AND CALENDAR 1992

1)	Fibers (Investigate readout techniques,fibers)	\$60K
2)	Explore alternative to fibers	\$15K
3)	Explore new data acquisition architecture (Develop new chip jointly with LeCroy)	\$50K
4)	Build prototypes for calorimeter tube chambers	\$40K
5)	Build prototypes for tracking chambers	\$45K
	TOTAL	\$210K

Table 12.1: R&D Requests for P–803.

P–815 R & D FOR FALL '91 AND CALENDAR 1992

1)	Upgrade to Scintillator Calorimetry	\$60K
2)	Engineering Studies of Upgraded Spectrometer	\$90K
	TOTAL	\$150K

Table 12.2: R&D Requests for P–815.

13 Summary and Conclusions

We have seen that the Main Injector neutrino program is both a comprehensive and deep program, simultaneously offering the potential for major discovery and important improvements of existing measurements.

The primary goal of the low-energy program is the search for neutrino oscillations. The discovery of neutrino oscillations would be the first demonstration of the violation of lepton number and hence would be our first glimpse of physics at the Grand Unification scale. The long-baseline experiments, especially working in tandem with the short-baseline effort, can explore territory accessible in no other way and are elegant and beautiful experiments in their own right. The combination could potentially (1) find the source of 90% of the mass of the Universe, (2) establish the violation of lepton number, and (3) discover the ν_τ. The discovery potential of such a program is enormous. In addition, the experiments can perform valuable measurements of V_{cd} and slow-rescaling.

The Tevatron experiments offer solid, precise measurements of structure functions which both incisively test QCD and provide much-needed data for the SSC. The measurements of $\sin^2\theta_W$ and ρ are essential for probing physics at the TeV mass scale and will both complement and extend the measurements which can be made at colliders. In the case of the ρ parameter neutrino-nucleon scattering provides unique information on a wide variety of new physics. Limits on rare processes also provide constraints on new physics and with an order-of-magnitude more data, offer the possibility of a solid discovery of new phenomena.

We have designed a 120 GeV transport system, target, and horn which will provide the required beam to the experiments while also meeting the safety and groundwater criteria. The arrangement has the additional feature of combining the abort and extraction functions of the Main Injector, simplifying construction and reducing the overall expense. A major finding of this Report is that short-baseline and long-baseline oscillation experiments may be combined along a common beamline, with all the physics advantages of such an arrangement, for only a small marginal cost over that of a single experiment.

One of the beams necessary for the Tevatron program has already been successfully

operated; the other requires no new technology and in many ways involves only small changes from the existing beamline. The Civil Construction necessary for this experiment is not significant in either complexity or expense.

We have described the experimental methods, presented the design, and estimated the costs of both medium and high-energy neutrino programs at the Main Injector. The experiments will create a new generation of neutrino physics in the coming decade, testing the Standard Model and searching for new physics across an enormous arena of energy and distance scales. We will provide accurate and decisive measurements on topics ranging from precise tests of QCD to the nature of the Higgs sector to the most profound questions of cosmology. This range and depth, providing at the same time both increased precision and increased reach, are unique to the Main Injector and testify to its vast potential.